

การจำลองการยึดเหนี่ยวเชิงกลระหว่างคอนกรีตและเหล็กเสริมภายใต้อุณหภูมิที่เพิ่มขึ้น



นาย ปฐมเมศ ผาณิตพจมาน

ศูนย์วิทยพัทยากร
จุฬาลงกรณ์มหาวิทยาลัย

วิทยานิพนธ์นี้เป็นส่วนหนึ่งของการศึกษาตามหลักสูตรปริญญาวิศวกรรมศาสตรดุษฎีบัณฑิต

สาขาวิศวกรรมโยธา ภาควิชาวิศวกรรมโยธา

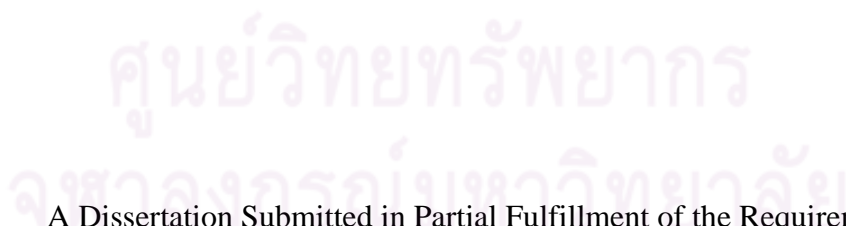
คณะวิศวกรรมศาสตร์ จุฬาลงกรณ์มหาวิทยาลัย

ปีการศึกษา 2553

ลิขสิทธิ์ของจุฬาลงกรณ์มหาวิทยาลัย

MODELING OF MECHANICAL BONDING BETWEEN CONCRETE AND
REINFORCING STEEL BARS UNDER ELEVATED TEMPERATURES

Mr. Pattamad Panedpojaman



A Dissertation Submitted in Partial Fulfillment of the Requirements
for the Degree of Doctor of Philosophy Program in Civil Engineering

Department of Civil Engineering

Faculty of Engineering

Chulalongkorn University

Academic Year 2010


Copyright of Chulalongkorn University



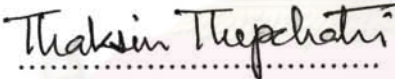
5 0 7 1 8 8 3 9 2 1


Thesis Title MODELING OF MECHANICAL BONDING
BETWEEN CONCRETE AND REINFORCING STEEL
BARS UNDER ELEVATED TEMPERATURES
By Mr. Pattamad Panedpojaman
Field of study Civil Engineering
Thesis Advisor Associate Professor Thanyawat Pothisiri, Ph.D.

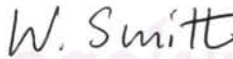
Accepted by the Faculty of Engineering, Chulalongkorn University in Partial
Fulfillment of Requirements for the Doctoral Degree

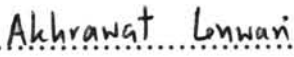
.....  Dean of the Faculty of Engineering
(Associate Professor Boonsom Lerdhirunwong, Dr. Ing.)


THESIS COMMITTEE

 Chairman
(Professor Thaksin Thepchatri, Ph.D.)

 Thesis Advisor
(Associate Thanyawat Pothisiri, Ph.D.)

 Examiner
(Assistant Professor Watanachai Smittakorn, Ph.D.)

.....  Examiner
(Akhrawat Lenwari, Ph.D.)

.....  External Examiner
(Assistant Professor Naret Limsamphancharoen, Ph.D.)

ปฐมเมศ ผาณิตพจนาน : การจำลองการยึดเหนี่ยวเชิงกลระหว่างคอนกรีตและเหล็กเสริมภายใต้
 อุณหภูมิที่เพิ่มขึ้น. (MODELING OF MECHANICAL BONDING BETWEEN CONCRETE
 AND REINFORCING STEEL BARS UNDER ELEVATED TEMPERATURES) อ.ที่ปรึกษา
 วิทยานิพนธ์หลัก : รศ. ดร.ธัญวัฒน์ โทษศิริ, 106 หน้า

การศึกษานี้นำเสนอแบบจำลองการยึดเหนี่ยวเชิงกลซึ่งสามารถอธิบายพฤติกรรมการยึด
 เหนี่ยวของ โครงสร้างคอนกรีตเสริมเหล็กภายใต้อุณหภูมิที่เพิ่มขึ้น แบบจำลองดังกล่าวพัฒนาบนพื้นฐาน
 ของทฤษฎีการแตกร้าวแบบรวมผล และทฤษฎีรูปทรงกระบอกผนังหนา โดยพิจารณาการเปลี่ยนแปลงของ
 สภาพะยึดหยุ่นแบบเกิดการแตกร้าวบางส่วน ความสัมพันธ์ระหว่างความต้านทานการแยกออกและรัศมี
 การแตกร้าวภายในคอนกรีตหุ้มที่อุณหภูมิสูงพิจารณาการเปลี่ยนแปลงคุณสมบัติของวัสดุตามค่าอุณหภูมิ
 และการขยายตัวเชิงอุณหภูมิที่ต่างกันของคอนกรีตและเหล็กเสริม การตรวจสอบความถูกต้องของ
 แบบจำลองที่นำเสนออาศัยผลการทดสอบค่ากำลังยึดเหนี่ยวของตัวอย่างคอนกรีตเสริมเหล็กที่เกิดการวิบัติ
 แบบแยกออกภายใต้อุณหภูมิปกติและอุณหภูมิสูงในงานวิจัยที่ผ่านมา การศึกษานี้ยังได้นำเสนอ
 ความสัมพันธ์ระหว่างหน่วยแรงยึดเหนี่ยวและการกระจัดสัมพัทธ์ระหว่างคอนกรีตและเหล็กเสริมกับ
 แบบจำลองที่นำเสนอ โดยอ้างอิงผลการทดสอบในงานวิจัยที่ผ่านมา

การศึกษานี้ได้ทำการทดสอบความสามารถในการรับน้ำหนักบรรทุกของคานคอนกรีตเสริม
 เหล็กซึ่งมีระยะคอนกรีตหุ้ม 25 มม. และ 40 มม. ภายใต้อุณหภูมิสูง โดยเปรียบเทียบผลการทดสอบในรูป
 ของความสัมพันธ์ระหว่างน้ำหนักบรรทุกและการโก่งตัว รวมทั้งรูปแบบการแตกร้าว กับผลการวิเคราะห์
 โดยระเบียบวิธีไฟไนต์เอลิเมนต์ซึ่งพิจารณาแรงยึดเหนี่ยวสองรูปแบบ ได้แก่ การยึดเหนี่ยวแบบสมบูรณ์
 และการยึดเหนี่ยวที่เกิดการกระจัดสัมพัทธ์ (แบบจำลองที่นำเสนอ) จากผลการศึกษาพบว่าผลการวิเคราะห์
 โดยพิจารณาการยึดเหนี่ยวที่เกิดการกระจัดสัมพัทธ์สามารถทำนายการแตกร้าวของคอนกรีตแบบแยกออก
 ในคานทดสอบได้ ซึ่งสอดคล้องกับผลการทดสอบ ในขณะที่การวิเคราะห์โดยพิจารณาการยึดเหนี่ยวแบบ
 สมบูรณ์มีแนวโน้มที่จะทำนายค่าหน่วยแรงยึดเหนี่ยวสูงเกินไป

ผลการศึกษานี้แสดงให้เห็นว่าแบบจำลองที่นำเสนอสามารถใช้ในการประเมินการ
 เสื่อมสภาพของการยึดเหนี่ยว พฤติกรรมการแตกร้าวแบบแยกออกของคอนกรีตหุ้ม รวมทั้งผลกระทบต่อ
 พฤติกรรมของคานคอนกรีตเสริมเหล็กภายใต้อุณหภูมิที่เพิ่มขึ้นได้

ภาควิชาวิศวกรรมโยธา..... ลายมือชื่อนิสิต ปฐมเมศ
 สาขาวิชาวิศวกรรมโยธา..... ลายมือชื่อ อ.ที่ปรึกษาวิทยานิพนธ์หลัก ธัญวัฒน์
 ปีการศึกษา 2553.....

5071883921

MAJOR CIVIL ENGINEERING

KEYWORDS :

BONDING / SPLITTING CRACK / RC STRUCTURES / FIRE

PATTAMAD PANEDPOJAMAN : MODELING OF MECHANICAL BONDING BETWEEN CONCRETE AND REINFORCING STEEL BARS UNDER ELEVATED TEMPERATURES THESIS ADVISOR : ASSOC. PROF. THANYAWAT POTHISIRI, Ph.D., 106 pp.

A mechanical bond model capable of characterizing the bonding behavior of reinforced concrete structures under elevated temperatures is proposed in the current study. The proposed model is developed based on the smear crack theory and the thick-wall cylinder theory by considering the concrete cover in its partially cracked elastic stage. The relationship between the splitting resistance and the inner crack radius of the concrete cover at the elevated temperature is established by taking into account the variation of the material properties with temperature and the differential thermal expansion of the steel rebar and the concrete cover. The proposed model is verified by using previous experimental results on the splitting bond strength of reinforced concrete pull-out specimens at normal and elevated temperatures. Furthermore, to investigate the bonding effect on the behavior of reinforced concrete structures, the relationship between the bond-slip curve and the proposed model is also established based on previous experimental results.

A series of load-bearing tests is conducted for reinforced concrete beams with 25-mm and 40-mm concrete covers subjected to elevated temperatures. The test data of the reinforced concrete beams in terms of the load-deflection relationship and the crack pattern are compared with the results obtained from the finite-element analyses assuming two types of bonding: perfect bonding and slip bonding (the proposed model). It is found that the FE models with slip bond are capable of predicting the tensile splitting cracks in the beam specimens which is consistent with the experimental results whereas the FE models with perfect bond tend to overestimate the bond stresses.

Based on the results of the current study, the proposed model can be used to assess the bonding degradation and the tensile splitting cracks as well as their influences upon the behavior of reinforced concrete beams at elevated temperatures.

Department : Civil Engineering Student's signature Pattamad
 Field of study : Civil Engineering Advisor's signature Thanyawat Pothisiri
 Academic year : 2010

ACKNOWLEDGEMENTS

The author wishes to express his deep appreciation and sincere gratitude to his thesis advisor, Associate Professor Thanyawat Pothisiri, Ph.D., for the guidance, assistance and constant support throughout his study at Chulalongkorn University. Grateful acknowledgements are due to Professor Thaksin Thepchatri, Ph.D., Assistant Professor Watanachai Smittakorn, Ph.D., Assistant Professor Naret Limsamphancharoen, Ph.D. and Akhrawat Lenwari, Ph.D. for their invaluable comments and recommendations. Special thanks are also extended to those who have helped directly and indirectly in the preparation of this thesis.



ศูนย์วิทยทรัพยากร
จุฬาลงกรณ์มหาวิทยาลัย

CONTENTS

	Page
Abstract (Thai)	iv
Abstract (English)	v
Acknowledgements	vi
Contents	vii
List of Tables	ix
List of Figures	x
CHAPTER I: INTRODUCTION	1
1.1 Introduction.....	1
1.2 Literature Review.....	2
1.3 Research Objectives.....	5
1.4 Scope of Research Works.....	5
1.5 Research Methodology	6
CHAPTER II: THEORETICAL BACKGROUND	8
2.1 Introduction.....	8
2.2 Bonding Mechanism	9
2.3 Analytical Model.....	12
2.3.1 Relationship between Radial Pressure and Bond Stress.....	12
2.3.2 Splitting Resistance of Concrete Cover at elevated Temperatures.....	13
2.3.3 Radial Pressure and Inner Crack Radius at elevated Temperatures.....	19
2.3.4 Bond Stress at Elevated Temperatures	22
2.4 Variation of Bond Strength with respect to Bond Length.....	24
2.5 Variation of Steel and Concrete Properties with Temperature	27
2.5.1 Concrete under and after High Temperatures	27
2.5.2 Variation of Thermal and Mechanical Properties of Steel and Concrete with Temperature.....	29

	Page
2.5.3 Tensile Stress–Strain Relationship of Concrete at Elevated Temperatures.....	31
CHAPTER III: VERIFICATION OF THE ANALYTICAL MODEL.....	35
3.1 Introduction.....	35
3.2 Tensile Softening Crack Model for Concrete at Normal Temperature....	36
3.3 Radial Pressure due to Differential Thermal Expansion of Materials.....	37
3.4 Prediction of Bond Strength for Reinforced Concrete at Elevated Temperatures.....	43
3.5 Bond-slip Relationship.....	47
CHAPTER IV: APPLICATION OF THE MODEL FOR REINFORCED CONCRETE BEAMS AT ELEVATED TEMPERATURES.....	54
4.1 Introduction.....	54
4.2 Experimental Setup	55
4.2.1 Test Specimens.....	55
4.2.2 Test Program.....	56
4.2.3 Experimental Results.....	60
4.3 FE Analysis.....	66
4.3.1 Structural Modeling.....	66
4.3.2 Thermal and Mechanical Properties.....	69
4.4 Finite Element Analysis Results and Discussions.....	72
CHAPTER V: CONCLUSIONS	90
REFERENCES.....	93
APPENDIX	100
VITA.....	106

LIST OF TABLES

		Page
Table 2.1	Variation of thermal properties of concrete and steel with temperature.....	29
Table 2.2	Variation of mechanical properties of steel with temperature.....	30
Table 2.3	Variation of mechanical properties of concrete with temperature ...	30
Table 2.4	Variation of compressive strength, peak strain and ultimate strain of concrete with temperature.....	31
Table 2.5	Variation of the normalized fracture energy $G_{f,T} / G_{f,20^{\circ}C}$ with temperature (Zhang and Bicanic 2002).....	35
Table 3.1	Comparison of the predicted bond strengths with previous experimental results for normal temperature	36
Table 3.2	Comparison of the ΔT_{cr} values computed by the proposed method with the results obtained from the previous studies.....	40
Table 3.3	Details of the pull-out specimens in previous experiments.....	44
Table 4.1	Temperatures and heating periods for fire tests.....	59
Table 4.2	Types of failure for the beam specimens	65
Table 4.3	Average temperatures for the bond-slip curves.....	71

LIST OF FIGURES

		Page
Figure 2.1	Mechanism of bond resistance in confined concrete (Eligeliausen 1983)	11
Figure 2.2	Bond-slip relationships for different types of failure (Steffen 2004)	12
Figure 2.3	Pull-out force transfer between rebar and concrete (Tepfers 1980 and Sakai <i>et al.</i> 1999).....	13
Figure 2.4	Modeling of a pull-out specimen as a hollow concrete cylinder subjected to a uniform pressure on the inner surface	14
Figure 2.5	Distribution of tensile ring stresses	15
Figure 2.6	Stress–strain relationship for concrete in tension.....	16
Figure 2.7	The pressure resistance model for a partially cracked concrete cylinder (Wang and Liu 2003)	17
Figure 2.8	Differential thermal expansion of concrete and rebar.....	20
Figure 2.9	Computational procedure for the thermal radial pressure and the inner crack radius due to thermal expansion.....	21
Figure 2.10	Reinforcement bar-concrete interface.....	23
Figure 2.11	Modeling of the pressure resistance of the concrete cover under the pull-out load and the thermal effect.....	24
Figure 2.12	The bond stress, tensile load, and slippage distribution (Akira and Toshiyuki, 2003)	25
Figure 2.13	Typical load-deformation response of concrete in uniaxial tension...	32
Figure 2.14	Tensile stress-crack width relationship at normal temperature.....	32
Figure 2.15	Tensile stress–strain relationship for concrete at temperature T	34
Figure 2.16	The normalized tensile stress–strain relationship for concrete at the elevated temperatures.....	34
Figure 3.1	Comparison of the predicted bond strengths with previous experimental results for reinforced concrete at normal temperature....	37
Figure 3.2	Splitting failure of the concrete cover (Aiello 2001; Wong 2006)	38

	Page
Figure 3.3	Variation of ΔT_{cr} with respect to different c/d_b values for FRP reinforced concrete..... 41
Figure 3.4	Comparison between the cracking patterns of the cylindrical FRP reinforced concrete specimens with $c/d_b = 4.38$ as predicted by the MTED model and the crack radius r_i values obtained by the proposed model..... 42
Figure 3.5	Comparison of the predicted bond strengths with the test results of Diederichs and Scheider (1981) 45
Figure 3.6	Comparison of the predicted bond strengths with the test results of Hertz (1982) 45
Figure 3.7	Comparison of the predicted bond strengths with the test results of Morley and Royles (1983) after elevated temperatures 46
Figure 3.8	Comparison of the predicted bond strengths with the test results of Morley and Royles (1983) at elevated temperatures..... 47
Figure 3.9	Comparison of the predicted bond strengths with the test results of Haddad <i>et al.</i> (2008) 47
Figure 3.10	Analysis of bond-slip-inner crack radius relationship..... 49
Figure 3.11	Comparison between the experimental slip and the analytical slip ($k = 70$)..... 51
Figure 3.12	Comparison between the bond-slip relationships obtained by the proposed method and the test results 52
Figure 3.13	Comparison between the bond-slip relationship obtained by the proposed method and the test results of Diederichs and Scheider (1981) 52
Figure 3.14	Comparison between the bond-slip relationship obtained by the proposed method and the test results of Morley and Royles (1983) 53
Figure 3.15	Comparison between the bond-slip relationship obtained by the proposed method and the test results of Haddad <i>et al.</i> (2008) 53
Figure 4.1	Details of a typical beam specimen..... 56

	Page
Figure 4.2	Experimental setup for the flexural test of reinforced concrete beams at elevated temperatures 57
Figure 4.3	Top view of the furnace..... 59
Figure 4.4	The specified temperature-time relationships for fire tests..... 59
Figure 4.5	Temperature-time curves for the specimens in C25 series..... 61
Figure 4.6	Temperature-time curves for the specimens in C40 series..... 62
Figure 4.7	Load-deflection curves of the beam specimens 63
Figure 4.8	Crack patterns of the beam specimens 64
Figure 4.9	Different types of failure..... 65
Figure 4.10	Modeling of the beam specimen..... 66
Figure 4.11	Overall process of structural analysis..... 67
Figure 4.12	Finite element models 68
Figure 4.13	Variation of the tensile stress-strain relationships for steel with temperature (BS EN 1992-1-2 (2004)) 70
Figure 4.14	Variation of the stress-strain relationships for concrete with temperature..... 70
Figure 4.15	Finite element model for the heat transfer analysis to obtain the bond-slip curve..... 71
Figure 4.16	Bond-slip relationships for the finite element analysis..... 71
Figure 4.17	Comparison of the load-deflection curves obtained from the experiment and the FE analysis 76
Figure 4.18	Graphical representation of cracks 77
Figure 4.19	Variation of the crack patterns with load for C25-RT 78
Figure 4.20	Variation of the crack patterns with load for C25-250..... 79
Figure 4.21	Variation of the crack patterns with load for C25-440 80
Figure 4.22	Variation of the crack patterns with load for C25-550 81
Figure 4.23	Variation of the crack patterns with load for C40-RT 82
Figure 4.24	Variation of the crack patterns with load for C40-250 83
Figure 4.25	Variation of the crack patterns with load for C40-400 84
Figure 4.26	Variation of the crack patterns with load for C40-550 85
Figure 4.27	Variation of the tensile force and the bond stress distribution along the rebar with load for C25-RT..... 86

	Page
Figure 4.28	Variation of the tensile force and the bond stress distribution along the rebar with load for C25-250..... 86
Figure 4.29	Variation of the tensile force and the bond stress distribution along the rebar with load for C25-440..... 87
Figure 4.30	Variation of the tensile force and the bond stress distribution along the rebar with load for C25-550..... 87
Figure 4.31	Variation of the tensile force and the bond stress distribution along the rebar with load for C40-RT..... 88
Figure 4.32	Variation of the tensile force and the bond stress distribution along the rebar with load for C40-250..... 88
Figure 4.33	Variation of the tensile force and the bond stress distribution along the rebar with load for C40-440..... 89
Figure 4.34	Variation of the tensile force and the bond stress distribution along the rebar with load for C40-550..... 89
Figure A-1	FE models with different meshing schemes..... 102
Figure A-2	Load-deflection relationships obtained from the FE models with different meshing schemes..... 102
Figure A-3	Comparison of the temperature-time curves obtained from the experiment and the FE model with 5-mm elements for C25 specimens..... 103
Figure A-4	Comparison of the temperature-time curves obtained from the experiment and the FE model with 5-mm elements for C40 specimens..... 104
Figure A-5	Lines A-A and B-B for the comparison of temperature distribution 105
Figure A-6	Comparison of the temperature distribution obtained from the FE model in case M4 and the FE model with 5-mm elements..... 105

CHAPTER I

INTRODUCTION

1.1 Introduction

Reinforced concrete (RC) structures are vulnerable to high-temperature conditions such as those during a fire. At elevated temperatures, the mechanical properties of concrete and reinforcing steel as well as the bond between steel and concrete may significantly deteriorate. Consequently, the RC structures must be evaluated for reuse or repair after fire incidents. Normally, severe damage of concrete, e.g. spalling, must be removed and repaired whereas the less-severe or non-visible damaged concrete can be examined for its residual capacity by destructive or nondestructive tests.

The post-fire investigation of RC structural elements with less severe or non-visible damage generally focuses on the residual compressive strength of the intact concrete. The other mechanical properties are often neglected, particularly the interaction or bonding between the reinforcement bars and the concrete cover. The changes in the bonding behavior may influence the flexibility or the moment capacity of the RC structures. Besides, the changing bond stress-slip relationships can cause additional joint moment in the RC structures. However, the investigation of the bonding between rebar and concrete at elevated temperatures is quite difficult in real cases.

During the past few decades, many researchers have studied the effect of elevated temperature on the interaction between reinforcement bars and concrete cover. The early investigations focused on the residual bond strength (Reichel 1978). Because the residual bond strength is not sufficient to represent the overall bonding mechanism between rebar and concrete, the bond-slip curve has also been examined (Diederichs and Schneider 1981). Various parameters that affect the bonding behavior, e.g. concrete strength, type of bar surface, heating duration, etc., have also been

investigated by other researchers (Hertz 1982; Royles and Morley 1983). Although a large number of experiments in this field have been conducted, the outcomes have mostly been expressed in forms of statistical models or percentages of bond strength reduction without a thorough understanding of the mechanics behind the changing bond and slip behavior under elevated temperatures. Without a proper mechanical model, the effect of the changing bonding interaction on the RC structures during fire cannot be clearly explained.

The development of the mechanical models for bonding between concrete and reinforcing steel bars thus far has been limited. Most bonding models adopt the material properties under the normal temperature condition. A popular model is based on the thick-wall cylinder theory (Timoshenko 1970) and the smear crack theory (Takahiro *et al.* 1999; Wong and Liu 2003). In this study, a mechanical model of bonding between concrete and steel reinforcement based on the smear crack theory is developed by taking the effect of increasing temperatures into consideration.

1.2 Literature Review

Previous investigations of the influence of high temperatures on the bond between concrete and reinforcing steel bars have focused mainly on the residual bond strength and the bond stress-slip relationship with respect to various parameters. In an early investigation, Reichel (1978) has conducted pull-out tests for bond strength with plain round and deformed rebars after fire. It has been concluded that the bond strength can significantly degrade at the temperature of up to 600°C. Subsequently, many researchers have investigated the residual bond strength with respect to various parameters and proposed mathematical functions to predict the residual bond strength based on statistical methods. Diederichs and Schneider (1981) have examined the bond stress-slip curve under high temperatures ranging from 20°C to 800°C. Their results show the shift of the bond-slip behavior at high temperatures. Hertz (1982) has concluded that the diameter of the rebars has little influence on the loss of bond strength at high temperatures of up to 500°C. Royles and Morley (1983) have investigated the bond strength with different concrete covers under and after high temperatures of up to 750°C. The study revealed that the specimens with thinner

concrete covers experienced greater reduction in bond strength. Moreover, the bond strengths under and after high temperatures were slightly different. Zhou and Wu (1995) have shown that the degradation of bond strength due to the increasing temperature is faster than the decrease of concrete compressive strength. Furthermore, Xie and Qian (1998) have proposed that the splitting bond stress after fire is proportional to the concrete tensile strength. Chiang and Tsai (2003) have investigated the influence of high temperatures in terms of the heating duration. It has been shown that longer heating duration may cause lower residual bond strength. Haddad *et al.* (2008) have examined the residual bond strength and the bond stress-slip relationship with respect to the percentage of fibers added to the aggregates of concrete. The results revealed that the use of fibers could lessen the degree of bond strength reduction.

Many researchers have proposed a single function to calculate the residual bond strength of reinforced concrete due to exposure to different temperatures based on the experimental results (see for example, Xie and Qian (1998), Chiang and Tsai (2003) and Haddad *et al.* (2008)). Most of the proposed functions were based on statistical analysis; no clear explanation on the mechanics of bonding between concrete and reinforcing bars was provided. Moreover, the developed functions for the residual bond strength can accurately predict only the cases similar to the experimental studies. A holistic mechanical model is, therefore, essential to understand the mechanism of bonding as well as to predict the residual bond strength for reinforced concrete after exposure to high temperature conditions.

The mechanical model for the reinforced concrete bond interface after fire has been introduced in the literature in the late 1990s. El-Hawary and Hamoush (1996) have proposed a mechanical formulation to predict the interfacial bond shear modulus for reinforced concrete after being subjected to elevated temperatures. The varying parameters include the diameter of the steel bars, the heating duration, the level of temperature, and the method of cooling. The specimens were controlled the type of failure by the loss of bond. The load-slip test results were analyzed using fracture mechanics assuming linear elastic behavior for both steel and concrete. Only the post-fire mechanical properties of concrete and steel, particularly the residual compressive strength of concrete, were required in their formulation. This model has limitations in

that the linear elastic behavior of concrete and steel is assumed and that the residual bond strength cannot be computed explicitly.

Even with limited studies on the high-temperature effects on the bonding behavior for reinforced concrete, the mechanical models of bonding between steel rebar and concrete have been well established for reinforced concrete at normal temperature. Tepfers (1979) has adopted Timoshenko's thick-wall cylinder theory (Timoshenko 1970) in his model. It has been concluded that bond failure occurred during the partly-cracked elastic stage and the plastic stage of concrete cover (Tepfers 1982). The smear crack theory has thus been adopted for the cracking part. Different concrete tensile softening models can be used to investigate the cracked part, such as the discrete crack model proposed by Den Uijl and Bigaj (1996) and the elastocohesive model proposed by Gambarova and Rosati (1997). However, the number of cracks must be known a priori in these models. As such, it is not applicable for real reinforced concrete structures in which it is difficult to determine the actual number of cracks. To overcome this problem, Takahiro *et al.* (1999) have proposed a bonding model that neglects the cracking part. The most up-to date analytical model has been proposed by Wang and Liu (2003) using the smear crack theory to represent the sum of the true and discrete crack openings.

A few researchers have investigated the correlation between the slip and the mechanical parameters required to establish the bond-slip relationship for reinforced concrete at normal temperature. Den Uijl and Bigaj (1996) have proposed the relationship between tangential strains of the concrete cover at the interface and slip only based on their mechanical model. Takahiro *et al.* (1999) have found the relationship between their analytical crack radius and experimental slip. Takahiro *et al.*'s relationships (1999) can accurately predict only the cases similar to the experimental studies.

To understand the bonding behavior of reinforcing steel and concrete and to predict the residual bond strength of the reinforced concrete structures at elevated temperatures, a holistic mechanical model is essential. To date, only the mechanical bonding model for normal temperature is available. This study, therefore, intends to develop a mechanical bonding model for reinforced concrete exposed to high

temperatures taking into account the varying mechanical properties of steel and concrete.

1.3 Research Objectives

The key objective of this research is to develop a mechanical model to characterize the bonding behavior of reinforcing steel embedded in concrete and to predict the residual bond strength under fire. Two objectives of the current research are addressed as follows:

- 1.3.1 To investigate the influences of elevated temperatures on the bonding behavior and to explore the interaction between the embedded steel reinforcing bars and the concrete cover during fire
- 1.3.2 To develop a mechanical model that is capable of characterizing the bonding behavior of reinforced concrete at elevated temperatures

The outcome of the current research is expected to facilitate engineers in making the decision whether to reuse or repair the fire-damaged concrete.

1.4 Scope of Research Works

For the current study, the mechanical model of bonding between concrete and reinforcing steel is developed based on Timoshenko's thick-wall cylinder theory (Tepfers 1982). The model assumes splitting failure, which is common for pull-out specimens and real structures, as the primary mode of failure for bonding between the embedded steel reinforcing bars and the concrete cover.

Based on the model proposed by Tepfers (1979), the bond failure occurs during the partly-cracked elastic stage and the plastic stage of concrete cover. Because it is seldom that regular concrete reach the plastic stage, the current study focuses only upon the cracked elastic stage of concrete. Furthermore, the damaged concrete cover in the partly-cracked elastic stage can be subdivided into the cracked part and the

elastic part. For the cracked part, the smear crack theory (Wang and Liu 2003) is adopted to estimate the tensile strength after cracking.

The change in the mechanical properties of concrete and reinforcement bars at elevated temperatures can affect the bonding behavior. For instance, the thermal expansion of steel and concrete may cause extra internal stresses. In addition, the dropping tensile strength may lead to crack propagation in the concrete cover. The induced internal stresses, cracking and the interaction between the reinforcing bar and the concrete cover can be examined by using the finite element model, taking into account the varying mechanical and thermal properties of steel and concrete with respect to temperature. The results obtained from the finite element analysis will be compared with the experimental data collected from the literature.

The residual bond strength is generally useful for the less damaged reinforced concrete elements which must be decided whether to be reused or repaired. Therefore, the investigation of the bonding behavior is limited up to the temperature of 500°C. After this level of temperature the concrete may experience severe damage and loss of bond strength (Morely and Royles 1983; Bazant and Kaplan 1996; Kodur and McGrath 2003; Haddad and Shannis 2004).

1.5 Research Methodology

In order to understand the influence of high temperature upon the bonding behavior of reinforced concrete, the framework of this study includes theoretical review, analytical and experimental studies, and case studies. The research method can be explained as follows:

- 1.5.1 Review the basic theories and previous experimental data regarding bond failure, bond stress-slip relation, thick-wall cylinder theory, mechanical bond strength models, smear crack theory and concrete properties.
- 1.5.2 Examine the previous bond strength models for reinforced concrete at normal temperature and compare the modeling results with the experimental data drawn from the literature.

- 1.5.3 Develop a mechanical model for bonding between reinforcing steel and concrete under elevated temperatures.
- 1.5.4 Verify the efficacy of the proposed mechanical model by comparing the mechanical bond strength with previous experimental results in the literature.
- 1.5.5 Investigate the relationship between the mechanical bond stress and slip to generate the bond stress-slip curve for reinforced concrete during fire. The bond stress-slip curve can be used to examine the structural behavior due to the changes in bonding between reinforcing steel and concrete under high temperatures.
- 1.5.6 Conduct experiments on the flexural behavior of reinforced concrete beams under different temperature loads of 200, 350 and 500°C. The experimental results will be used to investigate the influence of the changing bond stress-slip relationship on the overall structure behavior.
- 1.5.7 Compare the experimental results with those obtained from the finite element models using the proposed bond stress-slip relationship.
- 1.5.8 Discussion and conclusion.

CHAPTER II

THEORETICAL BACKGROUND

2.1 Introduction

As previously discussed, a holistic mechanical model is essential for predicting the residual bond strength of reinforced concrete at elevated temperatures. The development of such a model requires that the bonding behavior as well as the interaction between concrete and reinforcement bars be fully comprehended during the increasing temperature. Based on the data from the pull-out tests that have previously been published in the literature (Tepfers 1979; Eligehausen 1979), the bond strength depends mainly on the concrete cover or the bar spacing of the reinforcing bars and the mechanical properties of the concrete cover. Further, it has been shown that most bonding failure is determined by the splitting bond strength (Tepfers 1982).

To develop the splitting bond strength model, this study adopts the model of Wang and Liu (2003) based on the thick-wall cylinder theory (Timoshenko 1970) and Tepfers' model (Tepfers 1979). Because the bond failure occurs in the partially cracked elastic stage of the concrete cover (Tepfers 1982), the model can be subdivided into the cracked part and the elastic part. The mechanical models of Tepfers (1979) and Wang and Liu (2003) consider only the bond strength for short embedded length of reinforcing bars, the so-called local bond strength. To account for the actual bond stress distribution that may vary with the increasing embedded length, Yasojima and Kanakubo (2003) have proposed a standardization technique based on a governing equation of bond stress and slip relationship and an equivalent bond stress block (EBSB). The proposed model of Wang and Liu (2003) can predict the bond strength only for normal-temperature cases but will be used as the prototype for the bond strength model of reinforced concrete under high-temperature conditions.

The variation of mechanical and thermal properties of concrete and reinforcing steel with temperature brings about changes in the load-bearing capacity of the concrete cover as well as the internal stresses of concrete and steel. The bonding behavior of reinforced concrete structures may be affected by these changes and will be investigated in the current study through a series of finite element analyses.

2.2 Bonding Mechanism

The pull-out test simulates the condition in which a pullout force is applied to the reinforcing bar embedded in concrete and the force is transferred from the bar to concrete through bonding. Bonding between concrete and reinforcing bars is a combination of three components: chemical adhesion, mechanical interlocking, and friction between concrete and the bar (Mitchell *et al.* 1992). For plain bars, chemical adhesion and friction are the main sources of bonding after the slip of the bars. On the other hand, bonding for deformed bars depends mainly upon the mechanical action with slight effects from chemical adhesion, while friction can merely occur after the slip between the reinforcing bars and the concrete.

The type of failure generally depends upon the three aforementioned components of bonding. Because the bonding mechanism of plain bars is characterized by the chemical adhesion and friction, the bonding failure normally involves only the surface between concrete and rebar. In the case of deformed bars, the pullout force is transferred from the rebar to the concrete cover in two directions: perpendicular and parallel to the rebar. In the perpendicular direction, the force is transferred in terms of radial pressure along the perimeter of the concrete cover. This pressure causes the hoop or tangential stresses to split the concrete cover. In the parallel direction, the force is transferred in terms of shear stresses through concrete keys.

The process of pull-out failure for deformed bars involves different stages (Saroushian 1989) as illustrated in Figure 2.1. Figure 2.1 (a) shows the initiation of damage in the form of inclined cracks around the steel lugs that can propagate to splitting failure because of the bearing pressure transferred from the steel. Shear cracking and crushing of concrete keys between the steel lugs may be experienced

due to high shear and compressive stress intensity near the ribs as shown in Figure 2.1 (b). If the shear cracking and crushing is expanded to larger parts, it can lead to complete shearing-off of the concrete keys. After the shearing-off failure, the pullout force is resisted only by friction forces as shown in Figure 2.1 (c). The gradual shearing-off of the concrete keys can occur only if the concrete cover or confinement is sufficient to prevent a severe splitting crack.

According to the above mechanism of bond resistance, the bonding failure can be categorized into three types (Tepfers 1982): 1) shear failure along the perimeter of the bar; 2) splitting failure of the concrete cover; and 3) shearing-off failure. The first type of failure occurs in case of smooth bars with large diameters when the shear strength of concrete along the perimeter of the bar can not resist the pullout force. The splitting failure of the concrete cover occurs if the shear strength of concrete is sufficient to resist the shear force, while the principal tensile stress, which is the tangential stress, exceeds the tensile strength of concrete causing the splitting cracks to radially propagate to the outer perimeter of the concrete cover. The splitting failure is common for pull-out specimens, as well as for real structures, as the primary mode of failure for bonding between the embedded steel bars and the surrounding concrete (Skorobogatov and Edwards 1979; Tepfers 1982; ACI408 2003). The shearing-off failure occurs in concrete between the ribs of the bar. As opposed to the second type of failure, the shearing-off failure occurs if the tensile or splitting strength of the concrete cover is sufficiently high, while the shear strength of concrete cannot resist the shear force, resulting in a shear failure of concrete around the bar lugs along the embedded length. Normally, the bond strength obtained from this type of failure is higher than the other types. In ordinary concrete structures, this type of failure is hardly encountered and can only be examined by using pull-out specimens with short bond length (Tepfers 1982).

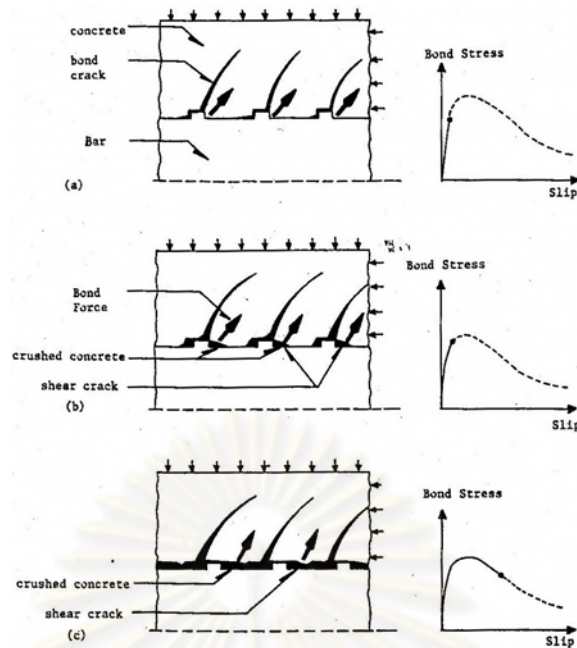


Figure 2.1 Mechanism of bond resistance in confined concrete (Eligehausen 1983):
 (a) inclined cracks at steel lugs; (b) crushing and shear cracking of concrete keys; and
 (c) progressive shearing-off of concrete keys

The relationship between the pull-out bond strength, τ_b , and the shear strength of concrete, f_v , can be expressed as

$$\tau_b = f_v \frac{H}{S} \quad (2.1)$$

in which H and S are the height and spacing of the steel bar ribs, respectively. The bond strength computed based on Eq. (2.1) is usually higher than the bond splitting strength obtained from the experimental results.

The bond-slip relationships for each type of failure can be shown in Figure 2.2. For smooth bars, the slip occurred at the maximum bond stress in shear failure is typically small. For deformed bars, the slip occurred at the maximum bond stress in shearing-off failure is normally larger than splitting failure. It can be observed from Figure 2.2 that in the early stage the bond-slip relationships for different types of failure are very close while the splitting-failure bond models (Eligehausen *et al.* 1983; Harajli *et al.* 1995; Den Uijl and Bigaj 1996) yield the same bond-slip relationships as the shearing-off failure bond models until the splitting bond strength is reached.

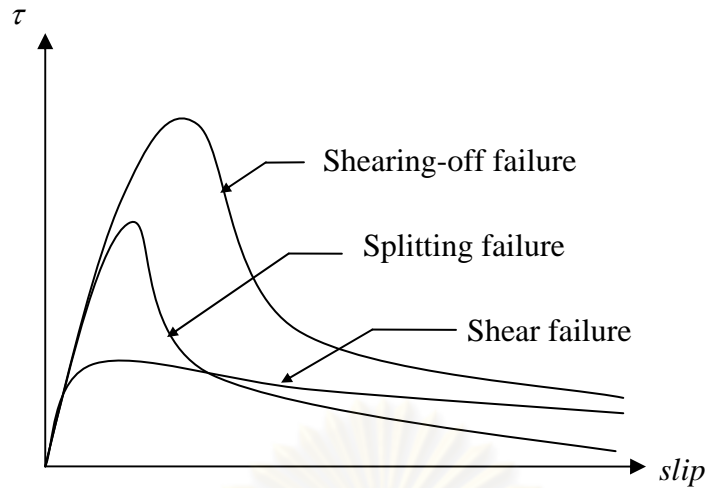


Figure 2.2 Bond stress-slip relationships for different types of failure (Lettow 2004)

2.3 Analytical Model

2.3.1 Relationship between Radial Pressure and Bond Stress

The pullout force between rebar and concrete is transferred mainly through the bearing of rebar ribs on the concrete interface, distributing the compressive stress around the rib surface into the surrounding concrete (see Figure 2.3). Due to the inclined configuration of the ribs, the pullout force can be decomposed into two directions, i.e. parallel and perpendicular to the rebar. Whilst the parallel force is concentrated at the steel-concrete interface, the perpendicular force is regarded as an internal pressure in the concrete cylinder and can be used to determine the bond stress (τ) and the bond strength (τ_b) for splitting failure. Based on the study of Tepfers (1979), the internal pressure from the pull-out load (p_p) can be considered to be equilibrated by the pressure resistance of the concrete cover (p_c)

$$p_p = p_c \quad (2.2)$$

and the association between the radial pressure of the pull-out load and the bond stress can be expressed as:

$$\tau = p_p \cot \alpha \quad \text{or} \quad \tau = p_c \cot \alpha \quad (2.3)$$

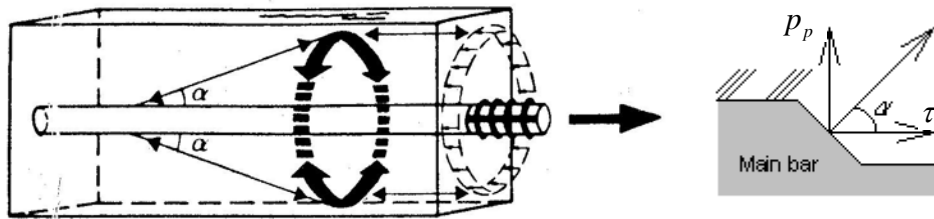


Figure 2.3 Pull-out force transfer between rebar and concrete
(Tepfers 1980 and Takahiro *et al.* 1999)

where the effective face angle $\alpha = 45^\circ$ has been widely adopted to estimate the bond stress at normal temperature, i.e. $T = 20^\circ\text{C}$ (Tepfers 1979; Den Uijl and Bigaj 1996; Wang and Liu 2003). Note that the bond stress, τ , in Eq. (2.3) assumes a uniform pullout force distribution along the embedded length of the rebar. This assumption is applicable only for short bond length and the computed bond stress is generally referred to as the local bond stress.

At the elevated temperature, the decreasing mechanical properties of the concrete cover degrade the pressure resistance to the pull-out load. Moreover, the different coefficients of thermal expansion between the rebar and the concrete cover also generate extraneous radial pressure in addition to that from the pull-out force.

2.3.2 Splitting Resistance of Concrete Cover at Elevated Temperatures

Let us consider a pull-out specimen, consisting of a concrete cylinder with an embedded reinforcement bar, subjected to a pullout force that can be modeled as an internal pressure, p , on the cross section of the hollow concrete cylinder as illustrated in Figure 2.4. The internal pressure p is equilibrated by the pressure resistance of the concrete cover along the perimeter of the reinforcement bar. Based on the elastic theory of hollow cylinders with plane stress analysis (Timoshenko 1970), the radial and the tangential stress components of the concrete cover in a cylindrical coordinate system, σ_r and σ_θ , can be expressed as:

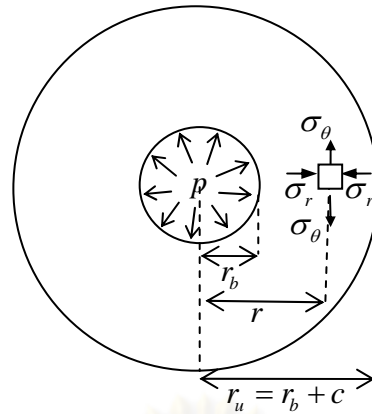


Figure 2.4 Modeling of a pull-out specimen as a hollow concrete cylinder subjected to a uniform pressure on the inner surface

$$\sigma_r(r) = \frac{r_b^2 p}{r_u^2 - r_b^2} \left(1 - \frac{r_u^2}{r^2} \right) \quad (2.4)$$

$$\sigma_\theta(r) = \frac{r_b^2 p}{r_u^2 - r_b^2} \left(1 + \frac{r_u^2}{r^2} \right) \quad (2.5)$$

in which r_b is the inner radius of the concrete cover which is equal to the radius of the rebar;

r_u is the outer radius of the concrete cover; and

r is the radial distance from the center of the concrete cylinder.

Based on the above equations, the imposed radial pressure, p , essentially generates tensile stresses in the circumferential direction, σ_θ , of the concrete around the inner radius r_b of the concrete cover. During the elastic stage, cracking is initiated if σ_θ at the rebar-concrete interface exceeds the tensile strength of concrete as illustrated in Figure 2.5 (a). Based on the work of Tepfers (1982), the current study incorporates the effect of the elevated temperature in computing the pressure resistance of the concrete cover in the elastic stage, $p_{ce,T}$, by substituting σ_θ in Eq. (2.5) with the tensile strength of concrete at an elevated temperature T , $f_{ct,T}$, at the inner radius of the concrete cover (r_b) as follows:

$$p_{ce,T} = f_{ct,T} \frac{r_u^2 - r_b^2}{r_u^2 + r_b^2} \quad (2.6)$$

After the concrete cracks, the concrete cover can be divided into two zones as illustrated in Figure 2.5 (b). The concrete within the outer zone does not crack and sustains its elastic behavior, whereas the concrete is considered cracked throughout the inner zone. The boundary of the inner zone can be specified by the distance at which the splitting cracks propagate to, the so-called inner radius, r_i . Takahiro *et al.* (1999) have recommended neglecting the tensile strength of the cracked concrete within the inner zone. However, this assumption has not been widely accepted, and various cracking concrete models have been employed to analyze the effect of this cracked part (Cairns and Jones 1996; Gambarova and Rosati 1997; Nielsen and Bicanic 2002). Compared with other models, the tensile softening crack model or the smear crack theory seems advantageous in terms of its ability to accurately represent discrete crack openings, which are impossible to count in real structures, in an average sense.

Prior to cracking, the relationship between the tensile stress, σ_{ct} , and the tensile strain, ε_t , in concrete can be considered linear-elastic. Based on the tensile softening model, cracking of concrete can be regarded as a process of softening once the tensile strain ε_t is higher than the elastic tensile strain limit, $\varepsilon_{ct,T}$, as illustrated in Figure 2.6 (Petersson 1981; Wittmann *et al.* 1988; CEB-90 (1991); Guinea *et al.* 1994; Pantazopoulou *et al.* 2001; Bazant 2002). The tensile stress-strain relationship in Figure 2.6 can be expressed as:

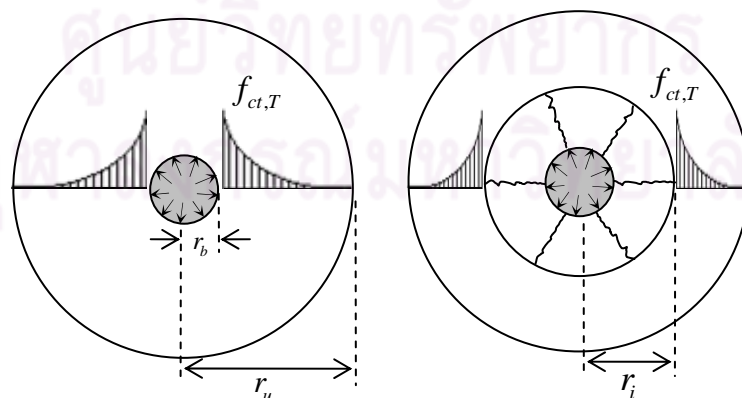


Figure 2.5 Distribution of tensile ring stresses in (a) elastic and (b) partly cracked elastic (Tepfers 1982)

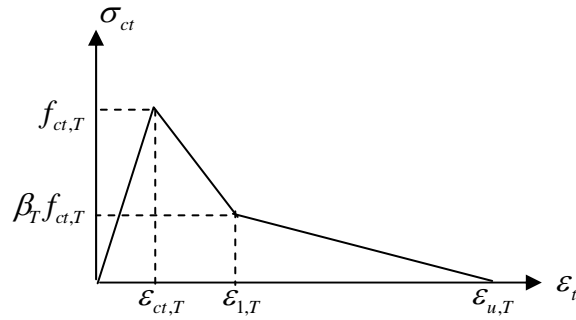


Figure 2.6 Stress–strain relationship for concrete in tension

$$\begin{aligned}
 \sigma_{ct} &= E_{c,T} \varepsilon_t && \text{for } \varepsilon_t \leq \varepsilon_{ct,T} \\
 \sigma_{ct} &= f_{ct,T} \left[1 - \frac{(1 - \beta_T)(\varepsilon_t - \varepsilon_{ct,T})}{\varepsilon_{1,T} - \varepsilon_{ct,T}} \right] && \text{for } \varepsilon_{ct,T} < \varepsilon_t \leq \varepsilon_{1,T} \\
 \sigma_{ct} &= \beta_T f_{ct,T} \frac{\varepsilon_{u,T} - \varepsilon_t}{\varepsilon_{u,T} - \varepsilon_{1,T}} && \text{for } \varepsilon_{1,T} < \varepsilon_t \leq \varepsilon_{u,T}
 \end{aligned} \tag{2.7}$$

in which σ_{ct} is the tensile stress of concrete (MPa);

β_T is the multiplier of the tensile strength at the kink point in the bilinear softening model;

$E_{c,T}$ is the initial elastic modulus of concrete (MPa) at the temperature T ;

ε_t is the tensile strain of concrete (mm/mm);

$\varepsilon_{ct,T}$ is the tensile strain of concrete (mm/mm) at initial cracking at the

temperature T , $\varepsilon_{ct,T} = \frac{f_{ct,T}}{E_{c,T}}$;

$\varepsilon_{1,T}$ is the tensile strain at the kink point in the bilinear softening model at the temperature T ; and

$\varepsilon_{u,T}$ is the tensile strain which corresponds to zero residual tensile strength at the temperature T .

It can be seen from Figure 2.6 that concrete can still sustain the residual tensile capacity through its softening behavior and the internal pressure can still be transferred to the outer zone of the concrete cover through the cracked part (Tepfers 1973; Aiello 2001; Wang and Liu 2003). As a result, the splitting resistance, $p_{c,T}(r_i)$,

of concrete can be computed as a summation of the pressure resistance of the outer zone, $p_{co,T}(r_i)$ and the pressure resistance of the inner zone, $p_{ci,T}(r_i)$, as illustrated in Figure 2.7 according to the following pressure equilibrium equation.

$$2\pi r_b p_{c,T}(r_i) = 2\pi r_i p_{co,T}(r_i) + 2\pi r_b p_{ci,T}(r_i) \quad (2.8)$$

or

$$p_{c,T}(r_i) = \frac{(r_i p_{co,T}(r_i) + r_b p_{ci,T}(r_i))}{r_b} \quad (2.9)$$

The pressure resistance of concrete in the outer zone, which is in elastic stage, is acquired by substituting the term r_b in Eq. (2.6) with r_i as shown in Eq. (2.10) whereas the pressure resistance of concrete in the inner zone, which is in the cracked stage, can be computed by integrating the tangential stress over the cracked inner part as shown in Eq. (2.11).

$$p_{co,T}(r_i) = f_{ct,T} \left(\frac{r_u^2 - r_i^2}{r_u^2 + r_i^2} \right) \quad (2.10)$$

$$p_{ci,T}(r_i) = \frac{\int_{r_b}^{r_i} \sigma_{ct}(r) dr}{r_b} \quad (2.11)$$

in which $\sigma_{ct}(r)$ is the tensile stress of the cracked inner part of concrete in accordance with Eq. (2.7).

The tensile stress of the cracked inner concrete can be analyzed by neglecting the Poisson's effect and assuming that the radial displacement, $u_{rc}(r < r_i)$, is constant throughout the cracked part and equal to the radial displacement at the inner radius, $u_{rc}(r_i)$, as illustrated in Eq. (2.12) and Eq. (2.13) (Wang and Liu 2003).

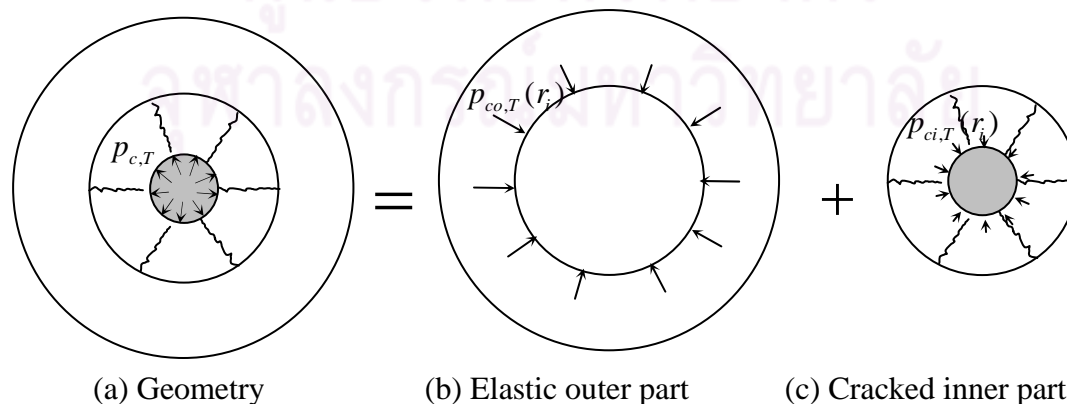


Figure 2.7 The pressure resistance model for a partially cracked concrete cylinder
(Wang and Liu 2003)

$$u_{rc}(r_i) = r_i \varepsilon_{ct,T} = u_{rc}(r) = r \varepsilon_t \quad \text{for } r_b \leq r < r_i \quad (2.12)$$

or

$$\varepsilon_t = \frac{r_i}{r} \varepsilon_{ct,T} \quad \text{for } r_b \leq r < r_i \quad (2.13)$$

The tangential strain of the cracked concrete represented in Eq. (2.13) can be converted to the tensile stress by using Eq. (2.7) in which the integral in Eq. (2.11) can be solved:

$$\int_{r_b}^{r_i} \sigma_{ct}(r) dr = \frac{f_{ct,T}}{\varepsilon_{1,T} - \varepsilon_{ct,T}} \left[(\varepsilon_{1,T} - \beta_T \varepsilon_{ct,T})(r_i - r_b) - (1 - \beta_T) r_i \varepsilon_{ct,T} \ln \frac{r_i}{r_b} \right]$$

for $\frac{r_i}{r_b} < \frac{r_u}{r_b} \leq \frac{\varepsilon_{1,T}}{\varepsilon_{ct,T}}$

$$\int_{r_b}^{r_i} \sigma_{ct}(r) dr = I_1 + I_2 \quad \text{for } \frac{\varepsilon_{1,T}}{\varepsilon_{ct,T}} < \frac{r_i}{r_b} < \frac{r_{u,T}}{r_b} \leq \frac{\varepsilon_{u,T}}{\varepsilon_{ct,T}} \quad (2.14)$$

where

$$I_1 = \int_{r_b}^{r_i} \sigma_{ct}(r) dr = \frac{(1 - \beta_T) f_{ct,T}}{\varepsilon_{u,T} - \varepsilon_{1,T}} \left[\varepsilon_{u,T} \frac{r_i \varepsilon_{ct,T} - r_b \varepsilon_{1,T}}{\varepsilon_{1,T}} - r_i \varepsilon_{ct,T} \ln \frac{r_i \varepsilon_{ct,T}}{r_b \varepsilon_{1,T}} \right]$$

$$I_2 = \int_{r_i}^{r_b} \sigma_{ct}(r) dr = \frac{f_{ct,T}}{\varepsilon_{1,T} - \varepsilon_{ct,T}} \left[(\varepsilon_{1,T} - \beta_T \varepsilon_{ct,T}) r_i \frac{(\varepsilon_{1,T} - \varepsilon_{ct,T})}{\varepsilon_{1,T}} - (1 - \beta_T) r_i \varepsilon_{ct,T} \ln \frac{\varepsilon_{1,T}}{\varepsilon_{ct,T}} \right]$$

with $r_i = \frac{r_i \varepsilon_{ct,T}}{\varepsilon_{1,T}}$

The computed tensile stress can then be used to solve for $p_{c,T}(r_i)$ and $p_{ci,T}(r_i)$ in Eq. (2.9) and Eq. (2.11), respectively. The maximum pressure resistance of the concrete cover, $\max(p_{c,T})$, is required to solve for the bond strength based on Eq. (2.2) and Eq. (2.3) which can be calculated by differentiating $p_{c,T}(r_i)$ in Eq. (2.15) with respect to r_i and set to zero.

$$\frac{dp_{c,T}(r_i)}{dr_i} = \frac{1}{r_b} \left(\left(\frac{r_u^4 - r_i^4 - 4r_i^4 r_u^4}{(r_u^2 - r_i^2)^2} \right) f_{ct,T} + \frac{d \left(\int_{r_b}^{r_i} \sigma_t(r) dr \right)}{dr_i} \right) = 0 \quad (2.15)$$

where

$$\frac{d\left(\int_{r_b}^{r_i} \sigma_t(r) dr\right)}{dr_i} = \frac{f_{ct,T}}{(\varepsilon_{1,T} - \varepsilon_{ct,T}) r_b} \left[(\varepsilon_{1,T} - \beta_T \varepsilon_{ct,T}) - (1 - \beta_T) \varepsilon_{ct,T} \left(1 + \ln \frac{r_i}{r_b}\right) \right] \quad \text{for } \frac{r_i}{r_b} < \frac{r_u}{r_b} \leq \frac{\varepsilon_{1,T}}{\varepsilon_{ct,T}}$$

$$= \frac{\beta_T f_{ct,T}}{(\varepsilon_{u,T} - \varepsilon_{1,T}) r_b} \left[\frac{\varepsilon_{ct,T} \varepsilon_{u,T}}{\varepsilon_{1,T}} - \varepsilon_{ct,T} \left(1 + \ln \frac{r_i \varepsilon_{ct,T}}{r_b \varepsilon_{1,T}}\right) \right] + \frac{f_{ct,T}}{r_b} \left[\frac{(\varepsilon_{1,T} - \beta_T \varepsilon_{ct,T})}{\varepsilon_{1,T}} - \frac{(1 - \beta_T) \varepsilon_{ct,T}}{(\varepsilon_{1,T} - \varepsilon_{ct,T})} \ln \frac{\varepsilon_{1,T}}{\varepsilon_{ct,T}} \right]$$

$$\text{for } \frac{\varepsilon_{1,T}}{\varepsilon_{ct,T}} < \frac{r_i}{r_b} < \frac{r_u}{r_b} \leq \frac{\varepsilon_{u,T}}{\varepsilon_{ct,T}}$$

which can be solved for r_i and the corresponding maximum bond strength.

2.3.3 Radial Pressure and Inner Crack Radius at Elevated Temperatures

At the elevated temperature, the transverse coefficient of thermal expansion of the rebar is higher than that of the surrounding concrete. For a specified temperature increment ΔT ($\Delta T = T - 20^\circ \text{C}$), the differential thermal expansion causes the radial pressure, $p_{c,T}$, against the adjacent concrete cover as illustrated in Figure 2.8. During the elastic stage, the circumferential strains of concrete at the reinforcement bar-concrete interface, $\varepsilon_{ic,T}$, is less than the tensile strain of concrete at initial cracking, $\varepsilon_{ct,T}$. Aiello *et al.* (2001) have derived the circumferential strains of concrete and the rebar at the interface as follows:

$$\varepsilon_{ic,T} = \frac{p_{t,T}}{E_{c,T}} \left(\frac{r_u^2 + r_b^2}{r_u^2 - r_b^2} + \nu_c \right) + \alpha_{c,T} \Delta T \quad (2.16)$$

$$\varepsilon_{ib,T} = \alpha_{b,T} \Delta T - \frac{p_{t,T} (1 - \nu_b)}{E_{b,T}} \quad (2.17)$$

from which the thermal radial pressure, $p_{c,T}$, can be computed based on the compatibility of the circumferential strains at the reinforcement bar-concrete interface (i.e., $\varepsilon_{ib,T} = \varepsilon_{ic,T}$) as:

$$p_{c,T} = \frac{(\alpha_{b,T} - \alpha_{c,T}) \Delta T}{\frac{1}{E_{c,T}} \left(\frac{r_u^2 + r_b^2}{r_u^2 - r_b^2} + \nu_c \right) + \frac{1}{E_{b,T}} (1 - \nu_b)} \quad (2.18)$$

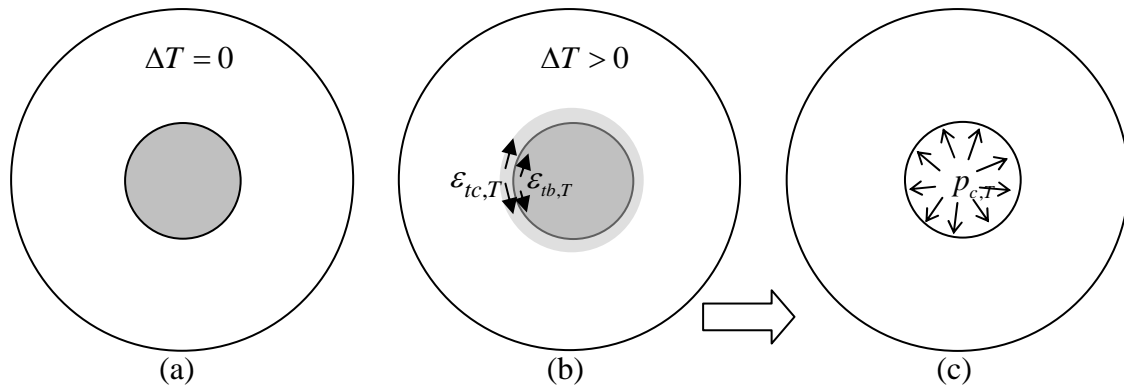


Figure 2.8 Differential thermal expansion of concrete and rebar: (a) cross section of the reinforced concrete cylinder at normal temperature; (b) expansion of the reinforcement bar and the concrete cover with the temperature increment; and (c) radial pressure caused by differential thermal expansion

in which $\epsilon_{tc,T}$ and $\epsilon_{tb,T}$ are the circumferential strains (mm/mm) of concrete and rebar, respectively, at the interface due to thermal expansion;

$\alpha_{c,T}$ and $\alpha_{b,T}$ are the transverse coefficients of thermal expansion of concrete and rebar;

ν_c and ν_b are the Poisson's ratios of concrete and rebar; and

$E_{c,T}$ and $E_{b,T}$ are the elastic moduli of concrete and rebar (MPa) at temperature T .

Once the concrete strain exceeds its tensile capacity, $\epsilon_{ct,T}$, cracking is initiated and propagates to an unknown inner radius r_i . The actual value of the inner radius r_i must be trialed in Equations (2.9) to (2.11) based upon the compatibility of the circumferential strains at the reinforcement bar-concrete interface. The circumferential strain of the reinforcement bar, $\epsilon_{tb,T}$, is generally in the elastic stage due to its high elastic modulus and can be computed by using Eq. (2.17). The circumferential strain of the surrounding concrete in the partially cracked elastic stage with thermal expansion can be computed as

$$\epsilon_{tc,T} = \frac{r_i}{r_b} \epsilon_{ct,T} + \alpha_{c,T} \Delta T \quad (2.19)$$

Figure 2.9 illustrates the computational procedures involved in the thermal radial pressure evaluation.

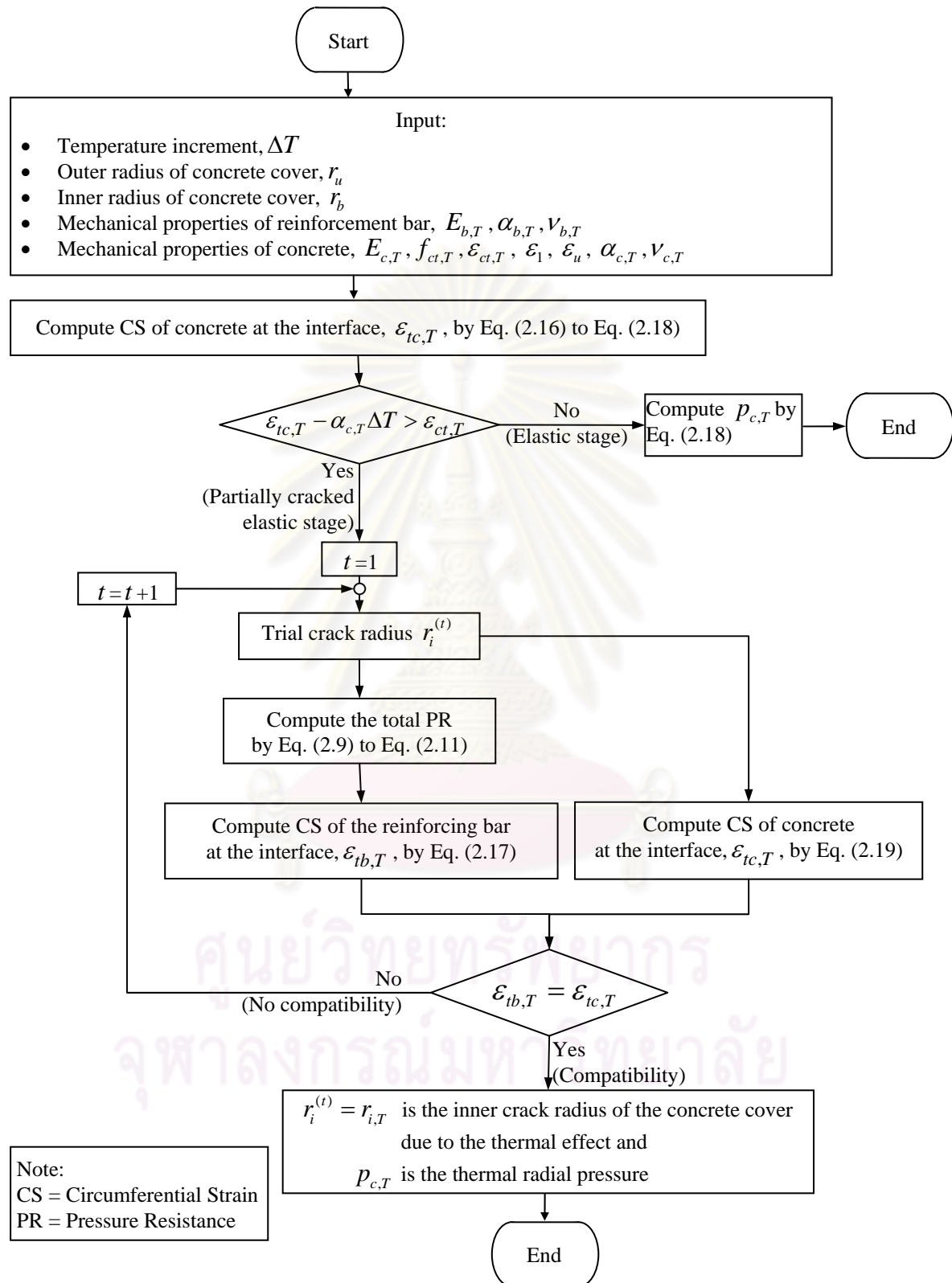


Figure 2.9 Computational procedure for the thermal radial pressure and the inner crack radius due to thermal expansion

2.3.4 Bond Stress at Elevated Temperatures

To investigate the bond stress at elevated temperatures, the effects of the pull-out force and the thermal load must be simultaneously considered. These two effects, coupled with the decreasing mechanical properties of concrete, degrade the splitting resistance of the concrete cover to the pull-out load.

Under the thermal effect, the values of $p_{c,T}$ and $r_{i,T}$ can be computed through the computational procedure illustrated in Figure 2.9. Because the reinforcement bar can be considered to be in full contact with the concrete cover along the interface as shown in Figure 2.10 (a), strain compatibility can be used to compute the thermal pressure. Once the pull-out load is additionally exerted through the reinforcing bar to the concrete cover, the inner crack radius is stretched out and gaps behind the ribs occur (Goto 1971) as illustrated in Figure 2.10 (b). At this stage, the reinforcement bar is in partial contact with the concrete cover along the interface (see Figure 2.10 (c)) and the strain compatibility concept is no longer applicable. The thermal pressure is seen to loosen through the gaps and can be neglected under the pull-out load.

The inner crack radius under the thermal effect, $r_{i,T}$ can be considered to degrade the pressure resistance of the concrete cover as the residual uncracked concrete cover, c' , is decreased as shown in Figure 2.11 (a). The concept is similar to the corrosion model of Wang and Liu (2006). Note that the crack due to thermal effect is modeled first, that is, prior to the pull-out loading of the rebar or the development of bond—as is generally the case in laboratory tests (Diederichs and Scheider 1981; Hertz 1982; Morley and Royles 1983; Haddad *et al.* 2008). Nevertheless, for the cases of simultaneous pull-out loading or partial pull-out loading with the thermal load, this concept is still applicable because the thermal effect causes cracking of the surrounding concrete within the inner zone along the concrete-rebar interface.

The pressure resistance of the residual concrete cover, $p_{c,T}(r_i)$, can be obtained from Eq. (2.9) by substituting r_b with $r_{i,T}$ (see Figure 2.11 (b)). Based on the pressure

equilibrium as shown in Figure 2.11 (b), the pressure resistance of the concrete cover under the thermal effect and the pull-out load, $p_c^{total}(r_i)$, can thus be computed as:

$$p_c^{total}(r_i) = \frac{r_i}{r_b} p_{c,T}(r_i) \quad (2.20)$$

The maximum pressure resistance of the concrete cover under the thermal effect and the pull-out load, $\max(p_c^{total})$, can also be obtained by differentiating $p_c^{total}(r_i)$ in Eq. (2.20) with respect to r_i and set to zero.

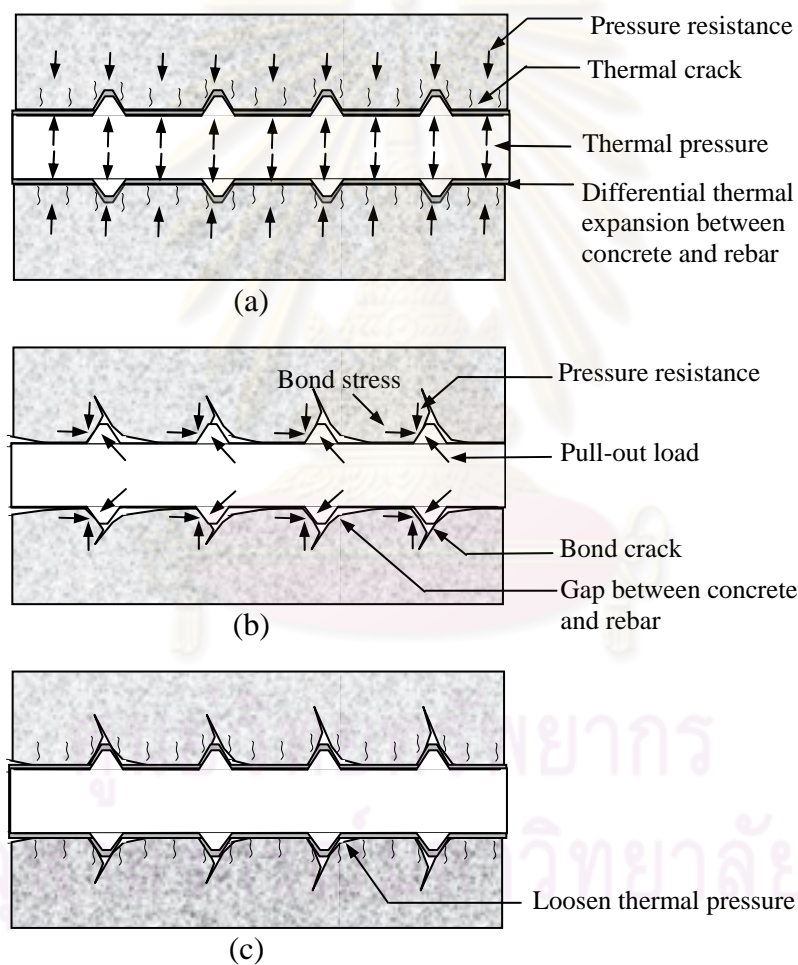


Figure 2.10 Reinforcement bar-concrete interface: (a) under the thermal load only; (b) under the pull-out load only; and (c) under the combined effects of the thermal load and the pull-out load

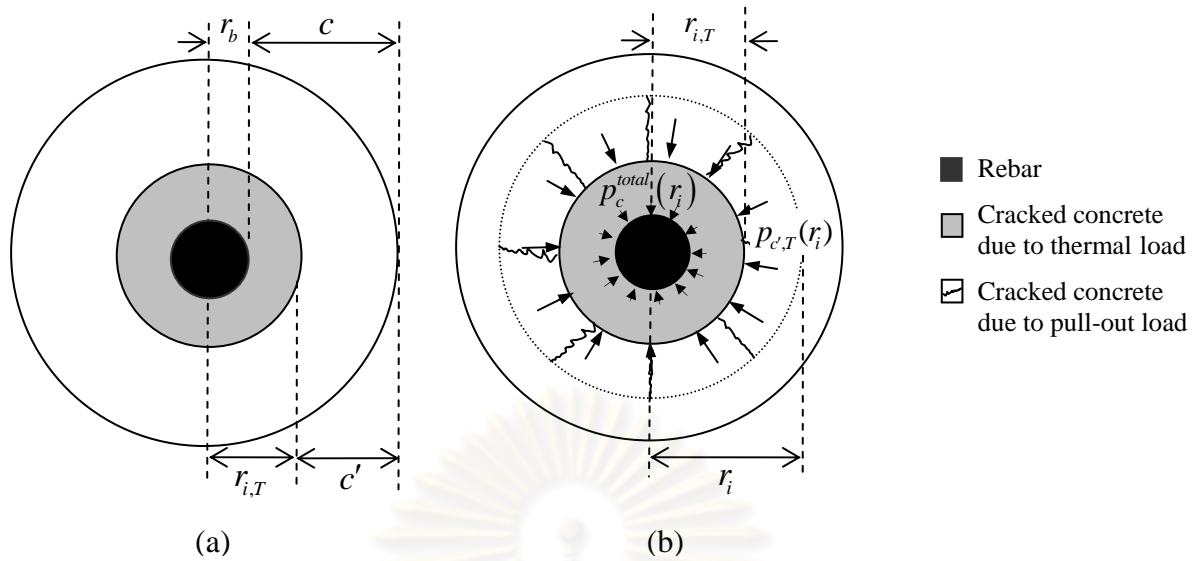


Figure 2.11 Modeling of the pressure resistance of the concrete cover under the pull-out load and the thermal effect: (a) residual concrete cover due to the thermal load; and (b) pressure resistance of the concrete cover.

The bond stress τ_T and bond strength $\tau_{b,T}$ under the elevated temperature T and the pull-out load can then be computed by substituting $p_c^{total}(r_i)$ and $\max(p_c^{total})$ for p_p in Eq. (2.3), respectively, as follows:

$$\tau_T = p_c^{total}(r_i) \cot \alpha \quad (2.21)$$

$$\tau_{b,T} = \max(\tau^{total}) = \max(p_c^{total}) \cot \alpha \quad (2.22)$$

2.4 Variation of Bond Strength with respect to Bond Length

As previously mentioned, the current study adopts the tensile softening model for cracked concrete to evaluate the bonding behavior of reinforced concrete at elevated temperatures. Previous experimental results on bond strengths published in the literature will be used to assess the efficacy of the proposed model. However, the proposed model assumes a uniform distribution of bond stress along a local embedded length of the reinforcing steel bar while the actual bond stress distribution generally varies as shown in Figure 2.12. As such, the bond strength obtained from testing must be converted to the local bond strength to allow a direct comparison between the test results and the modeling results.

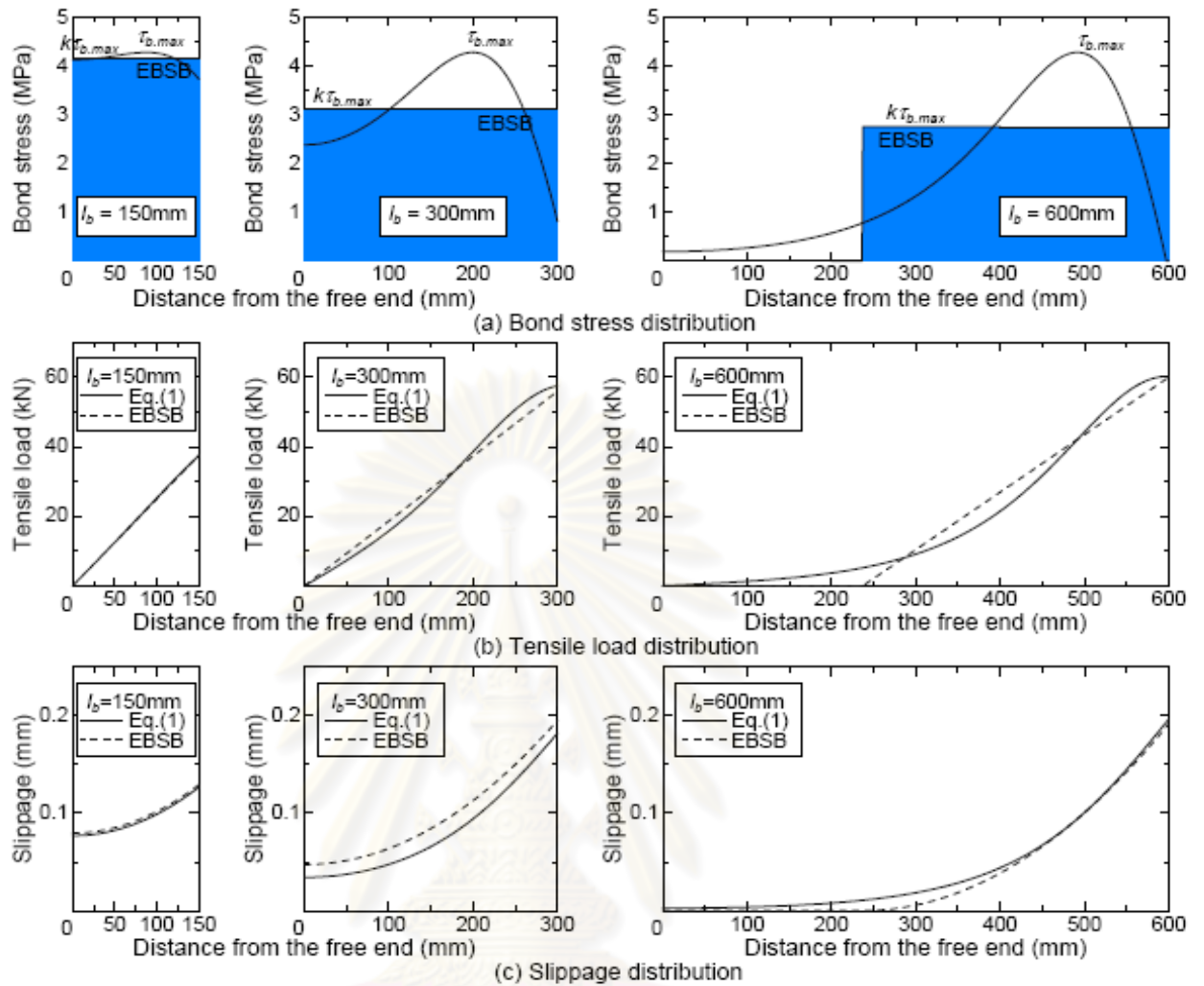


Figure 2.12 The bond stress, tensile load, and slippage distribution
(Yasojima and Kanakubo 2005)

The tested bond strength is generally computed as:

$$\tau_{b,test} = \frac{F}{\pi d_b l_b} \quad (2.23)$$

in which $\tau_{b,test}$ is the average bond strength (MPa) from testing;

F is the maximum pullout force (N);

d_b is the diameter of the reinforcement bar (mm);

l_b is the embedded length of the reinforcement bar (mm); and

πd is the perimeter of the bar (mm).

Yasojima and Kanakubo (2005) have proposed the use of an equivalent bond stress block (EBSB) to approximate the bond stress distribution as shown in Figure 2.12 in which the equivalent bond stress, τ_{EBSB} , is computed as a proportion of the maximum local bond stress, $\max(\tau_b)$:

$$\tau_{EBSB} = k\tau_b \quad (2.24)$$

in which k is a constant ranging between 0 and 1 that can be computed as

$$k = \frac{\int_{s_{x2}}^{s_{x1}} \tau_s ds}{s_{x1} - s_{x2}} \quad (2.25)$$

The value of τ_s in the above equation is expressed as

$$\tau_s = 20.4 f_{ct} s \frac{(r_u / 2r_b)^2 - (10.2s)^2}{(r_u / 2r_b)^2 + (10.2s)^2} \cot \alpha \quad (2.26)$$

in which τ_s is the bond stress function with respect to the slippage (Takahiro *et al.* 1999);

s is the slippage;

s_{x1} is the slippage of the loaded end at the maximum tensile load in the pull-out specimens;

s_{x2} is the slippage of the free end; and

l_e is the effective bond length (i.e., the length between the maximum loaded end and the free end).

Yasojima and Kanakubo (2005) have proposed the formulation of l_e and k based on Sakai's bond stress function (Sakai *et al.* 1999) as follows:

$$l_e = \sqrt{\frac{2E_b a_b}{(2 \log 2 - 1) f_{ct} \phi_b \cot \alpha}} \quad (2.27)$$

$$k = \frac{1 - 0.643}{2} \cos\left(\left(l_b / l_e\right)^2 \pi\right) + \frac{1 + 0.643}{2} \quad (2.28)$$

in which E_b is the elastic modulus of the reinforcement bar (MPa);

a_b is the cross-sectional area of the reinforcement bar (mm²);

ϕ_b is the perimeter of the reinforcement bar (mm); and

f_{ct} is the tensile strength of the concrete (MPa).

2.5 Variation of Steel and Concrete Properties with Temperature

The variation of mechanical and thermal properties of steel and concrete with temperature is required to evaluate the bonding behavior of reinforced concrete structures at elevated temperatures.

2.5.1 Concrete under and after High Temperatures

Under high temperatures, concrete normally changes its chemical composition, physical structure, and water content. Between the temperature of 30 and 120°C, the evaporable water is released from saturated concrete causing vapor pressure. At this stage, concrete cracking or spalling is initiated. At about 300°C, concrete is further dehydrated from the expulsion of chemically bound water in hardened paste. However, the primary changes in concrete properties initiate upon the dissociation of calcium hydroxide (CH) from the hardened cement paste (HCP) at 400°C. As the temperature rises up to 500°C, the expulsion of water from both gel pores and capillaries leads to a significant increase in the average pore volume as well as a change in the pore system from an isolated to an interconnected network. When the temperature exceeds 500°C, calcium hydroxide and calcium silicates hydrate (C-S-H) in the cement paste decompose, until C-S-H collapses at 900 °C (Bazant and Kaplan 1996).

The heat resistance of concrete depends on the type of aggregates. Siliceous aggregates break down at temperatures above 500 °C while carbonic aggregates decompose at much higher temperatures. Aggregate melting or fusion occurs above 1200°C, leading to complete concrete collapses (Bazant and Kaplan 1996). Because the physical change and chemical decomposition of concrete may cause cracks and/or explosive spalling, these changes can decrease the mechanical properties and increase in the permeability of concrete. Furthermore, in case of reinforced concrete, the bond strength between concrete and the embedded steel is affected.

Poon *et al.* (2001) have reported that the temperatures of greater than 300 °C and long exposure duration can cause a significant drop of concrete strength. Moreover, the types of aggregate, use of additives, and shape or size of specimen influence the loss in concrete strength after fire.

Arioz (2007) has investigated the effects of elevated temperatures on the properties of concrete. It has been suggested that the expansion of aggregates plays a significant role in the reduction of compressive strength of concrete after exposure to high temperatures. The relative residual strength of concrete for concrete mixtures with river gravel aggregates is lower than that of limestone aggregates. For instance, after exposure to the temperature level of 500°C, the residual strength of limestone concrete is higher than the river-gravel concrete for approximately 30%. These results agree well with Hertz (2005)'s explanation that siliceous aggregates highly expand and cause the greatest damage. On the other hand, limestone aggregates have lower thermal expansion. As a result, concrete produced with limestone has less damage.

Even though the concrete properties can significantly deteriorate after fire, some recovering behaviors have been reported in the literature. Poon *et al.* (2001) have investigated the recovery of fire-damaged concrete after post-fire curing. The recovery includes the strength and durability of the concrete. In their study, the concrete was exposed to elevated temperatures of up to 800°C. After the heating period, the tested concrete was naturally cooled, and then cured in water in a controlled environment. Subsequently, the changes in the macro- and micro-structure of the concrete were examined. The experimental data indicate that concrete has recovered substantial strength and durability. However, the recovery depends on the types of concrete, exposure temperature, cooling method and curing duration. It has also been found that the recovery is a result of rehydration processes that regenerate calcium-silicate-hydrate (C-S-H) and fill the internal cracks, capillaries, and honey combs damaged during the fire. This study agrees well with the works of Khoury (1992) and Sarshar and Khoury (1993).

2.5.2 Variation of Thermal and Mechanical Properties of Steel and Concrete with Temperature

Several researchers (Sebastjan *et al.* 2005; Kodur and Dwaikat 2008) have referred to the Eurocodes to assess behaviors of RC structures under and after fire. For the current study, we also adopt most of the thermal and mechanical properties of steel and concrete at elevated temperatures based on the Eurocodes. The variation of the tensile strength of concrete with temperature is based on other references (Bazant and Chern 1987) since the properties given by the Eurocodes significantly differ from other researchers and the estimate of the tensile strength obtained from the Eurocodes is zero for temperatures higher than 600°C. Moreover, the fracture mechanic model is employed to generate the tensile stress–strain relationship of concrete at high temperatures, which is not specified in the Eurocodes. The thermal and mechanical properties of steel and concrete adopted for the current study are summarized in Table 2.1 to Table 2.4.

Table 2.1 Variation of thermal properties of concrete and steel with temperature

Properties	Variation of Thermal Properties with Temperature	References
Specific heat of reinforcing steel, $c_{s,T}$ (J/kg-°C)	$c_{s,T} = 425 + 7.73 \times 10^{-1}T - 1.69 \times 10^{-3}T^2 + 2.22 \times 10^{-6}T^3$ for $20^\circ\text{C} \leq T \leq 600^\circ\text{C}$	EC3 (2005)
Thermal conductivity of reinforcing steel, $k_{s,T}$ (W/m-°C)	$k_{s,T} = 54 - 3.33 \times 10^{-2}T$ for $20^\circ\text{C} \leq T \leq 800^\circ\text{C}$	
Specific heat of concrete, $c_{c,T}$ (J/kg-°C)	$c_{c,T} = 900$ for $20^\circ\text{C} \leq T \leq 100^\circ\text{C}$ $c_{c,T} = 900 + (T - 100)$ for $100^\circ\text{C} < T \leq 200^\circ\text{C}$ $c_{c,T} = 900 + (T - 200) / 2$ for $200^\circ\text{C} < T \leq 400^\circ\text{C}$ $c_{c,T} = 1100$ for $400^\circ\text{C} < T \leq 1200^\circ\text{C}$	EC2 (2004)
Thermal conductivity of concrete, $k_{c,T}$ (W/m-°C)	The lower limit: $k_{c,T} = 1.36 - 0.136(T/100) + 0.0057(T/100)^2$ for $20^\circ\text{C} < T \leq 1200^\circ\text{C}$ The upper limit: $k_{c,T} = 2 - 0.245(T/100) + 0.0107(T/100)^2$ for $20^\circ\text{C} < T \leq 1200^\circ\text{C}$	

Table 2.2 Variation of mechanical properties of steel with temperature

Temperature, T ($^{\circ}\text{C}$)	$\frac{f_{y,T}}{f_{y,20^{\circ}\text{C}}}$ (EC2 2004)	$\frac{E_{s,T}}{E_{s,20^{\circ}\text{C}}}$ (EC2 2004)	ν_s (EC3 2005)	α_s ($1/^{\circ}\text{C}$) (EC3 2005)
20	1.00	1.00	0.3	12.0×10^{-6}
100	1.00	1.00	0.3	12.0×10^{-6}
200	1.00	0.90	0.3	12.0×10^{-6}
300	1.00	0.80	0.3	12.0×10^{-6}
400	1.00	0.70	0.3	12.0×10^{-6}
500	0.78	0.60	0.3	12.0×10^{-6}
600	0.47	0.31	0.3	12.0×10^{-6}

Table 2.3 Variation of mechanical properties of concrete with temperature

Properties	Variation of Mechanical Properties with Temperature	References
Modulus of elasticity, $E_{c,T}$	$E_{c,20^{\circ}\text{C}} = 22000(f_{c,20^{\circ}\text{C}}/10)^{0.3}$	EC2 (2004)
	$E_{c,T}/E_{c,20^{\circ}\text{C}} = \frac{2f_{c,T}/\varepsilon_{c1,T}}{2f_{c,20^{\circ}\text{C}}/\varepsilon_{c1,20}}$	EC2 (2004)
Compressive stress-strain relationship, $\sigma_{c,T} - \varepsilon_{c,T}$	$\sigma_{c,T} = \frac{3\varepsilon_{c,T}f_{c,T}}{\varepsilon_{c1,T} \left[2 + \left(\varepsilon_{c,T}/\varepsilon_{c1,T} \right)^3 \right]}$ for $\varepsilon_{c,T} \leq \varepsilon_{c1,T}$ $\sigma_{c,T} = f_{c,T} \left[1 - \frac{\varepsilon_{c,T} - \varepsilon_{c1,T}}{\varepsilon_{cu,T} - \varepsilon_{c1,T}} \right]$ for $\varepsilon_{c1,T} < \varepsilon_{c,T} \leq \varepsilon_{cu,T}$	EC2 (2004)
Poisson's ratios, ν_c	$\nu_c = 0$ for cracked concrete $\nu_c = 0.2$ for uncracked concrete	EC2 (2004)
Tensile strength, $f_{ct,T}$	$f_{ct,20^{\circ}\text{C}} = 0.3f_{c,20^{\circ}\text{C}}^{2/3}$ for strength classes $\leq \text{C50/60}$	EC2 (2004)
	$f_{ct,20^{\circ}\text{C}} = 2.12 \ln(1 + f_{c,20^{\circ}\text{C}}/10)$ for strength classes $> \text{C50/60}$	
	$f_{ct,T}/f_{ct,20^{\circ}\text{C}} = -0.000526T + 1.01052$ for $20^{\circ}\text{C} < T \leq 400^{\circ}\text{C}$ $f_{ct,T}/f_{ct,20^{\circ}\text{C}} = -0.0025T + 1.8$ for $400^{\circ}\text{C} < T \leq 600^{\circ}\text{C}$	Bazant and Chern (1987)
Coefficient of thermal expansion of concret, $\alpha_{c,T}$ ($1/^{\circ}\text{C}$)	$\alpha_{c,T} = 10 \times 10^{-6}$	EC2 (2004)

Note:

 $f_{c,T}$ is the compressive strength of concrete referred to Table 2.4; $\varepsilon_{c1,T}$ is the peak strain of concrete referred to Table 2.4; and $\varepsilon_{cu,T}$ is the ultimate strain of concrete referred to Table 2.4.

Table 2.4 Variation of compressive strength, peak strain and ultimate strain of concrete with temperature

Temperature, T ($^{\circ}\text{C}$)	Siliceous Concrete			Calcareous Concrete		
	$\frac{f_{c,T}}{f_{c,20^{\circ}\text{C}}}$	$\epsilon_{c1,T}$	$\epsilon_{cu,T}$	$\frac{f_{c,T}}{f_{c,20^{\circ}\text{C}}}$	$\epsilon_{c1,T}$	$\epsilon_{cu,T}$
20	1.00	0.0025	0.0200	1.00	0.0025	0.0200
100	1.00	0.0040	0.0225	1.00	0.0040	0.0225
200	0.95	0.0055	0.0250	0.97	0.0055	0.0250
300	0.85	0.007	0.0275	0.91	0.007	0.0275
400	0.75	0.010	0.0300	0.85	0.010	0.0300
500	0.60	0.015	0.0325	0.74	0.015	0.0325
600	0.45	0.025	0.035	0.60	0.025	0.035

2.5.3 Tensile Stress–Strain Relationship of Concrete at Elevated Temperatures

The typical load-deformation response of concrete in uniaxial tension (see, for example, Figure 2.13) can be divided into the two stages: 1) pre-peak stage and 2) post-peak stage. In the early pre-peak stage, the concrete sustains its elastic behavior and no crack occurs. Under the increasing load, micro-cracks gradually occur throughout the concrete. After the peak load, the cracks are stretched and opened but limited in a specific damage zone, the so-called fracture process zone. The fracture process zone causes the decreasing tension capacity of concrete or the softening behavior. In the post-peak stage, the displacement of concrete depends on the stress-strain relationship of concrete in the micro-crack zone and the stress-crack width relationship of the concrete in the fracture process zone.

Based on the typical load-deformation response, the tensile stress–strain relationship of concrete can be established. In the pre-peak stage and the micro-crack zone, the relationship between the tensile stress and strain of concrete is normally assumed to be linear-elastic prior to cracking, with a slope of the initial modulus of elasticity (Pantazopoulou and Papoulia 2001). In the post-peak stage, the stress-crack width relationship takes the major part in the tensile stress–strain relationship. The stress-crack width relationship is normally assumed bi-linear as shown in Figure 2.14

(Roelfstra and Wittmann 1986; Bazant 2002). Under the normal-temperature condition ($T = 20^\circ\text{C}$), the area under the bi-linear relationship is governed by the fracture energy:

$$G_{f,20^\circ\text{C}} = 0.5(\alpha_{20^\circ\text{C}} + \beta_{20^\circ\text{C}})w_{u,20^\circ\text{C}}f_{ct,20^\circ\text{C}} \quad (2.29)$$

which is defined as the energy dissipated because of the fracture process zone per unit length of fracture. To consider the corresponding smeared values of strain, the crack width, w , is divided by the characteristic crack-band width h_c so that

$$\varepsilon_t = \frac{w}{h_c} \quad (2.30)$$

Based on the results of Bazant and Oh (1983), h_c is approximately 5 times of the maximum aggregate size and h_c can be taken as 100 mm (Pantazopoulou and Papoulia 2001)

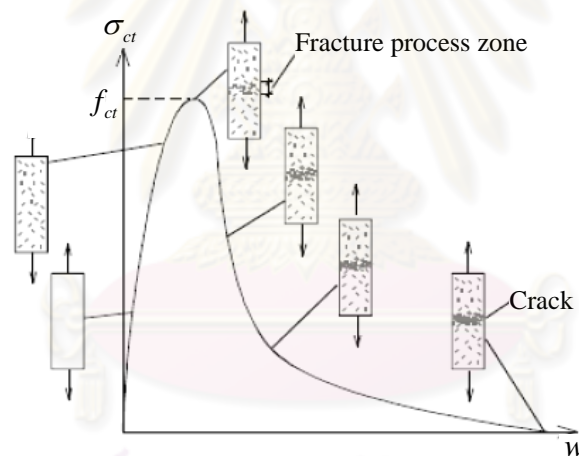


Figure 2.13 Typical load-deformation response of concrete in uniaxial tension

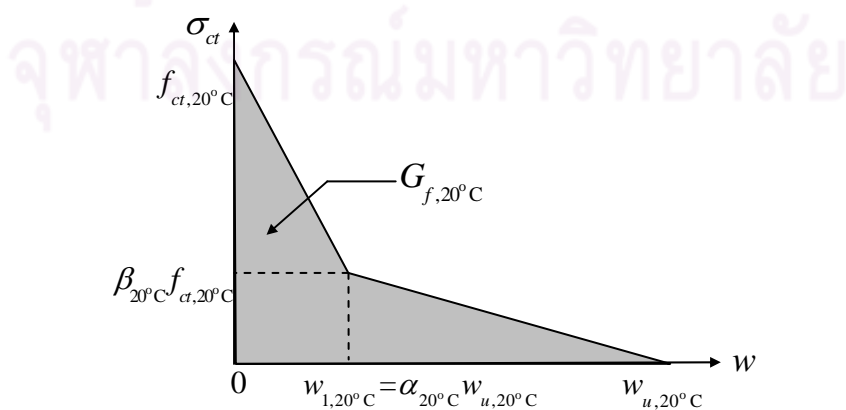


Figure 2.14 Tensile stress-crack width relationship at normal temperature

Following the works of Roelfstra and Wittmann (1986) and Walraven *et al.* (1993), the values of $\alpha_{20^\circ\text{C}}$, $\beta_{20^\circ\text{C}}$ and $w_{u,20^\circ\text{C}}$ are assumed to be 0.14, 0.25 and 0.2 mm, respectively. The value of $G_{f,20^\circ\text{C}}$ can be computed using Eq. (2.29) as

$$G_{f,20^\circ\text{C}} = 0.039f_{ct,20^\circ\text{C}} \quad (2.31)$$

The $\beta_{20^\circ\text{C}}$ value of 0.25 agrees with the study of Rokugo *et al.* (1989). Note that the stress at the kink point normally varies between $0.15f_{ct,20^\circ\text{C}}$ and $0.33f_{ct,20^\circ\text{C}}$ (Bazant 2002). By assuming the linear-elastic relationship in the pre-peak stage and the stress-crack width relationship in the post-peak stage, the tensile stress–strain relationship of concrete can be illustrated as shown in Figure 2.15.

At the elevated temperature T , the bi-linear tensile stress–strain relationship after the post-peak stage becomes more gradual. Moreover, the value of the fracture energy $G_{f,T}$ can significantly vary because of the thermal effect as shown in Table 2.5 (Zhang and Bicanic 2002). Because the damage of concrete is more diffused at the elevated temperatures, the overall behavior is more ductile and the $G_{f,T}$ value increases at least up to 300°C (Taerwe *et al.* 2008). To generate the tensile stress–strain relationship at the elevated temperature T , the current study adopts the same values of β_T and $w_{u,T}$ as for the normal-temperature case (i.e., 0.25 and 0.2 mm) but varies α_T based on Eq. (2.29) according to $G_{f,T}$ and $f_{ct,T}$:

$$\alpha_T = \frac{2G_{f,T}}{w_{u,20^\circ\text{C}}f_{ct,T}} - \beta_{20^\circ\text{C}} \quad (2.33)$$

The normalized tensile stress–strain relationship for concrete at elevated temperatures is shown in Figure 2.17.

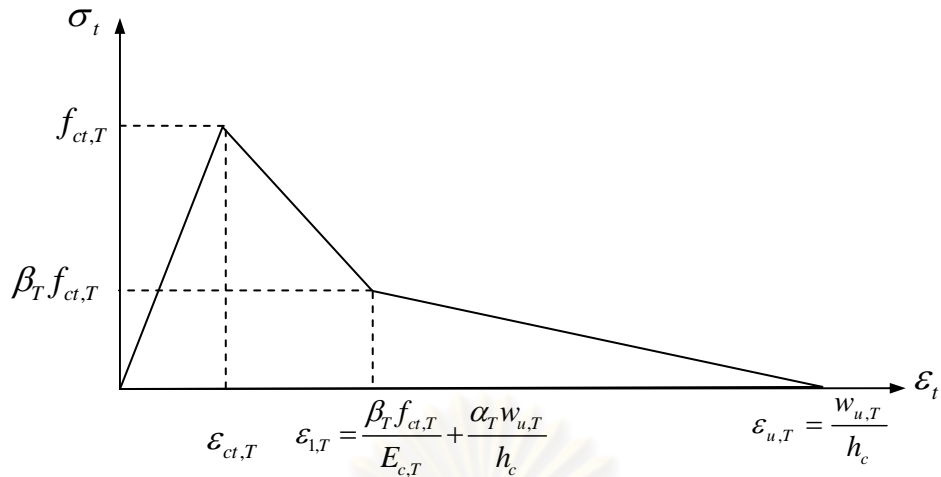


Figure 2.15 Tensile stress–strain relationship for concrete at temperature T

Table 2.5 Variation of the normalized fracture energy $G_{f,T} / G_{f,20^\circ C}$ with temperature (Zhang and Bicanic 2002)

Temperature (°C)	Normal strength concrete ($f_{c,20^\circ C} \leq 57.4$ MPa)	High strength concrete ($f_{c,20^\circ C} \leq 77.6$ MPa)
20	1.00	1.00
100	1.29	1.26
200	1.52	1.48
300	1.57	1.59
400	1.45	1.52
500	1.29	1.37
600	0.81	1.15

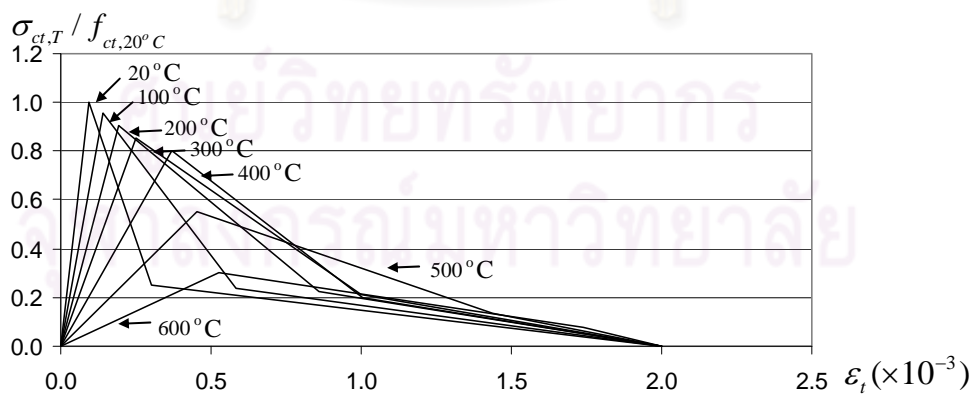


Figure 2.17 The normalized tensile stress–strain relationship for concrete at elevated temperatures

CHAPTER III

VERIFICATION OF THE ANALYTICAL MODEL

3.1 Introduction

In this chapter, the efficacy of the model proposed in the previous chapter to predict the bond strength for reinforced concrete at normal and elevated temperatures is verified based upon the following key points:

- the ability of the tensile softening model for cracked concrete to predict the splitting bond strength at normal temperature;
- the ability of the proposed model to predict the thermal radial pressure and the corresponding inner crack radius caused by the differential thermal expansion of the rebar and concrete; and
- the ability of the proposed model to predict the bond strength for reinforced concrete at elevated temperatures.

It should be noted herein that due to the scarcity of the previous experimental data on the thermal radial pressure and the corresponding crack radius for steel rebars embedded in concrete at elevated temperatures, the experimental results for FRP rebars are also adopted for the model verification. Furthermore, since the investigation of the bonding effect on the behavior of reinforced concrete structures requires the bond-slip relationship, in this chapter we also establish the relationship between the bond-slip curve and the proposed model based on previous experimental results. Finally, the bond-slip relationships obtained from the proposed model are compared with the results of the previous studies.

3.2 Tensile Softening Crack Model for Concrete at Normal Temperature

The ability of the tensile softening crack model for concrete to predict the splitting bond strength of steel reinforced concrete at normal temperature can be verified by comparing previous experimental results obtained from the literature with the proposed model. Because the bond strength is related to the tensile strength of the concrete cover, the comparison is done in terms of the bond strength-to-concrete tensile strength ratio, τ_b / f_{ct} (Tepsfer 1979; Wang and Liu 2003; and ACI408 2003). The results are shown in Table 3.1 and Figure 3.1. It can be concluded that the predicted bond strengths agree well with the experimental results.

Table 3.1 Comparison of the predicted bond strengths with previous experimental results for normal temperature

Tested by	d_b (mm)	r_u (mm)	c/d_b	l_b/d_b	f_c (MPa)	f_{ct}^{**} (MPa)	τ_b (MPa)		τ_b / f_{ct}	
							Model	Test	Model	Test
Diederichs and Scheider (1981)	16	86	4.88	5.0	55.0*	3.7	24.7	29.0	6.7	7.8
Morley and Royles (1983)	16	25	1.56	2.0	35.0*	2.8	7.0	7.9	2.5	2.8
	16	32	2.00	2.0	35.0*	2.8	10.9	10.8	3.9	3.9
	16	46	2.88	2.0	35.0*	2.8	11.9	12.8	4.3	4.6
	16	55	3.44	2.0	35.0*	2.8	14.0	16.9	5.0	6.0
Lee <i>et al.</i> (2002)	13	45	3.00	6.0	24.7	2.5	11.2	6.2	4.5	2.5
		45	3.00	6.0	33.0	3.1	13.2	9.1	4.3	2.9
		45	3.00	6.0	42.1	3.6	15.2	12.1	4.2	3.4
		45 ^{***}	3.00	6.0	24.7	2.5	11.2	8.0	4.5	3.2
Al-Negheimish and Al-Zaid (2004)	14	75	4.86	10.7	25.8	2.6	12.7 ^{****}	9.5	4.9	3.7
Xiao and Falkner (2005)	10	50	4.50	5.0	43.0*	3.2	19.9	17.4	6.2	5.4
Haddad <i>et al.</i> (2008)	20	50 ^{***}	2.00	7.5	77.0*	4.1	10.8 ^{****}	8.5	2.6	2.1
Valcuende and Parra (2009)	16	100	5.75	5.0	66.0	4.3	32.9	32.0	7.7	7.4

Note: * Standard cube strength

*** With lateral reinforcement

** Based on the Eurocodes

**** Multiplied with k due to values of l_b / d_b

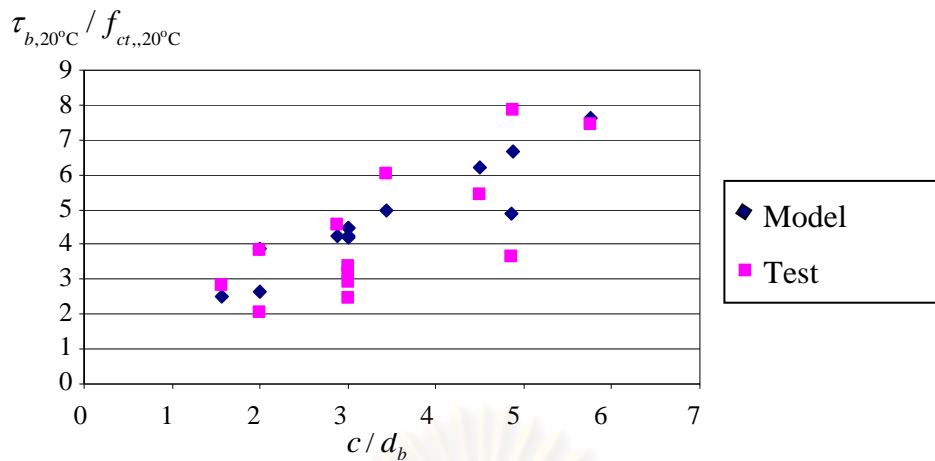


Figure 3.1 Comparison of the predicted bond strengths with previous experimental results for reinforced concrete at normal temperature

3.3 Radial Pressure due to Differential Thermal Expansion of Materials

The radial pressure due to the thermal expansion of concrete and the embedded reinforcing bar within the pull-out specimens, $p_{t,T}$, can not be directly measured during the test. However, under elevated temperatures, this radial pressure can be evaluated based on a critical temperature, ΔT_{cr} , at which the thermal radial pressure exceeds the pressure resistance of the concrete cover by using the computational procedure in Figure 2.9. The critical temperature increment ΔT_{cr} can be assessed by specifying a trial temperature increment, ΔT , and the mechanical properties of the rebar and the surrounding concrete as initial parameters. The process is iterated until the thermal radial pressure exceeding the pressure resistance of the concrete cover is computed. At this stage, cracking is initiated and propagates through the concrete cover, resulting in a failure of bonding between the concrete and the embedded bar, the so-called splitting failure, as shown in Figure 3.2.

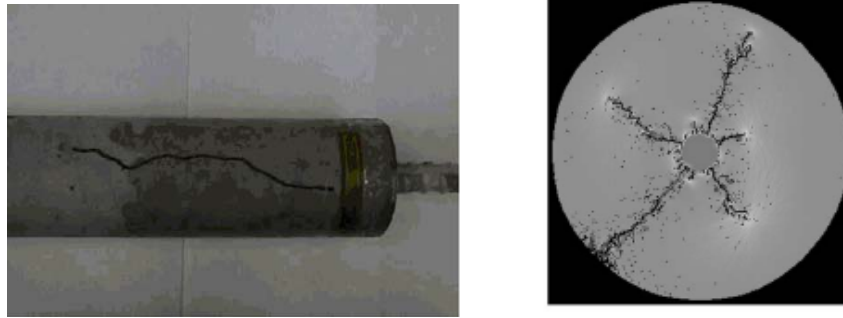


Figure 3.2 Splitting failure of the concrete cover (Aiello 2001; Wong *et al.*2006)

The critical temperature increment ΔT_{cr} values computed by the proposed model are compared with the results obtained from the previous experiments (Aiello 1999; Aiello *et al.* 2001; Masmoudi *et al.* 2005; Zaidi and Masmoudi 2008), the analytical model of Aiello *et al.* (2001) (without the tensile softening effect) and the mesoscopic thermoelastic damage (MTED) model of Wong *et al.* (2006) as summarized in Table 3.2. Note that the previous experimental investigations were conducted for cylindrical and rectangular concrete specimens reinforced with AFRP and GFRP bars which were slowly heated until the splitting failure of concrete occurred. For the rectangular FRP reinforced concrete specimens, the value of c is taken as a shorter distance between one-half of the reinforcement spacing and the minimum concrete cover.

The values of ΔT_{cr} shown in Table 3.2 are also plotted for different values of c/d_b in Figure 3.3. It is seen from Figure 3.3 that the proposed model can predict the critical temperature increments values close to the results obtained by the previous experiments and Aiello *et al.*'s model but generally higher than those predicted by the Aiello *et al.*'s model due to the tensile softening effect.

The inner crack radius r_i values estimated by the proposed method for FRP reinforced concrete prior to the splitting failure are also compared with the results obtained by the MTED model. Note that because it is difficult, if not virtually impossible, to measure the internal crack radii within concrete specimens, currently there are no experimental data available. The cracking patterns of the concrete cover for a cylindrical FRP reinforced concrete specimen with $c/d_b = 4.38$ predicted by the MTED model are compared with the crack radii computed by the proposed model as

illustrated in Figure 3.4. It is apparent from the illustration that the computed crack radii closely approximate the MTED modeling results for the temperature increments ranging between 34°C-74°C. However, the proposed model overestimates the critical temperature increment ΔT_{cr} at 85°C, compared with 76°C as predicted by the MTED model.

Through comparison with previous solutions and experimental results, it is seen that most of the results obtained from the proposed model agree better with the experimental data for the range of the c/d_b values considered compared with the model without the tensile softening effect. Furthermore, the estimated crack radii at different temperature increments conform with the cracking patterns predicted by the MTED model. It can be implied from the current study that the present model that incorporates the tensile softening effect can better characterize the actual behavior of the partially cracked concrete in evaluating the cracking resistance of FRP reinforced concrete under thermal loads.

Table 3.2 Comparison of the ΔT_{cr} values computed by the proposed method with the results obtained from the previous studies

Specimen Geometry	Rebar Material Properties	Concrete Material Properties	c/d_b	d_b (mm)	Critical temperature increment ($^{\circ}\text{C}$)				References for Experimental Results
					Experimental results	Aiello <i>et al.</i> 's model (2001)	MTED model (Wong <i>et al.</i> 2006)	Proposed model	
Rectangular	AFRP type $E_b=3,200$ MPa $\nu_b=0.38^*$ $\alpha_b=60.0 \times 10^{-6} / ^{\circ}\text{C}$	$E_c=24,300$ MPa $f_{tc}=2.36$ MPa $\nu_c=0.18^*$ $\alpha_c=10.0 \times 10^{-6} / ^{\circ}\text{C}$	1.19	10	40	14	-	22	Aiello (1999)
			1.25	10	42	14	-	23	
			1.67	10	43	18	-	28	
			2.27	10	43	24	-	37	
			1.00	10	35	17	-	27	
			2.00	10	50	30	-	48	
	GFRP type $E_b=7,100$ MPa $\nu_b=0.34$ $\alpha_b=41.2 \times 10^{-6} / ^{\circ}\text{C}^{**}$	$E_c=28,000$ MPa $f_{tc}=4.20$ MPa $\nu_c=0.17$ $\alpha_c=11.6 \times 10^{-6} / ^{\circ}\text{C}$	1.00	25	30	22	-	29	Zaidi and Masmoudi (2008)
			1.30	25	40	27	-	35	
			1.40	19	40	29	-	37	
			1.60	16	>60	32	-	41	
			1.80	19,25	>60	36	-	45	
			2.20	16,19,25	>60	44	-	54	
	GFRP type $E_b=4000$ MPa $\nu_b=0.40$ $\alpha_b=58.0 \times 10^{-6} / ^{\circ}\text{C}$	$E_c=30,000$ MPa $f_{tc}=3.90$ MPa $\nu_c=0.18$ $\alpha_c=12.1 \times 10^{-6} / ^{\circ}\text{C}$	1.00	13	-	17	36,42,46***	25	Wong (2006)
			1.27	13	-	21	28***	30	
			2.00	13	-	30	54,52***	43	
1.46			13	41	23	-	33		
Cylindrical	GFRP type $E_b=4000$ MPa $\nu_b=0.40$ $\alpha_b=58.0 \times 10^{-6} / ^{\circ}\text{C}$	$E_c=30,000$ MPa $f_{tc}=3.90$ MPa $\nu_c=0.18$ $\alpha_c=12.1 \times 10^{-6} / ^{\circ}\text{C}$	1.46	13	28	23	35	33	Aiello <i>et al.</i> (2001) and Wong <i>et al.</i> (2006)
			2.92	13	70	43	55	60	
			4.38	13	65	65	76	85	
	GFRP type $E_b=7100$ MPa $\nu_b=0.38$ $\alpha_b=31.0 \times 10^{-6} / ^{\circ}\text{C}^{**}$ for $d=13$ mm $\alpha_b=34.9 \times 10^{-6} / ^{\circ}\text{C}^{**}$ for $d=16$ mm $\alpha_b=36.6 \times 10^{-6} / ^{\circ}\text{C}^{**}$ for $d=19$ mm $\alpha_b=43.1 \times 10^{-6} / ^{\circ}\text{C}^{**}$ for $d=25$ mm	$E_c=28,000$ MPa $f_{tc}=4.10$ MPa $\nu_c=0.17$ $\alpha_c=11.6 \times 10^{-6} / ^{\circ}\text{C}$	0.80	25	30	16	-	23	Masmoudi <i>et al.</i> (2005)
			1.00	25	30	19	-	26	
			1.20	19	30	28	-	36	
			1.50	13,16, 19,25	34.5****	35****	-	44****	

Note: * General properties

** Temperature range: 30 $^{\circ}\text{C}$ to 60 $^{\circ}\text{C}$ *** The different values of ΔT_{cr} reported for the MTED model are due to the varying configurations of the model

**** Average values

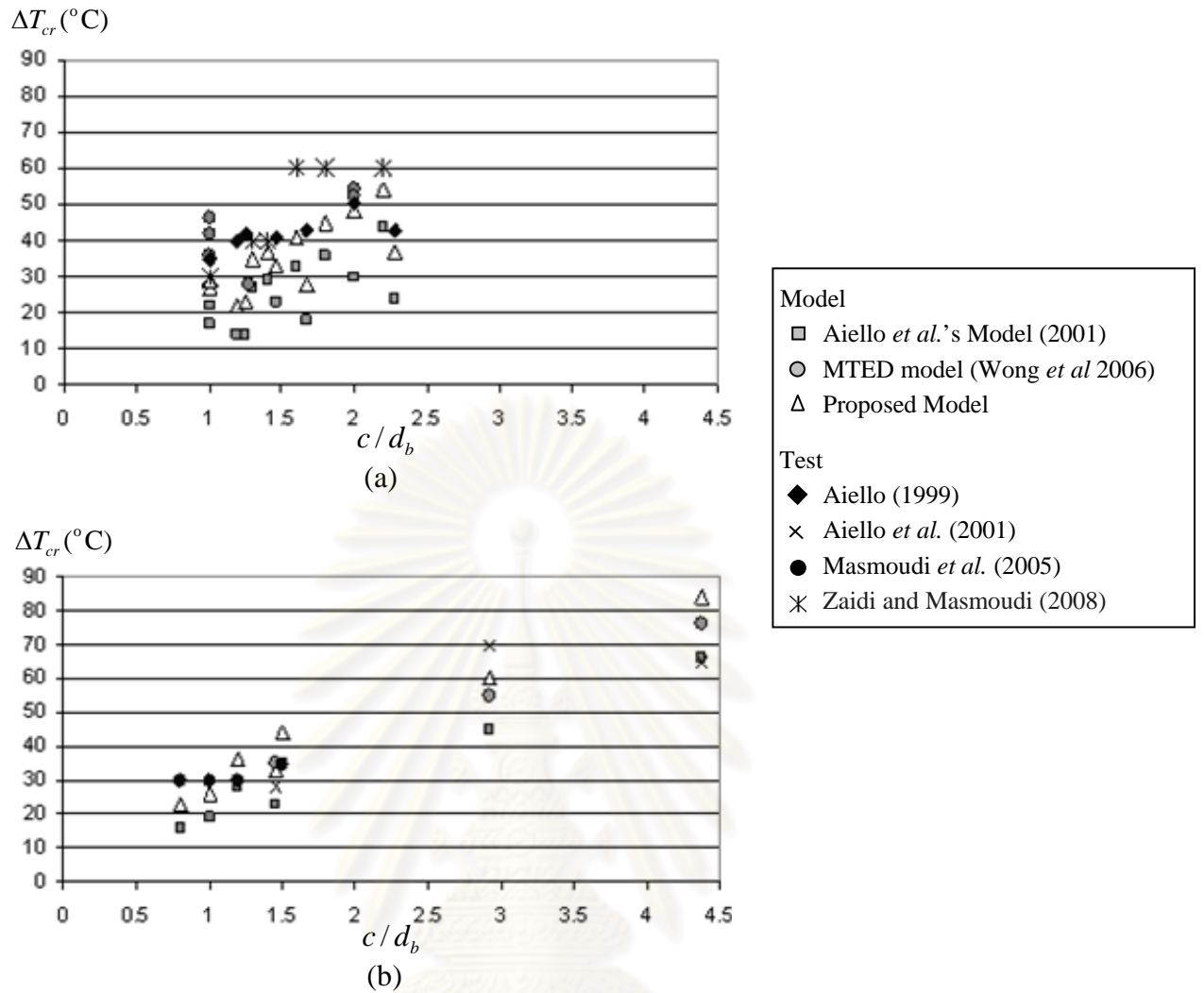


Figure 3.3 Variation of ΔT_{cr} with respect to different c/d_b values for FRP reinforced concrete: (a) rectangular specimens and (b) cylindrical specimens

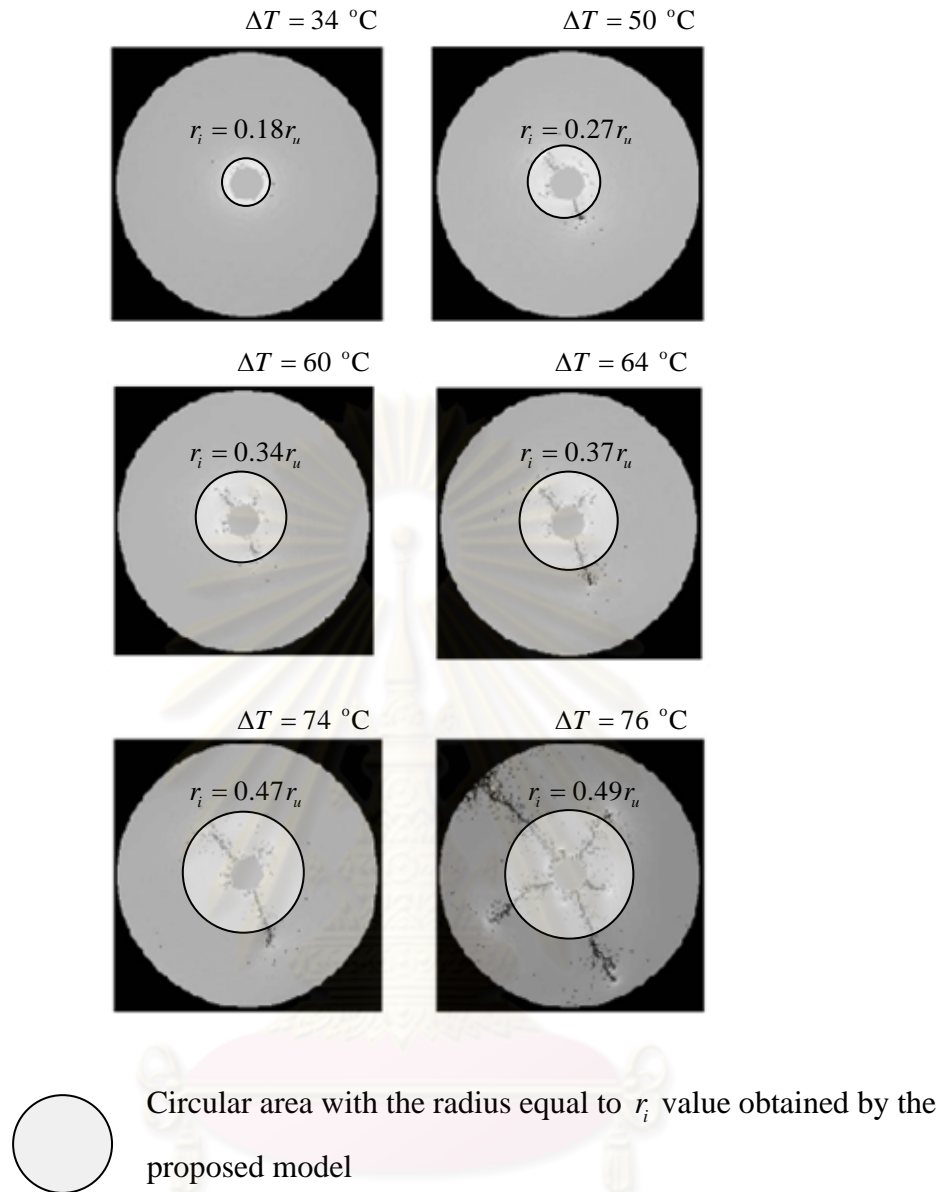


Figure 3.4 Comparison between the cracking patterns of the cylindrical FRP reinforced concrete specimens with $c/d_b = 4.38$ as predicted by the MTED model and the crack radius r_i values obtained by the proposed model

3.4 Prediction of Bond Strength for Reinforced Concrete at Elevated Temperatures

For the current study the efficacy of the proposed model to predict the bond strength for reinforced concrete at elevated temperatures is examined using previous experimental results based on pull-out specimens, each of which consisted of a concrete cylinder or a concrete square prism and an embedded reinforcing steel bar with or without stirrups (Diederichs and Scheider 1981; Hertz 1982; Morley and Royles 1983; and Haddad *et al.* 2008). The details of the pull-out specimens are summarized in Table 3.3. The analysis performed for the proposed model assumes a uniform temperature distribution throughout the cross section of the concrete cylinder and the reinforcement bar since in the experiments the specimens were reported to be slowly heated, at the rate of $2^{\circ}\text{C}/\text{minute}$ or less, up to the required temperature and saturated thermally for at least one hour.

The values of bond strength and the ratio of the bond strength at the elevated temperature T to the bond strength at normal temperature, $\tau_{b,T}/\tau_{b,20^{\circ}\text{C}}$, as reported by the previous studies are compared with the values predicted by the proposed model with and without the thermal effect as shown in Figure 3.5 to Figure 3.9. It is seen from these figures that the predicted values are in line with the experimental results, both for the cases of reinforced concrete specimens under and after elevated temperatures. Moreover, it can be observed from the results of the proposed model that the thermal effect degrades the bond strength, especially for small c/d_b values ($c/d_b \leq 2.00$) and for medium temperatures ($T \approx 200^{\circ}\text{C} - 300^{\circ}\text{C}$). In other words, with larger c/d values, the concrete cover is able to act better as a thermal barrier and causes smaller thermal crack radii compared with the original concrete cover. For the case of high temperatures ($T > 300^{\circ}\text{C}$), the modulus of elasticity of both concrete and reinforcing steel drop significantly; resulting in less thermal effect and smaller crack radii.

Note that the predicted values may be overestimated or underestimated due to the variation of the properties of concrete and reinforcing steel with temperature, which can vary in a wide range (Xiao, Konig 2004; Chang *et al.* 2006; Youssef and Mofteh 2007). Nonetheless, based on the results of the current study it may be concluded that the

accuracy of the proposed model based on the mechanical properties according to the Eurocodes is acceptable for the prediction of the bond strength of steel reinforced concrete elements under elevated temperatures.

Table 3.3 Details of the pull-out specimens in previous experiments

Tested by	Specimen type	Aggregate Type	d_b (mm)	r_u (mm)	c/d_b	l_b/d_b	$f_{c,20\text{ }^\circ\text{C}}$ (MPa)
Diederichs and Scheider (1981)	Pull-out cylindrical specimens without stirrups under elevated temperatures	Siliceous	16	86	4.88	5.0	55*
Hertz (1982)	Pull-out cylindrical specimens without stirrups after elevated temperatures	Mixture of quartz, granite and limestone	25	75	2.50	N.A.	20
			16	75	4.18	N.A.	20
			12	75	5.75	N.A.	20
Morley and Royles (1983)	Pull-out cylindrical specimens without stirrups after elevated temperatures (with 3.77 MPa pre-stress)	Siliceous	16	33	1.56	2.0	35*
			16	40	2.00	2.0	35*
			16	54	2.88	2.0	35*
			16	63	3.44	2.0	35*
		Pull-out cylindrical specimens without stirrups under elevated temperatures (with 3.77 MPa pre-stress)	Siliceous	16	63	3.44	2.0
Haddad <i>et al.</i> (2008)	Pull-out square prism specimens with stirrups after elevated temperatures	Basalt	20	50	2.00	7.5**	77*

Note: * Standard cube strength

** For large l_b/d_b values, the experimental bond strength must be converted to the local bond strength (Yasojima and Kanakubo 2005).

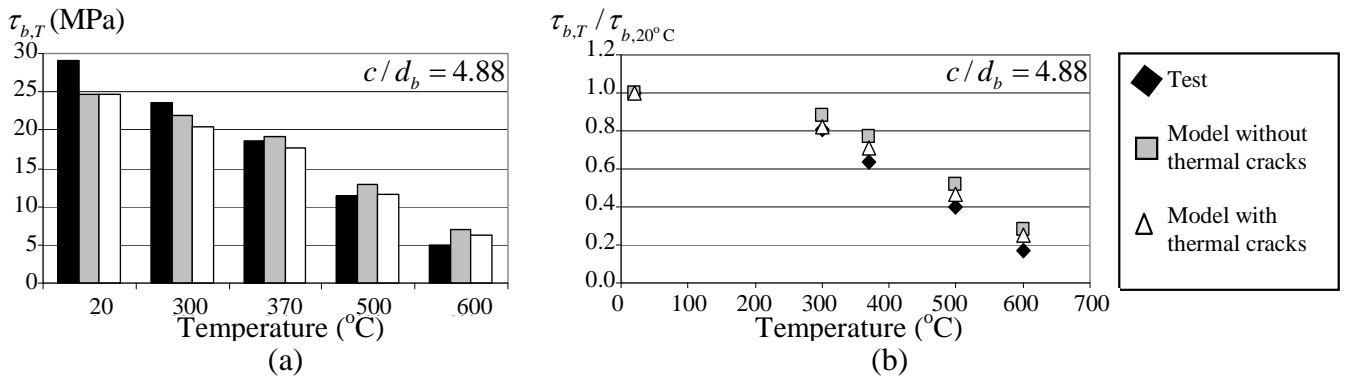


Figure 3.5 Comparison of the predicted bond strengths with the test results of Diederichs and Scheider (1981): (a) $\tau_{b,T}$ vs. Temperature and (b) $\tau_{b,T}/\tau_{b,20^{\circ}\text{C}}$ vs. Temperature

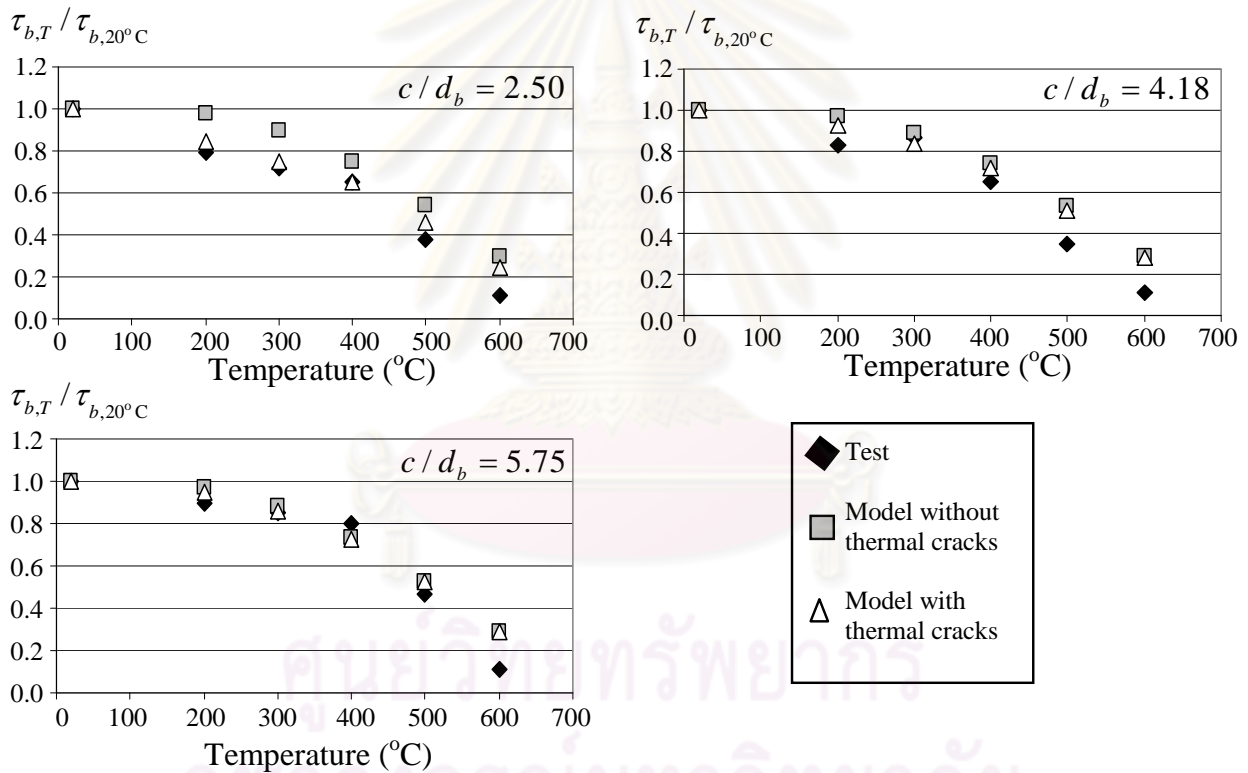


Figure 3.6 Comparison of the predicted bond strengths with the test results of Hertz (1982): $\tau_{b,T}/\tau_{b,20^{\circ}\text{C}}$ vs. Temperature

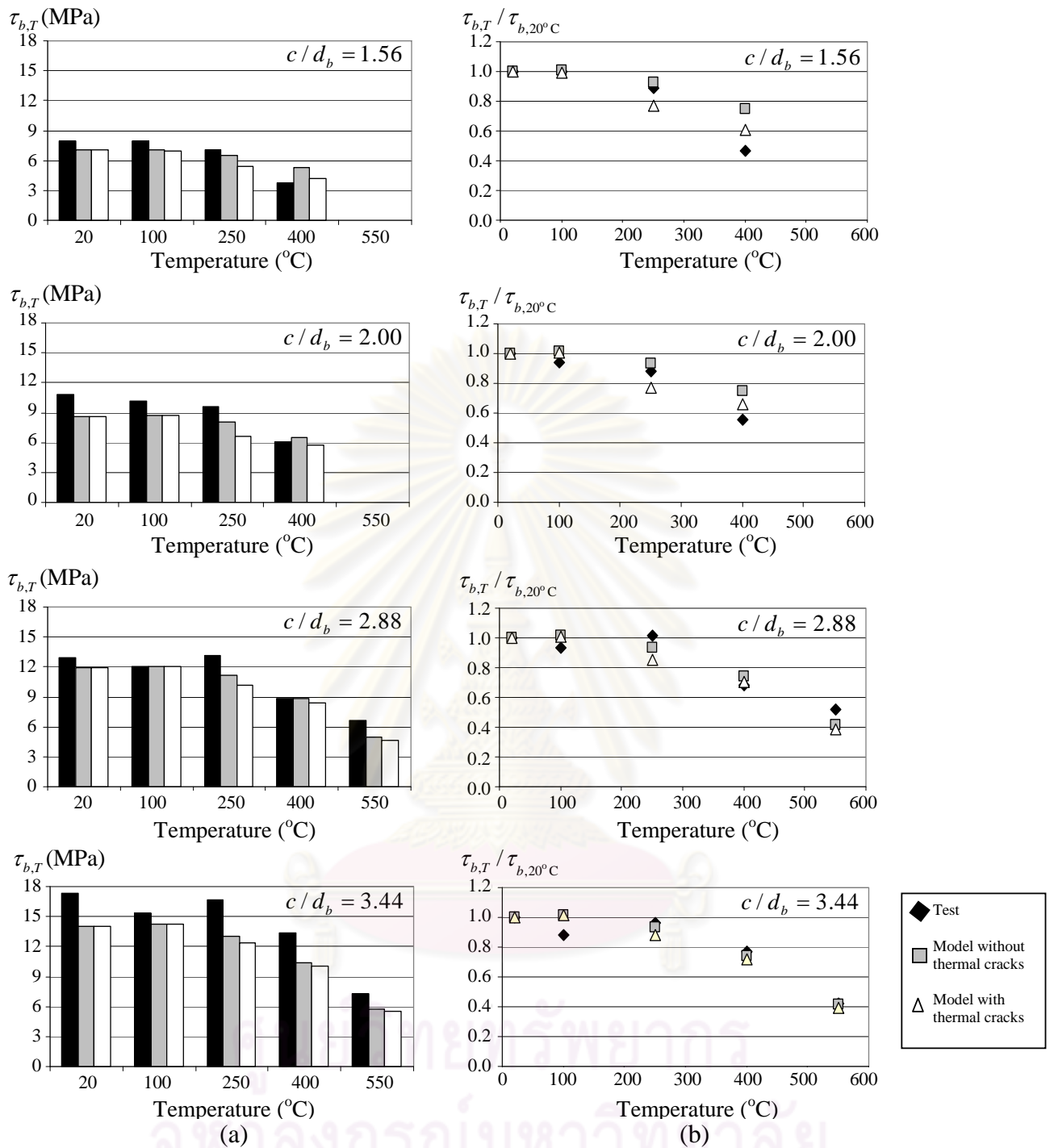


Figure 3.7 Comparison of the predicted bond strengths with the test results of Morley and Royles (1983) after elevated temperatures: (a) $\tau_{b,T}$ vs. Temperature and (b) $\tau_{b,T} / \tau_{b,20^{\circ}\text{C}}$ vs. Temperature

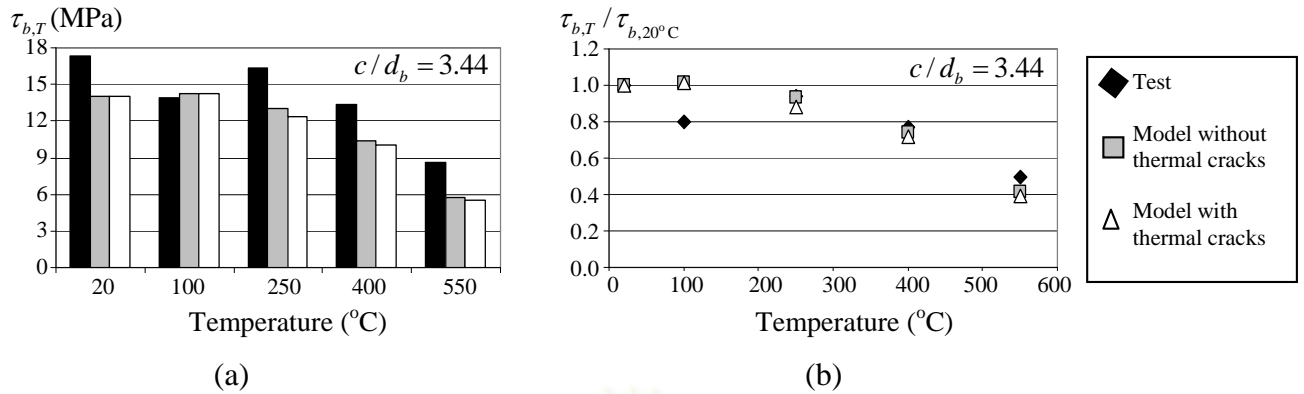


Figure 3.8 Comparison of the predicted bond strengths with the test results of Morley and Royles (1983) under elevated temperatures: (a) $\tau_{b,T}$ vs. Temperature and (b) $\tau_{b,T}/\tau_{b,20^{\circ}\text{C}}$ vs. Temperature

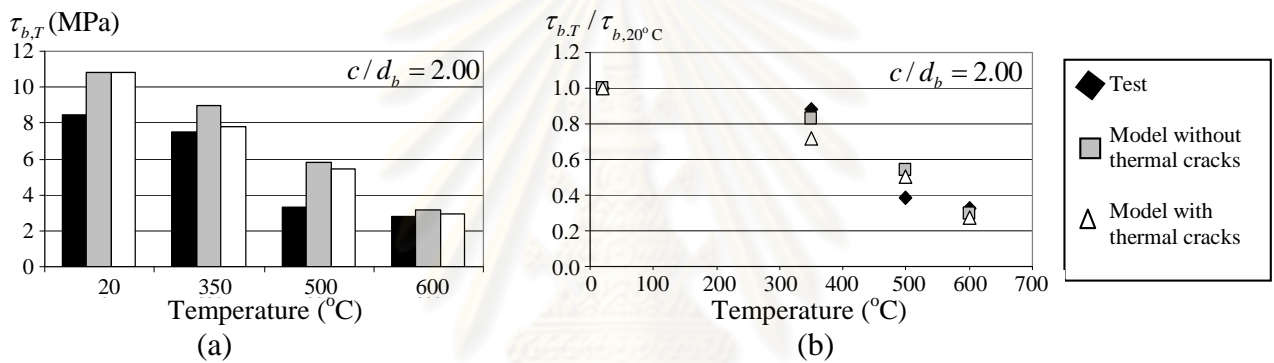


Figure 3.9 Comparison of the predicted bond strengths with the test results of Haddad *et al.* (2008): (a) $\tau_{b,T}$ vs. Temperature and (b) $\tau_{b,T}/\tau_{b,20^{\circ}\text{C}}$ vs. Temperature

3.5 Bond-Slip Relationship

Many researchers have established the bond stress-slip relationship for reinforced concrete at normal temperature based on the experiment works (Eligehausen *et al.* 1983; Pochanart and Harmon 1989; CEB-90 (1991); Alsiwat and Saatcioglu 1992). However, only a few researchers (Den Uijl and Bigaj 1996; Takahiro *et al.* 1999) have investigated the correlation between the slip and the inner crack radius, which can be used to establish the bond-slip relationship for reinforced concrete at elevated temperatures. The bond-slip relationship is required to investigate the bonding effect on the behavior of reinforced concrete structures.

Based on the proposed model, the bond stress for the normal-temperature condition ($T = 20^\circ\text{C}$) can be analyzed at two stages: the elastic stage and the partially cracked elastic stage. For the partially cracked elastic stage, the relationship between the normalized bond stress, $\tau_{20^\circ\text{C}} / \tau_{b,20^\circ\text{C}}$, and the inner crack length, $r_i - r_b$, in general can be illustrated as shown in Figure 3.10 (a) in which the bond stress at the initiation of the inner crack ($r_i - r_b = 0$) is denoted as $\tau_{p,20^\circ\text{C}}$. To compare the bond-slip relationship obtained from the proposed model and the previous test results, a generalized curve which relates the normalized bond stress after the initiation of the inner crack ($\tau_{p,20^\circ\text{C}} / \tau_{b,20^\circ\text{C}}$) and the relative slip, $s - s_p$, must be established as shown in Figure 3.10 (b) in which s_p is the slip corresponding to $\tau_{p,20^\circ\text{C}}$. Based on the previous studies (Diederichs and Scheider 1981; Lee *et al.* 2002; Al-Negheimish and Al-Zaid 2004; Haddad *et al.* 2008), the relationship between the curve in Figure 3.10 (a) and Figure 3.10 (b) can be approximated as:

$$s - s_p = \frac{r_i - r_b}{k} \quad (3.1)$$

in which k is an empirical constant.

In order to generate a complete curve that also covers the elastic stage, the curve in Figure 3.10 (a) must be extrapolated to start from zero bond stress ($\tau_{20^\circ\text{C}} / \tau_{b,20^\circ\text{C}} = 0$). By using the initial slope of $\tau_{20^\circ\text{C}} / \tau_{b,20^\circ\text{C}}$ vs. $r_i - r_b$, the curve can be extended to intercept the horizontal axis at r_i' as shown in Figure 3.10 (c) in which r_i' can be computed as:

$$r_i' = \frac{\tau_{p,20^\circ\text{C}}}{\left. \frac{d\tau_{p,20^\circ\text{C}}}{dr_i} \right|_{r_i=r_b}} = \frac{r_b}{2} \left(1 + \left(\frac{r_b}{r_u} \right)^2 \right) \quad (3.2)$$

After shifting the origin of the curve as shown in Figure 3.10 (d), the relationship between the slip s and the inner crack radius r_i can be determined as

$$s = \frac{r_i - r_b + r_i'}{k} \quad (3.3)$$

Note that r_i' may be considered as the virtual crack radius for the elastic stage.

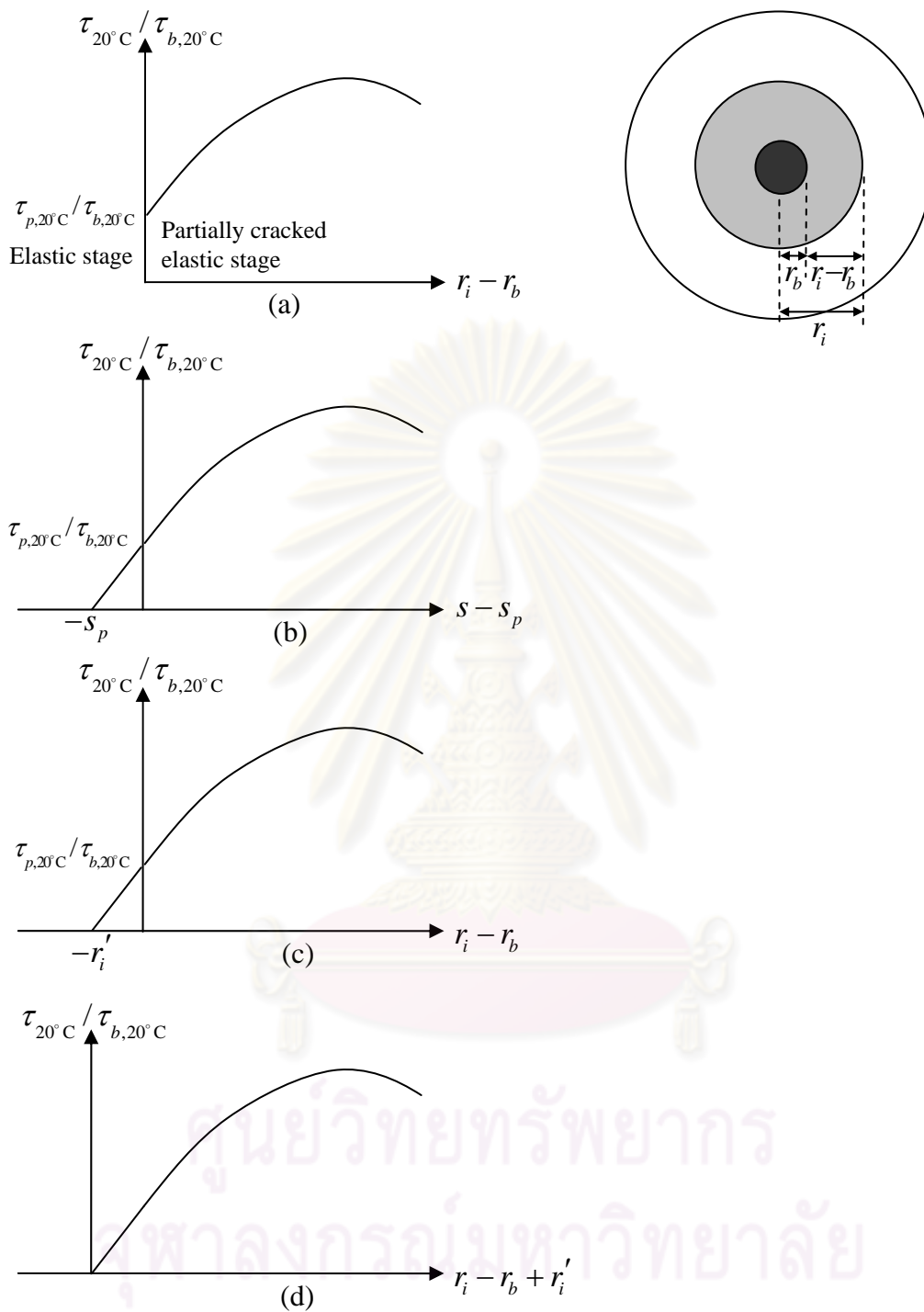


Figure 3.10 Analysis of bond stress-slip-inner crack radius relationship:

- (a) bond stress-inner crack length relationship in the partially cracked elastic stage;
- (b) bond stress-slip relationship in the partially cracked elastic stage; (c) virtual crack radius obtained from extrapolation; (d) curve shifting

As for the normal-temperature case, the slip can be related with the inner crack radius at the elevated temperature T . The total crack radius r_i can be considered to be due to the thermal effect ($r_{i,T}$) and the pull-out load. As such, the inner crack length due to the pull-out load at the elevated temperature can be considered as $r_i - r_{i,T}$. The bond stress at the initiation of the inner crack due to the pull-out load ($r_i - r_{i,T} = 0$) is denoted as $\tau_{p,T}$. By substituting the inner crack length, $r_i - r_b$, in Eq. (3.3) with $r_i - r_{i,T}$, we obtain:

$$s = \frac{r_i - r_{i,T} + r_i'}{k} \quad (3.4)$$

where the virtual crack radius r_i' for reinforced concrete at the elevated temperature T can be computed based on Eq. (3.2) and Eq. (2.20) as

$$r_i' = \frac{\tau_{p,T}}{\left(\frac{r_{i,T}}{r_b} \right) \frac{d\tau_{p,T}}{dr_i} \Big|_{r_i=r_{i,T}}} \quad (3.5)$$

Based on a statistical analysis of the correlation between the experimental slips (Diederichs and Scheider 1981; Lee *et al.* 2002; Al-Negheimish and Al-Zaid 2004; Haddad *et al.* 2008) and the slips obtained from the proposed method for different values of normalized bond stress, $\tau_{20^\circ\text{C}} / \tau_{b,20^\circ\text{C}}$, it has been found that the estimate of $k = 70$ provides the best coefficient of determination $R^2 = 0.8625$ as shown in Figure 3.11. Note that in the proposed model the splitting failure occurs when then ultimate slip is reached at which point the bond stress can be considered to be zero.

The bond-slip relationships obtained by using the proposed model are compared with the previous experimental results (Diederichs and Scheider 1981; Lee *et al.* 2002; Al-Negheimish and Al-Zaid 2004; Haddad *et al.* 2008) in terms of the normalized bond stress, $\tau_{20^\circ\text{C}} / \tau_{b,20^\circ\text{C}}$, as shown in Figure. 3.12. The comparisons between the bond-slip relationship obtained from the proposed model and the previous test results of Diederichs and Scheider (1981) and Haddad *et al.* (2008) are shown in Figure 3.13 to Figure 3.15, respectively.

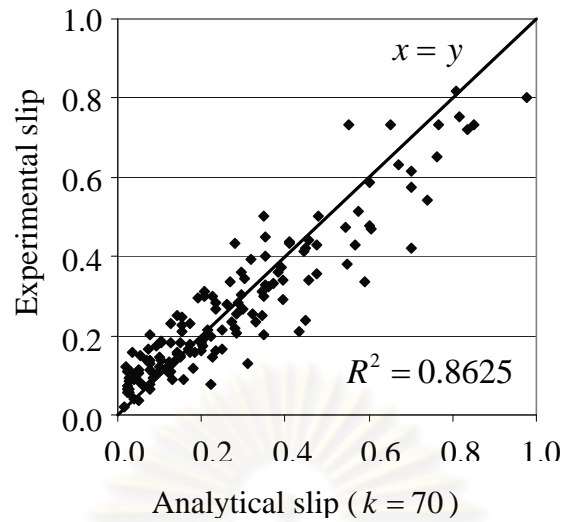


Figure 3.11 Comparison between the experimental slip and the analytical slip ($k = 70$)

In some cases of the comparison, the experimental slips may be significantly larger than the modeling results due to the combination of modes of failure between the splitting failure and the shearing-off failure, especially for large values of c/d_b . In these cases, the maximum bond stress can be higher than the splitting bond strength but the bond-slip relationship remains the same in the early stage (Eligehausen *et al.* 1983; Harajli *et al.* 1995; Den Uijl and Bigaj 1996). Therefore, the experimental bond stresses are normalized by the bond stress value taken at the slip which corresponds to the maximum bond stress as predicted by the proposed model. At the elevated temperatures, it can be seen in most cases that the modeling results agree well with the experimental results except for the case of $T = 600^\circ\text{C}$ in Figure 3.13 in which significantly lower stiffness of the experimental bond-slip relationship is observed. The reason may be due to the deviation of the modulus of elasticity of concrete used in the model from the actual unreported value.

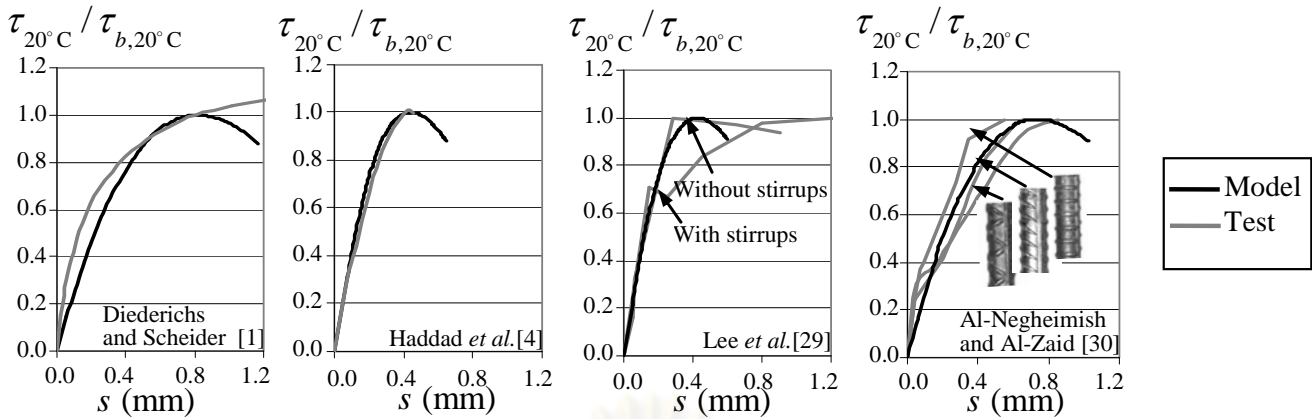


Figure 3.12 Comparison between the bond-slip relationships obtained by the proposed method and the test results

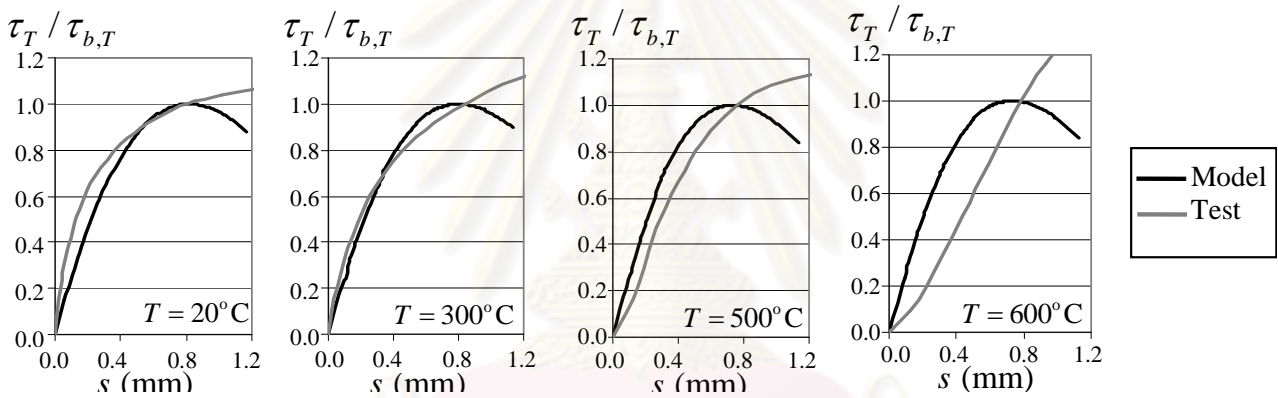


Figure 3.13 Comparison between the bond-slip relationship obtained by the proposed method and the test results of Diederichs and Scheider (1981)

ศูนย์วิทยทรัพยากร
จุฬาลงกรณ์มหาวิทยาลัย

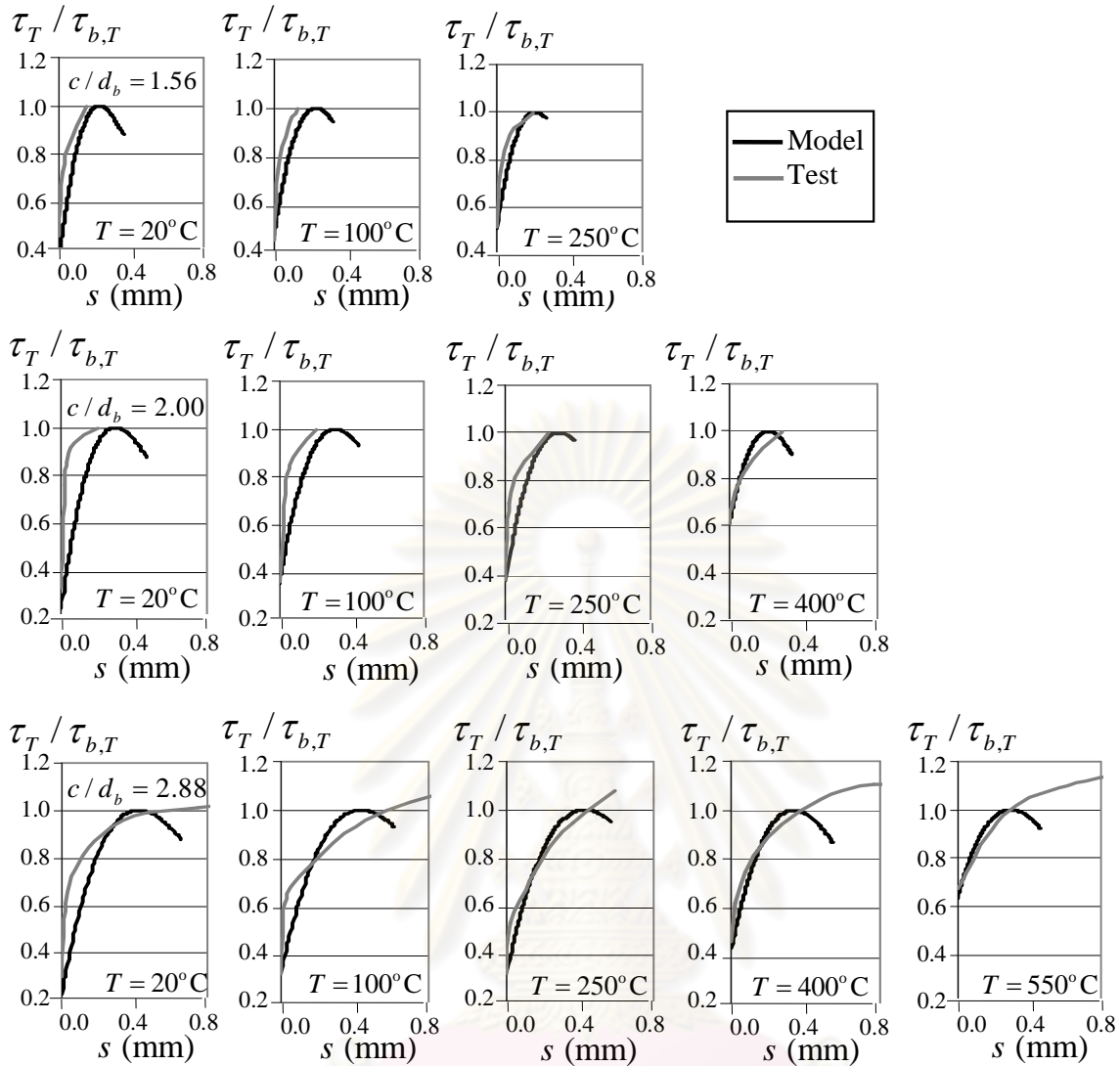


Figure 3.14 Comparison between the bond-slip relationships obtained by the proposed method and the test results of Morley and Royles (1983)

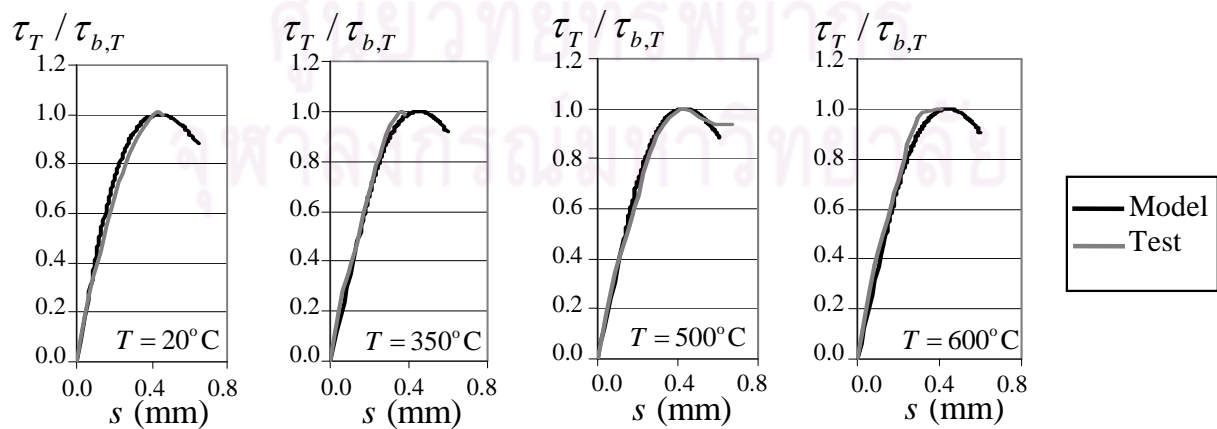


Figure 3.15 Comparison between the bond-slip relationships obtained by the proposed method and the test results of Haddad *et al.* (2008)

CHAPTER IV

APPLICATION OF THE MODEL FOR REINFORCED CONCRETE BEAMS AT ELEVATED TEMPERATURES

4.1 Introduction

For flexural load-bearing structural members, such as reinforced concrete beams, the degradation of the bond strength between concrete and the embedded steel rebars at elevated temperatures can affect the structural behavior of the members. Most of the previous studies (Huang and Platten; 1997; Terro 1998; Zha 2003; Capua and Mari 2007; Bratina *et al.* 2007; Kodur, Dwaikat 2008; Huang *et al.* 2009) have neglected the bonding effect on the structural behavior of beams under high-temperature conditions and applied perfect bond assumption for their analyses. For the current study we investigate the influences of bonding on the structural behavior of reinforced concrete beams subjected to elevated temperatures through a series of load-bearing tests.

The test data of the reinforced concrete beams in terms of the load-deflection relationship and the crack pattern were compared with the results obtained from the finite-element analyses assuming two types of bonding: perfect bonding and slip bonding (based on the model proposed in the previous chapter). The comparison of the structural behavior obtained from the finite-element models and the experimental results allowed us to examine the influence of bonding at the steel-concrete interface on the structural behavior of the reinforced concrete beams. The results are useful as a guideline for the structural design for fire safety.

4.2 Experimental Setup

4.2.1 Test Specimens

A series of load-bearing fire tests were conducted using eight reinforced concrete beam specimens. The dimensions of the beams were 200 mm x 300 mm in cross-section, 2450 mm in overall length, and 2300 mm in supported span. These beams were cast from a concrete mix having the compressive strength of 24 MPa after 28 days of casting based on standard cylinders. Each of the beam specimens was reinforced by two 16 mm-diameter deformed bars of SD 40 grade with the tested yield stress of 475 MPa as the tension reinforcement, two 9 mm-diameter round bars of SR 24 grade with the tested yield stress of 350 MPa as the compression reinforcement and 6 mm-diameter round bars of grade SR 24 with the tested yield stress of 320 MPa as stirrups at a spacing of 150 mm throughout the beam's length. The modulus of elasticity of the steel rebars obtained from the test was approximately 200,000 MPa. The details of a typical beam specimen are shown in Figure 4.1.

To monitor the temperature distribution of the specimens during the fire test, type K 4/0.32 GBS thermocouples with the sensitivity of $41 \mu\text{V}/^\circ\text{C}$ and the measurement range between -200°C and $+1350^\circ\text{C}$ were used. The thermocouples were installed at various locations within each specimen prior to pouring the concrete mix into the formwork used for casting the specimen as also illustrated in Figure 4.1. All the specimens were cast at room temperature and cured by covering them with wet hessian. The curing duration was set to be at least 28 days before the test. The upper surface of each of the beam specimens for load-bearing tests under elevated temperatures was protected with 2.5-cm thick ceramic fiber pads to simulate fire exposure only on three sides.

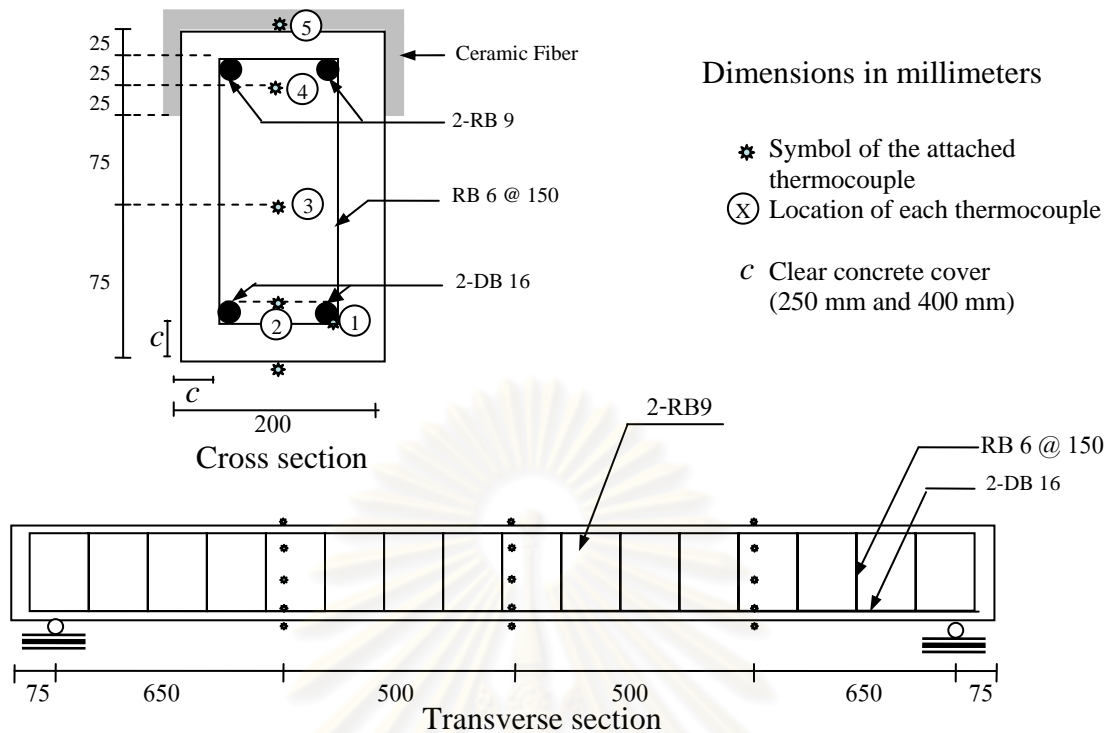


Figure 4.1 Details of a typical beam specimen

4.2.2 Test Program

The fire tests were conducted at the Fire Safety Research Center (FSRC) of Chulalongkorn University. The specimen installation within the furnace and the load-bearing test setup are illustrated in Figure 4.2. For the load-bearing test, the specimens were subjected to two-point bending in which the load was applied using a hydraulic jack and a transfer girder with two short columns to transmit the load to the beam. The total weight of the loading system was 2 kN. The vertical movements were observed through ceramic fiber tubes and the loading columns inserted into the furnace above the beam specimens. To monitor the movements, linear variable differential transducers (LVDT) with an accuracy of 0.1 mm were used. Throughout the test program the movements of the supports were continuously monitored (see Figure 4.2) to avoid the collapse of the supports while the movements of the loading columns were used to examine the inclination of the loading system. The vertical movements of the specimen measured elsewhere were used to plot the load-deflection curve.

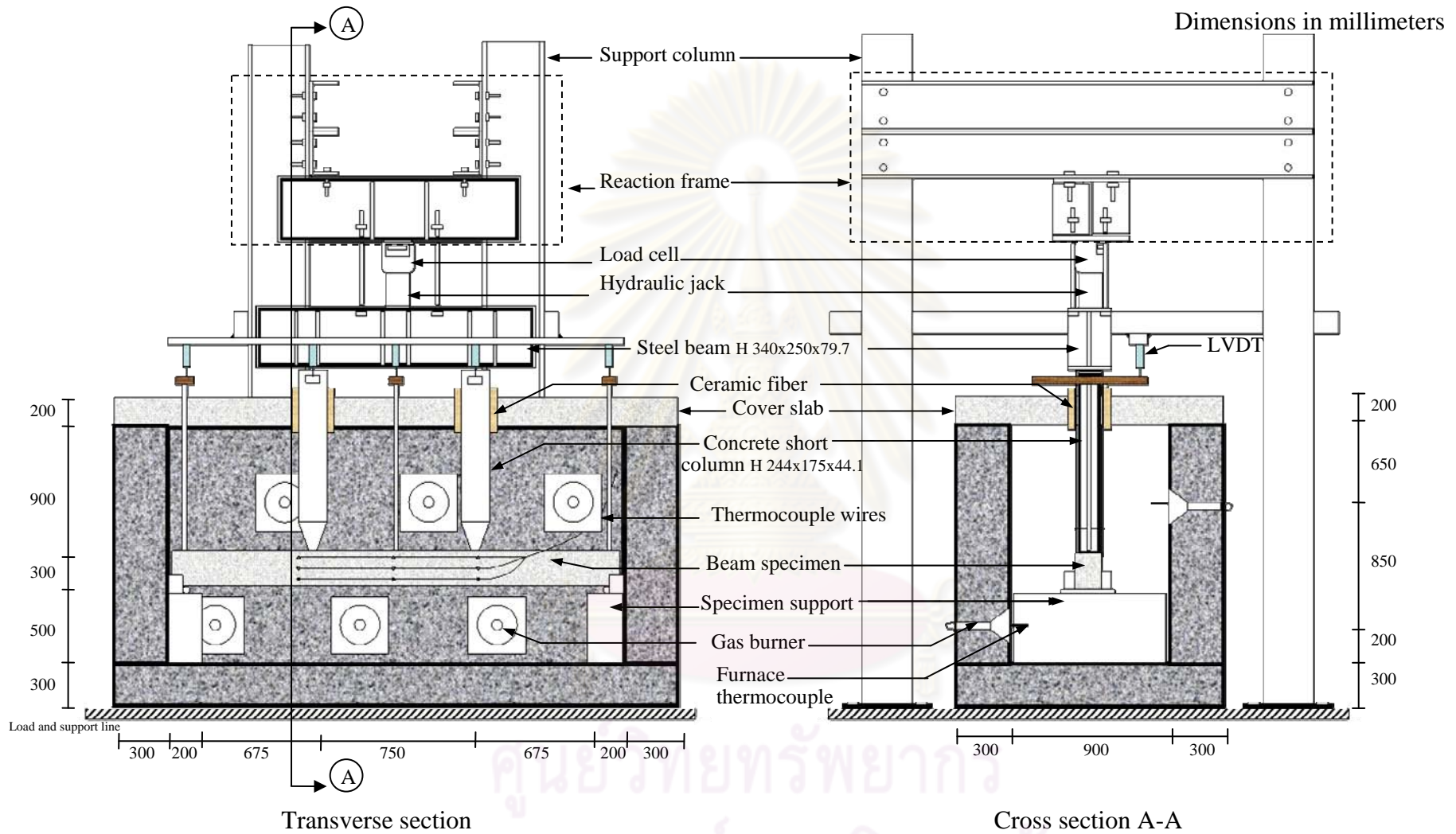


Figure 4.2 Experimental setup for the flexural test of reinforced concrete beams at elevated temperatures

The details of the furnace used in the current study are shown in Figure 4.2 and 4.3. The internal dimensions of the furnace are 0.90 m wide, 2.50 m long and 1.70 m high. The inside surface of the furnace is lined with 30 cm-thick insulating bricks and ceramic fiber blankets. Three gas-nozzled burners and three thermocouples are located on each of the two side walls of the furnace at the level of approximately 0.20 m above the furnace floor on one side and 1.05 m above the furnace floor on the other side. The lid of the furnace is a refractory-lined concrete cover slab with two 0.25 m x 0.25 m openings to insert the transfer columns for the flexural loading.

The temperatures and the heating periods during the fire tests are summarized in Table 4.1 and plotted in Figure 4.4. The furnace temperature of up to 550 °C was used to avoid concrete spalling or severe damage of the specimens that may cause premature bonding failure (Bazant and Kaplan 1996). Moreover, the heating period was set to two hours to allow heat to dissipate through the entire cross section of the beam. The furnace temperature was controlled to reach the target temperature within five minutes and constant thereafter until the flexural test was completed. The temperature inside the furnace was controlled based on the average of the temperatures recorded by the six thermocouples every two seconds. The valve of the gas supply for each burner was controlled or switched off to adjust the furnace temperature.

After the heating period of 2 hours, the load-bearing test of the beam was conducted. The applied load was increased in increments of 10 kN/minute. During the loading, the deflections of the beam were recorded every two seconds. The applied load was increased until the specimen reached the peak load capacity. After the test, the beam was cooled in the furnace for 24 hours and then observed for the crack patterns.

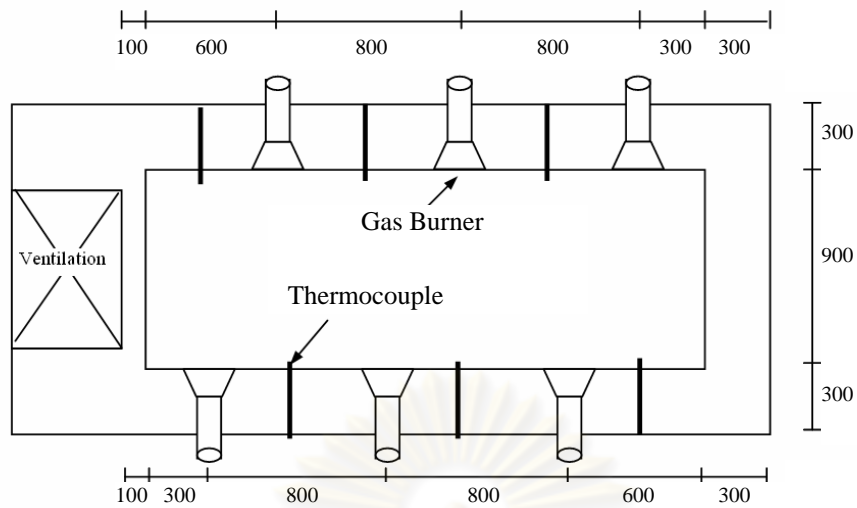


Figure 4.3 Top view of the furnace

Table 4.1 Temperatures and heating periods for fire tests

Specimen	Testing Temperature (°C)	Clear concrete cover (mm)	Heating period (minute)
C 25-RT	Room temperature	25	N.A.
C 40-RT	Room temperature	40	N.A.
C 25-250	250	25	125
C 40-250	250	40	125
C 25-400	400	25	125
C 40-400	400	40	125
C 25-550	550	25	125
C 40-550	550	40	125

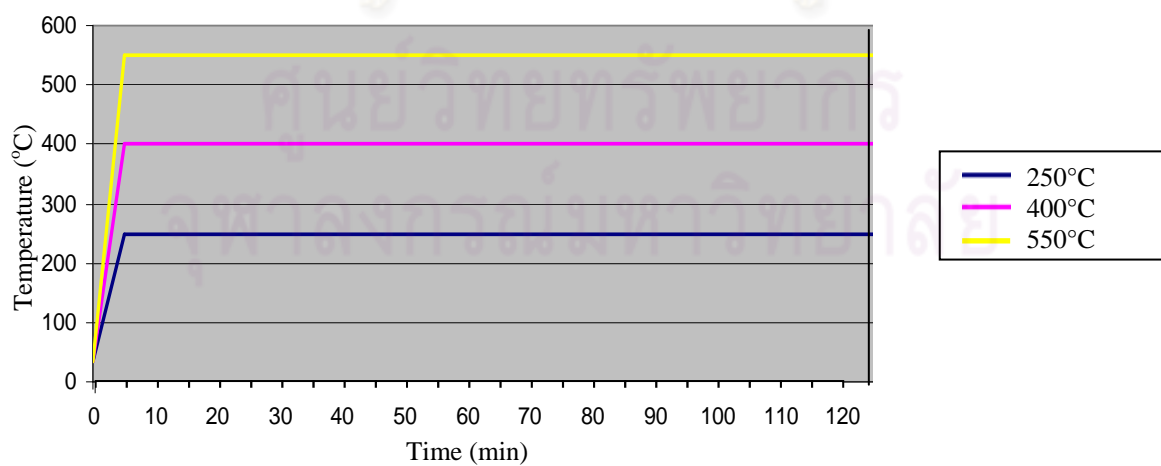


Figure 4.4 The specified temperature-time relationships for fire tests

4.2.3 Experimental Results

The temperature-time curves and the load-deflection curves are shown in Figures 4.5 – 4.7, respectively. It can be seen from Figure 4.5 and Figure 4.6 that the temperatures of the reinforcing steel for the beam specimens in C25 series are higher than those in C40 series. Based on the load-deflection curves in Figure 4.7, it can be observed that the peak loads of the beams in both series slightly decrease with the increasing level of temperature. The gradients of the load-deflection curves become more gradual under higher temperature levels which correspond to the softening stress-strain behavior of the reinforcing steel under elevated temperatures in accordance with BS EN 1992-1-2 (2004). It can also be observed from Figures 4.5 and 4.6 that the temperatures of the reinforcing steel are 480°C and 405°C, respectively, for specimens C25-550 and C40-550, upon which it is found that the peak load of specimen C25-550 is slightly less than that of specimen C40-550.

The crack patterns of the specimens can be illustrated in Figure 4.8, in which three types of cracks, i.e. flexural cracks, shear cracks; and tensile splitting cracks, are observed. For each of the beam specimens, the type of failure was identified based on the following guidelines (see Figure 4.9):

- the flexural failure was identified if crushing or compressive cracking occurred at the upper surface of the specimen;
- the shear failure was identified if shear cracks occurred and propagated to the lower or the upper surface of the specimen; and
- the shear failure with tensile splitting cracks was identified if shear cracks occurred and linked to tensile splitting cracks along the length of the reinforcing bars.

The types of failure of the specimens are summarized in Table 4.2. The evidence of shear cracks on the specimens under elevated temperatures clearly shows the thermal load effect upon the shear strength of the specimens. The tensile splitting cracks observed for the specimens in C25 series are due to insufficient concrete cover and can lead to the structural failure as can be seen in specimens C25-250 and C25-400.

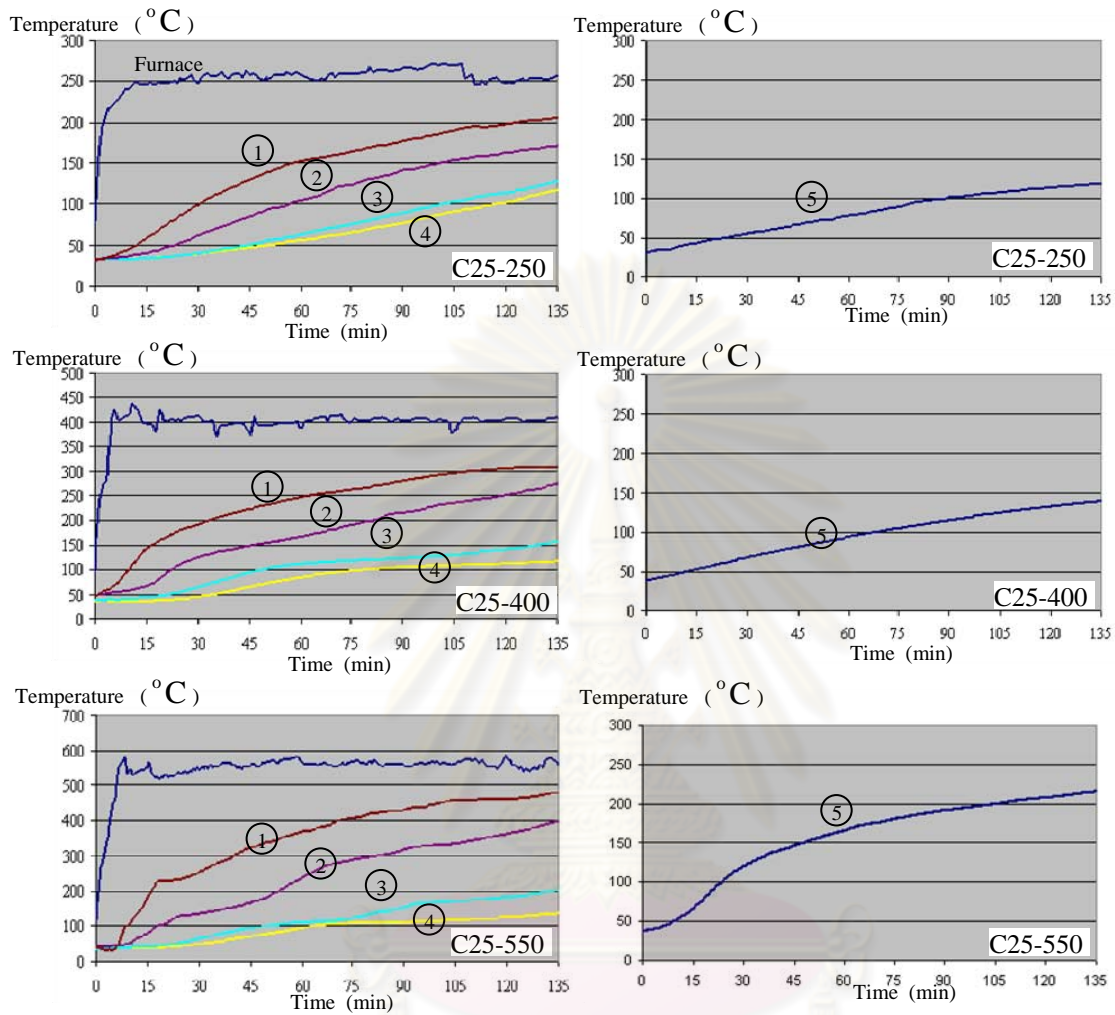
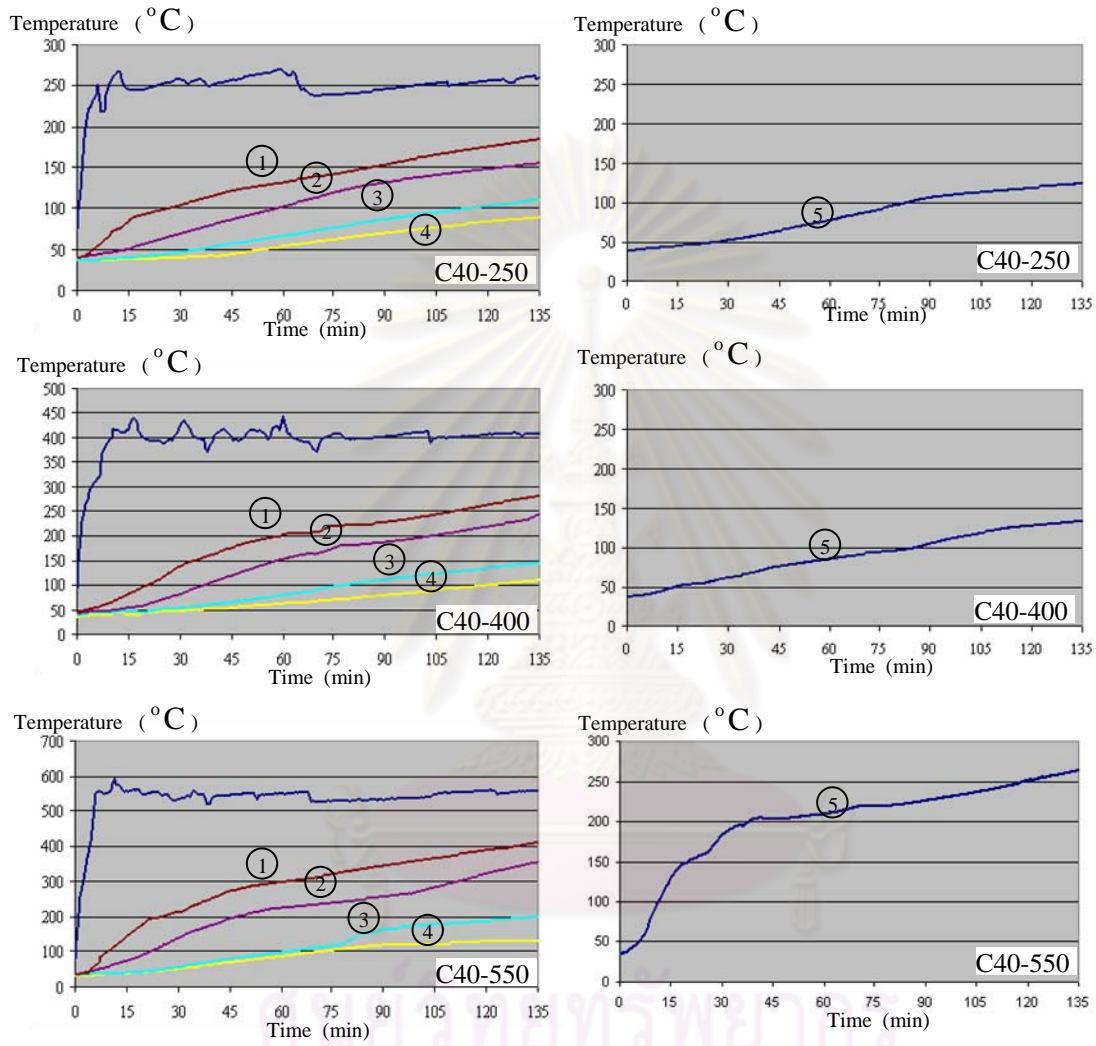


Figure 4.5 Temperature-time curves for the specimens in C25 series



(b)

Figure 4.6 Temperature-time curves for the specimens in C40 series

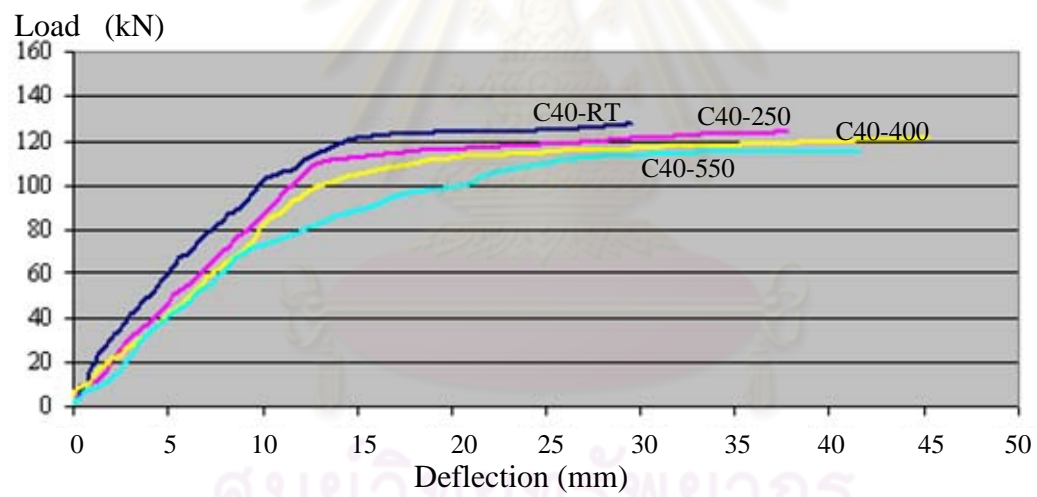
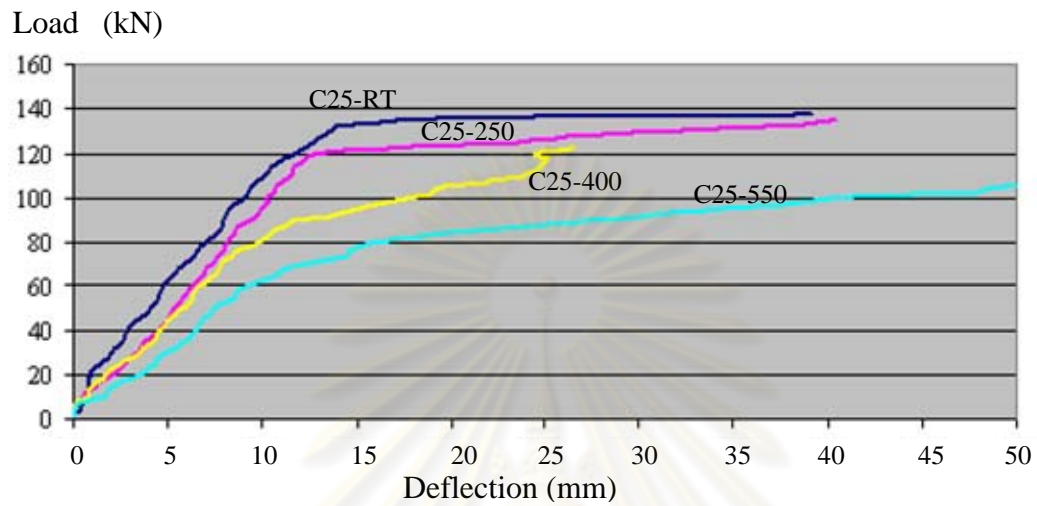


Figure 4.7 Load-deflection curves of the beam specimens

ศูนย์วิจัยทรัพยากร
จุฬาลงกรณ์มหาวิทยาลัย



Figure 4.8 Crack patterns of the beam specimens

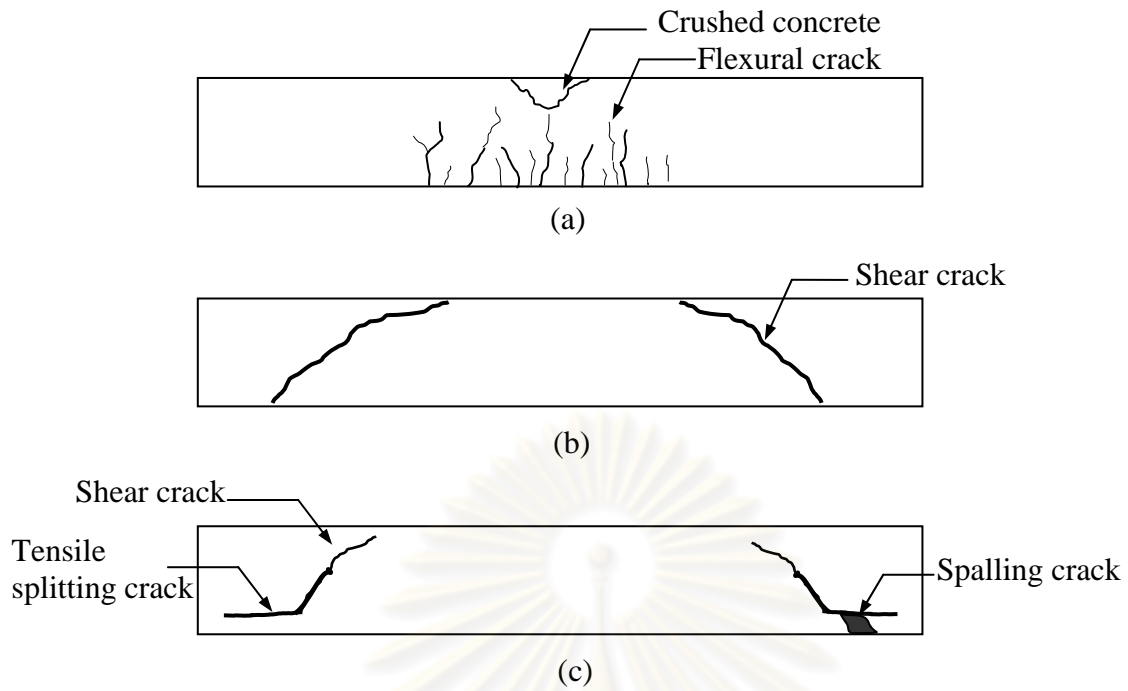


Figure 4.9 Different types of failure: (a) flexural failure; (b) shear failure; and (c) shear failure with tensile spitting cracks

Table 4.2 Types of failure for the beam specimens

Specimen	Type of failure
C25-RT	Flexural
C25-250	Shear with tensile slitting cracks
C25-400	Shear with tensile slitting cracks
C25-550	Flexural
C40-RT	Flexural
C40-250	Flexural
C40-400	Flexural and shear
C40-550	Flexural

4.3 FE Analysis

4.3.1 Structural Modeling

To simulate the thermo-mechanical behavior of the load-bearing beams under elevated temperatures, the commercial finite element software ANSYS was used. Due to symmetry of the test setup, the finite element model involved only a quarter of the beam as shown in Figure 4.10. The finite element analysis of the reinforced concrete beam models was subdivided into three steps to simulate the sequence of the imposed loadings upon each of the beam specimens during the tests. In the first step the beam model was considered to be subject only to the self weight and the initial load due to the loading devices. For the second step, the thermal load, based on the temperature distribution of the beam's cross-section obtained from a separate heat transfer analysis, was superimposed upon the model. In the final step, the load was incrementally applied onto the beam model until structural failure. The overall process of the structural analysis can be illustrated in Figure 4.11.

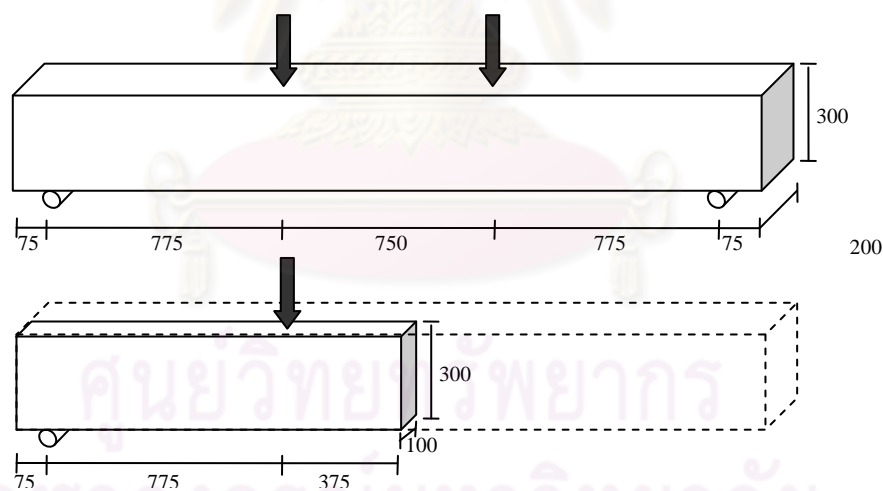


Figure 4.10 Modeling of the beam specimen

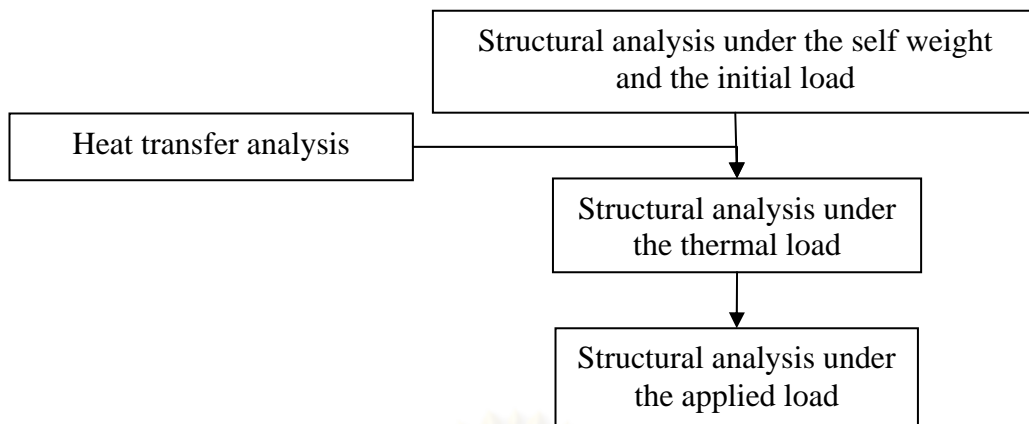


Figure 4.11 Overall process of structural analysis

For the thermal analysis, the beam was modeled with three-dimensional solid elements, solid70, having eight nodes with a single degree of freedom (i.e., temperature) at each node. To simulate the thermal load induced by the ambient temperature increase, the surface element SURF152 was used to account for heat convection and radiation. Because the presence of the steel rebars did not significantly influence the temperature distribution of the beam cross-section (Lie and Irwin 1993), the rebars were not included in the model. The entire beam model was considered to consist only of concrete elements and the temperature of the rebar was assumed to be equal to the temperature of the concrete at the same location. The details of the mesh refinement analysis to determine the appropriate size of element to be used in the thermal analysis model can be found in Appendix A.

The finite element model used for the structural analysis adopted a solid element, solid65, to model concrete; a bar element, link8, to model the steel rebar; and a nonlinear spring element, combine39, to simulate the bond stress-slip mechanism for the rebar in tension. The solid element solid65 is capable of modeling concrete cracking in tension and crushing in compression based on the smear crack theory. The deformation of the element is characterized by eight nodes having three degrees of freedom at each node: translations in the nodal x, y, and z directions. The 2-node bar element link8 is a uniaxial tension-compression element having three degrees of freedom at each node: translations in the nodal x, y, and z directions, with plasticity and large deflection capabilities. The nonlinear spring element combine39 is a uniaxial element defined by two nodes with nonlinear generalized force-deflection capability accounting for large displacements.

The influence of the bond-slip relationship for the cases of perfect bonding and slip bonding was modeled through the connections between the solid concrete elements and the steel bar elements. For perfect bonding, the solid element and the rebar element were set to share the same node at the connection whereas for slip bonding the nodes of the solid element were linked with the nodes of the bar element by using the non-linear spring element (Amatavirakul 2008). The stirrups and the compression reinforcement were assumed to be in perfect bond. The finite element models of the beam for thermal and structural analyses can be illustrated in Figure 4.12.

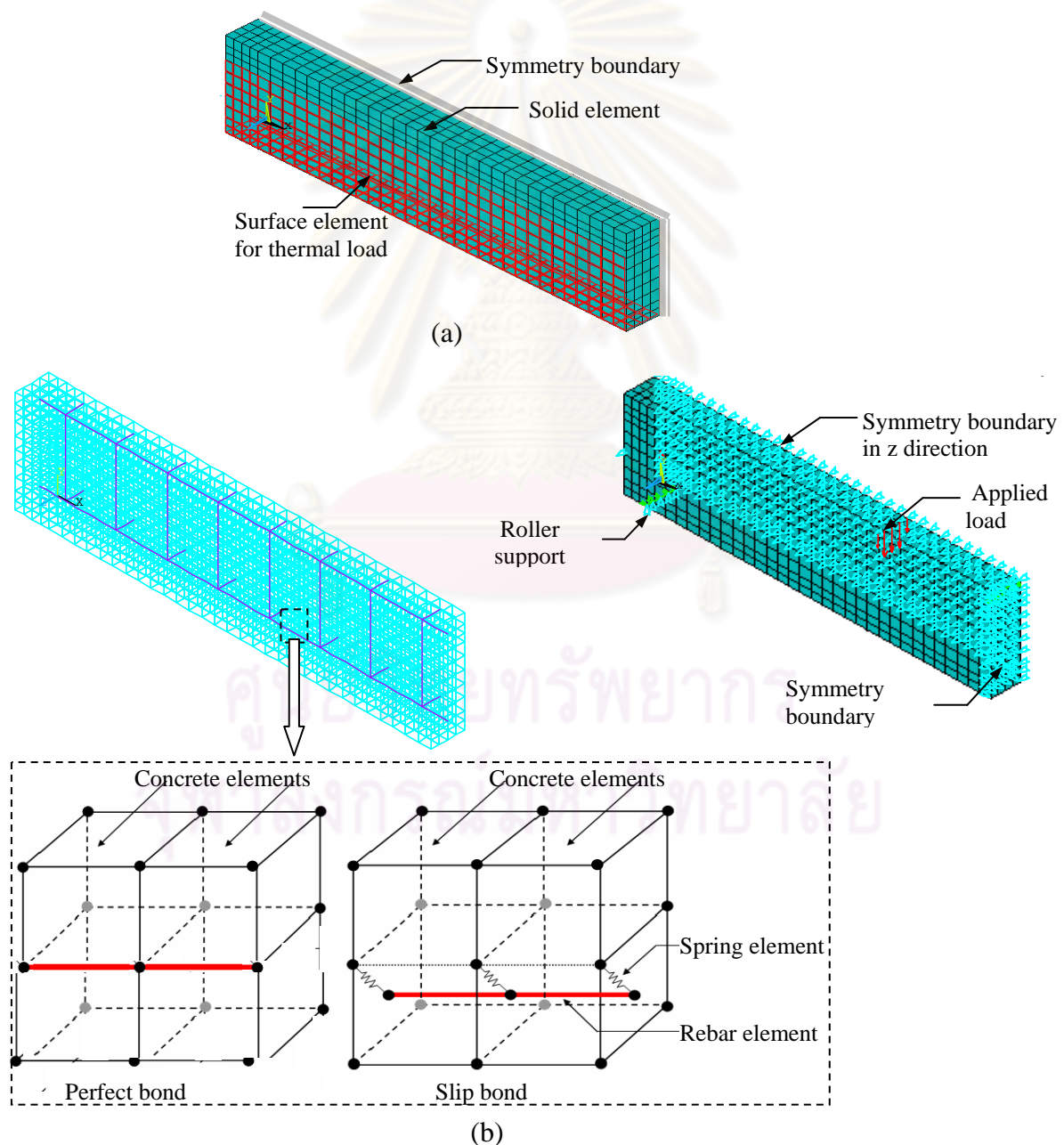


Figure 4.12 Finite element models for: (a) thermal analysis and (b) structural analysis

4.3.2 Thermal and Mechanical Properties

The thermal and mechanical properties of the reinforcing steel and concrete as previously described in Section 2.5.2 were employed for the current study. The normalized tensile stress-strain relationship for steel in accordance with BS EN 1992-1-2 (2004) was converted into the general form based on the tested properties as shown in Figure 4.13. The stress-strain relationship for concrete in compression was assumed to follow the normalized stress-strain relationship of BS EN 1992-1-2 (2004) until the peak stress and to be perfectly plastic thereafter (Ibrahim and Mahmood 2009) as shown in Figure 4.14 (a). The tensile stress-strain relationship for concrete was specified by the tensile strength and the modulus of elasticity as shown in Figure 4.14 (b). The shear transfer coefficients for the opening and the closing cracks were set to 0.30 and 0.50, respectively (Zhou *et al.* 2004). It should also be noted herein that the confinement effect on the concrete section due to the differential expansion between the outer elements exposed to fire and the inside was neglected for the current study. As such, the thermal expansion coefficients were not required in the finite element model (Piloto *et al.* 2006).

The average temperatures of the rebars and the surrounding concrete required to compute the bond-slip relationship were obtained from the heat transfer analysis using the finite element model with 5-mm element mesh as shown in Figure 4.15. The average temperature of the surrounding concrete was computed from the nodal temperatures of the concrete elements within the circle zone whereas the average temperature of the rebar was computed from the nodal temperatures of the rebar elements within the rectangular zone. The average temperatures and the corresponding bond-slip relationships are shown in Table 4.3 and Figure 4.16, respectively. Note that similar to the stress-strain relationship for concrete in compression the bond-slip relationship was assumed to follow the proposed model until the peak stress and to be perfectly plastic thereafter until the ultimate slip. This assumption enhanced the stability of the FE analysis for the investigation of the tensile splitting cracks.

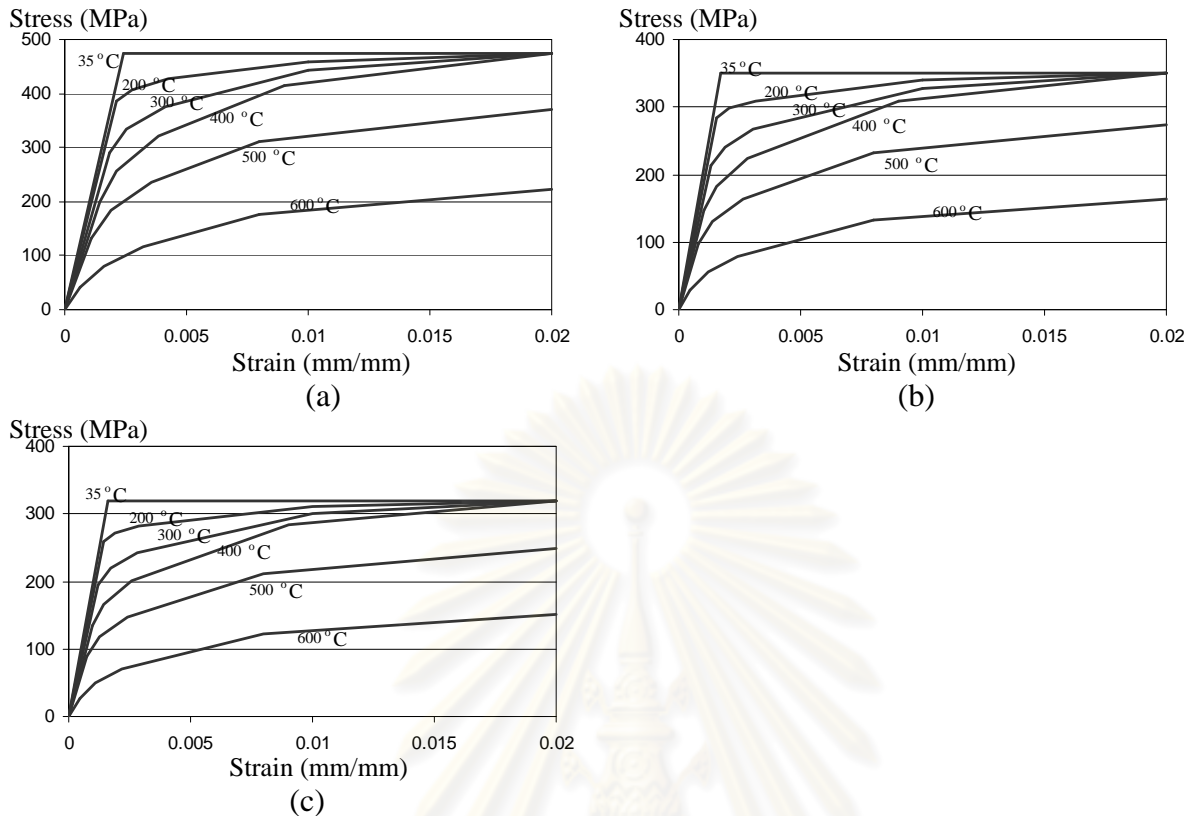


Figure 4.13 Variation of the tensile stress-strain relationships for steel with temperature (BS EN 1992-1-2 (2004)): (a) DB 16; (b) RB 9; and (c) RB 6

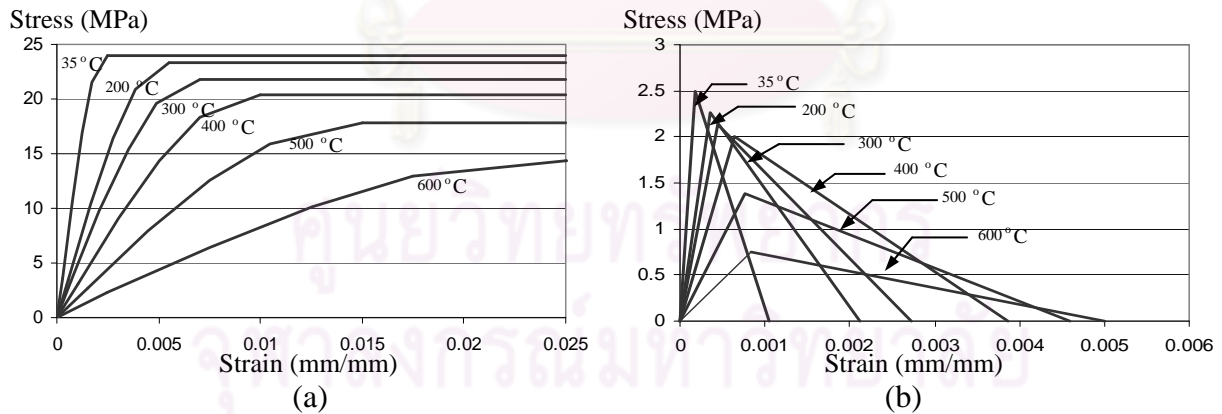


Figure 4.14 Variation of the stress-strain relationships for concrete with temperature: (a) compressive stress-strain relationship; and (b) tensile stress-strain relationship

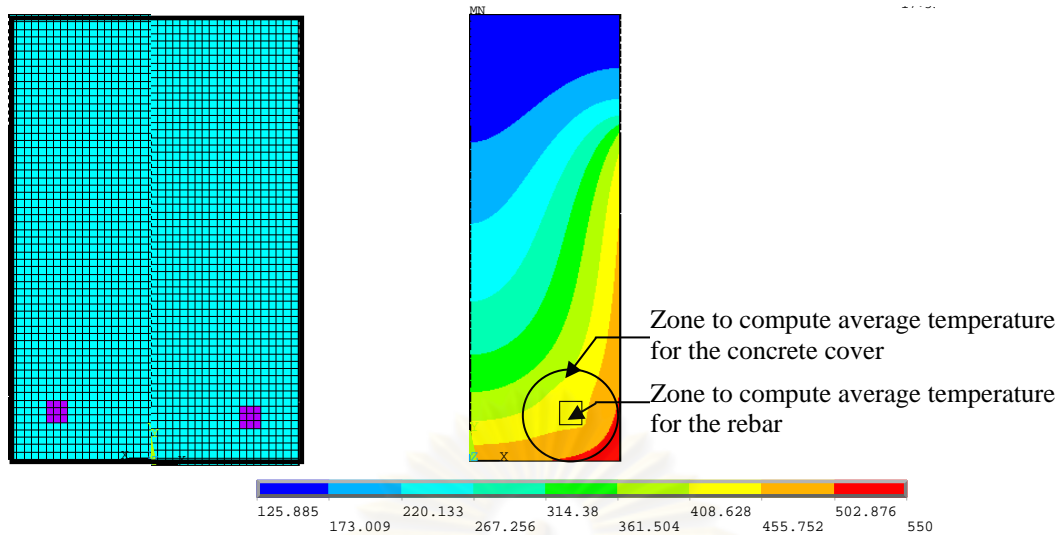


Figure 4.15 Finite element model for the heat transfer analysis to obtain the bond stress-slip curve

Table 4.3 Average temperatures for the bond stress-slip curves

Specimen	Average temperature ($^{\circ}\text{C}$)	
	Concrete cover	Reinforcing steel
C25-RT	35	35
C25-250	202	198
C25-400	327	320
C25-550	459	447
C40-RT	35	35
C40-250	187	180
C40-400	299	286
C40-550	417	395

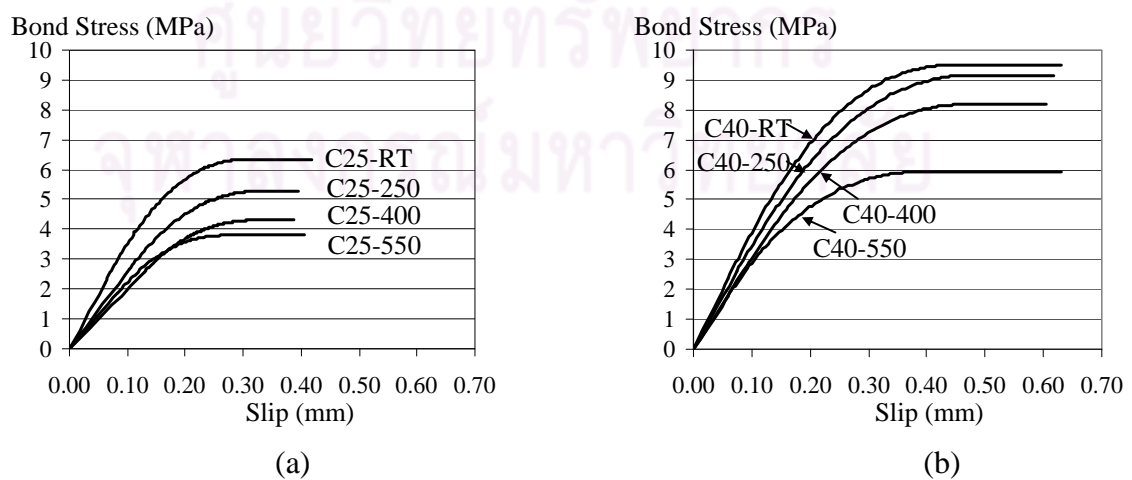


Figure 4.16 Bond-slip relationships for the finite element analysis:

(a) C25 series and (b) C40 series

4.4 Finite Element Analysis Results and Discussions

The load-deflection curves for the beam specimens obtained from the experiment were compared with the results from the FE analysis for the cases of perfect bond and slip bond (the proposed model) as shown in Figure 4.17. The comparison reveals that the overall analytical results are consistent with the experimental results. It is observed that the initial slope of the load-deflection curves obtained from the FE models is slightly higher compared with the test results in which the behavior of the FE models with slip bond only slightly differs from those with perfect bond.

The graphical representation of the cracks obtained from the FE models of the beam specimens can be illustrated in Figure 4.18. In the illustration, the crack planes that occur within the concrete elements are represented by using straight lines. These crack planes correspond with the directions perpendicular to which the principal stresses exceed the tensile strength of concrete. Because several crack planes can occur within each of the concrete elements, different color codes are used for illustrating the order of their appearance. Red, green and blue lines are used to represent the first, second and third crack planes in their consecutive order to initiate within each concrete element.

In terms of the crack pattern, three different types of crack, i.e. flexure, bond and shear cracks, can be observed in the beam model as shown in Figure 4.18. Under the applied load, tension is induced in the rebars and the concrete elements in the lower part of the beam specimen. Once the tensile stresses in the concrete elements reach the tensile strength, the flexural cracks are initiated and can propagate to the upper part, particularly at the middle of the beam's span. The flexural cracks are normally represented by a group of vertical lines as can be seen in Figure 4.18. The tensile force induced in the steel rebars is also transferred to the surrounding concrete through the bonding mechanism causing cracking of the surrounding concrete elements along the length of the rebars. These cracks are generally referred to as the bond cracks and can extend to the end of the rebar due to the bond stress distribution. Note that because the bond cracks are normally generated only at the interface between the rebars and the concrete cover, the cracks may not be observed in the actual experiment. However,

once the bond strength is reached, the bond cracks may appear in the form of the tensile splitting cracks. For the current study the bond cracks in the beam model can be observed as a group of short inclined lines along the length of the rebar as shown in Figure 4.18. In addition to the flexural cracks and the bond cracks, the shear cracks can occur if the stresses in the concrete elements within the shear zone reach the tensile strength. The shear cracks in the beam model can be observed as inclined lines around the mid-height of the beam in the shear zone as shown in Figure 4.18.

The variation of the crack patterns with respect to the increasing load steps obtained from the FE models for each of the specimens in both C25 and C40 series can be illustrated in Figures 4.19 to Figure 4.26. It can be seen from the illustrations that, at the initial stage of loading, the flexural cracks and the bond cracks for the FE models with perfect bond are more spatially distributed around the middle of the span length whereas the FE models with slip bond provide only a few discrete groups of flexural cracks and bond cracks. As the level of load is increased, the shear cracks can be observed in addition to the flexural and bond cracks. Moreover, more bond cracks can be observed along the length of the rebars. Compared to the FE models with perfect bond, fewer bond cracks are observed in the FE models with slip bond which is probably due to the fact that the tensile force in the rebars can be more gradually transferred to the surrounding concrete elements. At the peak load, it is nevertheless found that the overall crack patterns of the FE models with perfect bond and slip bond are similar based on the distribution of the cracks and the direction of the crack planes.

The comparison between the test results and the modeling results for the beam specimens at room temperature (see Figure 4.19 and Figure 4.23) reveals that only the flexural cracks are observed in the test specimens while the shear cracks can also be observed in the FE models in addition to the flexural cracks. Therefore, it can sometimes be difficult to predict the actual mode of failure for the beam specimens based only upon the crack patterns obtained from the FE models. Nevertheless, the load-displacement curves obtained from the FE models are consistent with the experimental results which imply that the overall crack strains can still be accurately estimated.

The variation of the tensile force and the bond stress distribution along the length of the rebar with respect to the increasing load steps for the FE models of the beam specimens in both C25 and C40 series can be illustrated in Figures 4.27 to Figure 4.34. It is observed that the tensile force reaches its maximum value around the beam's mid-span and its minimum value at the end of the rebar, respectively. Note that since the tensile force distribution corresponds with the transfer of forces between the tension rebars and the surrounding concrete through the bonding mechanism, the bond stresses can be derived directly from the difference of the tensile forces between adjacent rebar elements.

The bond stress distribution is observed to vary with the level of cracking of the concrete elements. If the concrete elements are completely cracked (i.e., total loss of tension resistance), the tensile force in the rebars can no longer be transferred to concrete, resulting in zero bond stress. For severely cracked concrete elements, the bond stress can significantly decrease and the tensile force transfer must be compensated by the increase in the bond stress of the adjacent concrete elements as evident from the undulation of the bond stress distribution corresponding to the location of the cracks.

It is seen from in Figures 4.27 to Figure 4.34 that the maximum bond stresses around the support at the peak load obtained from the FE models with perfect bond are significantly higher than those with slip bond. Based on the experimental results, the tensile splitting cracks were observed for C25-250, C25-400 and C25-550 specimens, which agree with the results obtained from the proposed model with slip bond in that the bond strength within the spring elements is reached and that the tensile splitting cracks occur. Whilst, for the FE models with perfect bond, without the spring elements the bond strength is not limited and the bond stresses tend to be overestimated. In the experiment, the tensile splitting cracks were also observed as the reason for failure of C25-250 and C25-400 specimens. However, the tensile splitting cracks were not observed for the specimens in C40 series because of their better splitting resistance under the thermal loads.

Based on the experimental results, the shear failure was observed for C40-400 specimen and the shear failure with tensile splitting cracks was observed for C25-250 and C25-400 specimens. However, the results obtained from the FE models suggest that the tension rebars yield at the peak loads of these specimens. It can thus be suspected that the shear failures observed in the experiment might occur after yielding of the tension rebars.

In summary, it is found that the FE models with perfect bond and slip bond provide similar results in terms of the load-deflection curve, the crack pattern and the tensile force distribution along the rebars. For the bond stress distribution, the FE models with slip bond are capable of predicting the tensile splitting cracks in the beam specimens by using the spring elements whereas the FE models with perfect bond tend to overestimate the bond stresses.



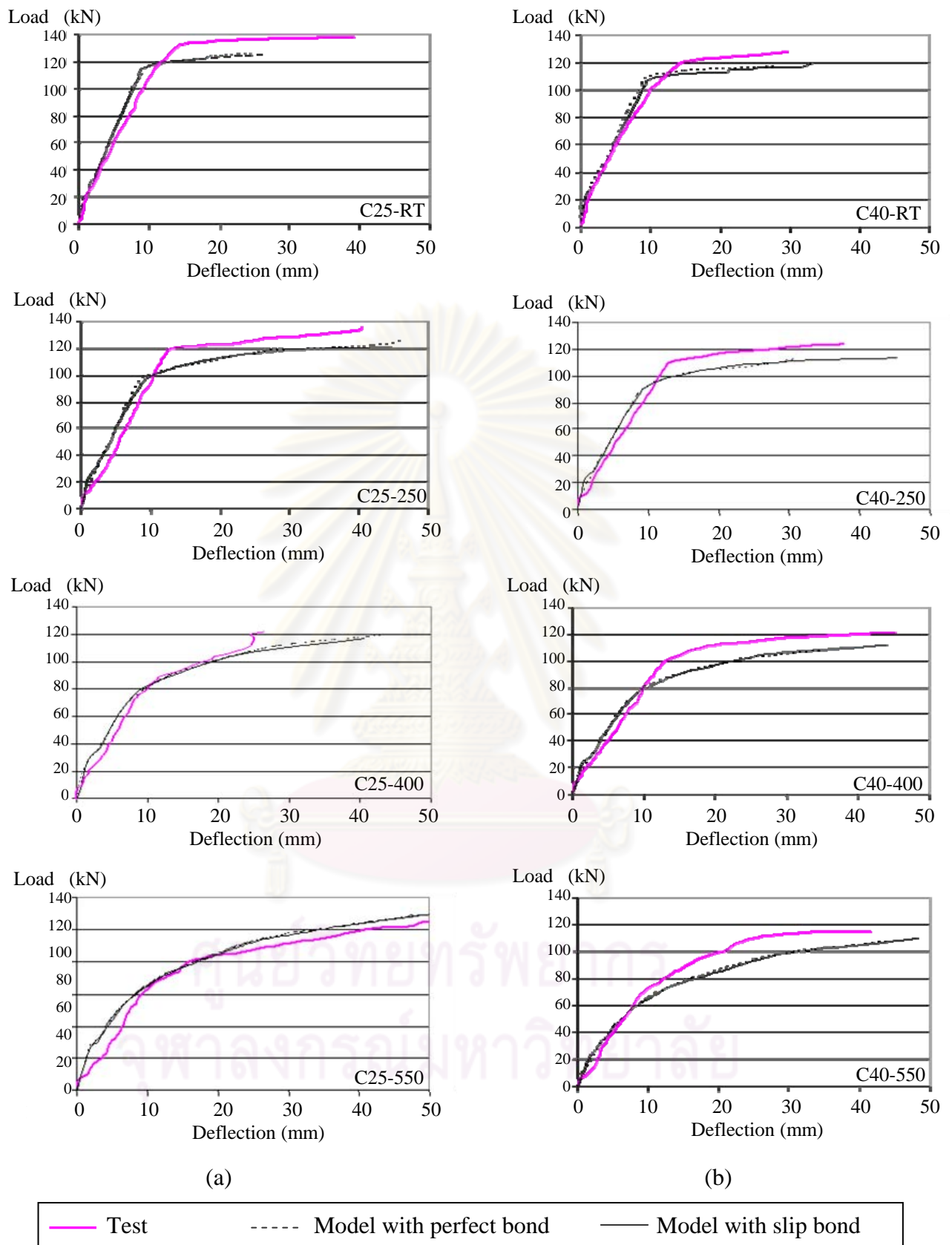


Figure 4.17 Comparison of the load-deflection curves obtained from the experiment and the FE analysis: (a) C25 series and (b) C40 series

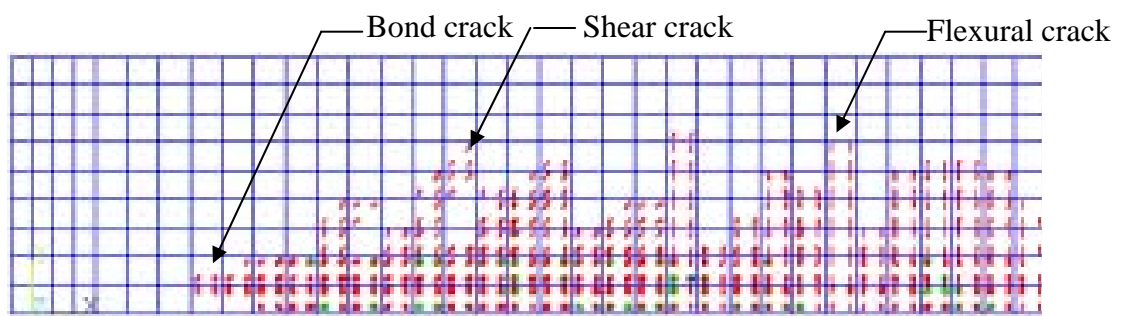
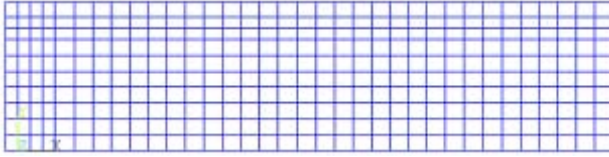


Figure 4.18 Graphical representation of cracks

ศูนย์วิทยทรัพยากร
จุฬาลงกรณ์มหาวิทยาลัย

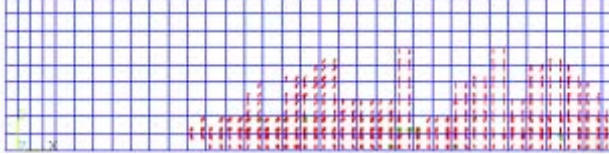
Load 20 kN



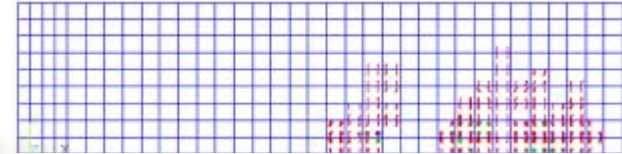
Load 20 kN



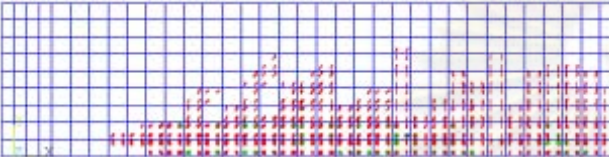
Load 40 kN



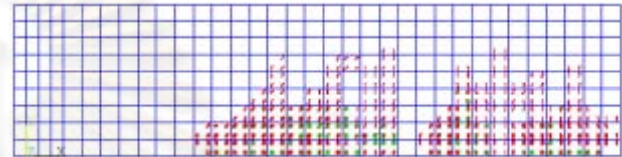
Load 40 kN



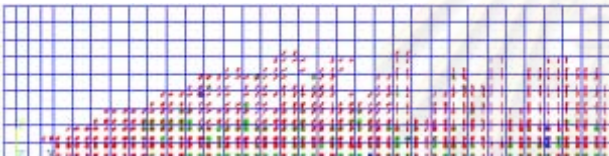
Load 60 kN



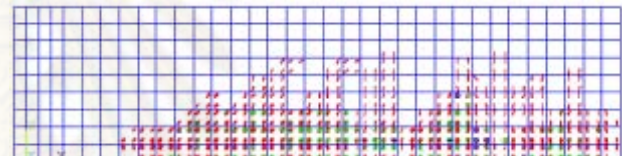
Load 60 kN



Load 80 kN



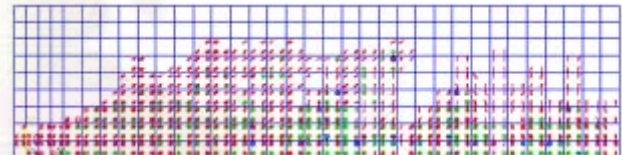
Load 80 kN



Load 100 kN



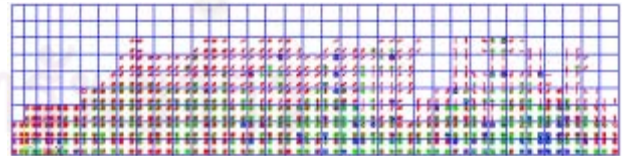
Load 100 kN



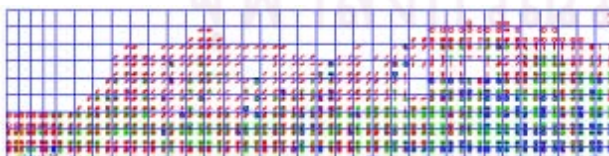
Load 120 kN



Load 120 kN



Load 128 kN



Load 128 kN



(a)

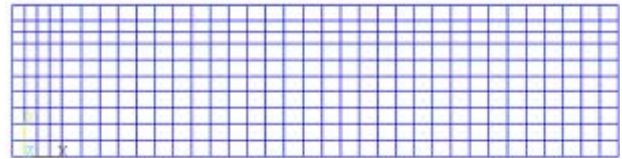
(b)

Figure 4.19 Variation of the crack patterns with load for C25-RT:
 (a) FE analysis with perfect bond and (b) FE analysis with slip bond

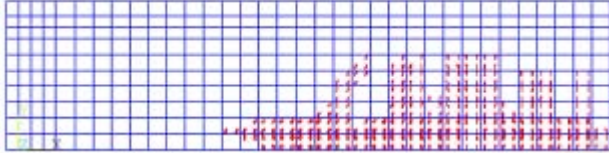
Load 20 kN



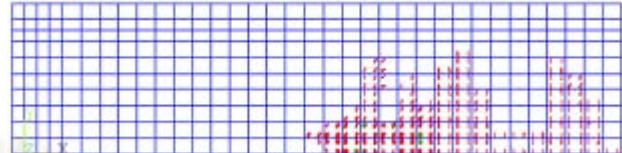
Load 20 kN



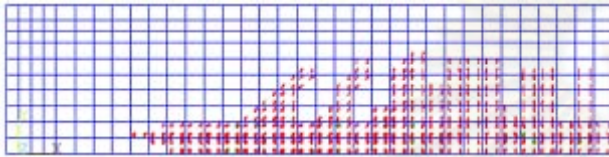
Load 40 kN



Load 40 kN



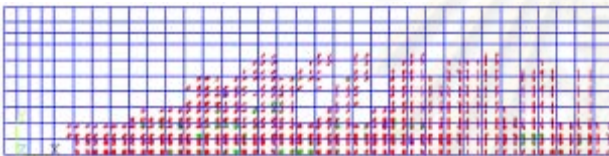
Load 60 kN



Load 60 kN



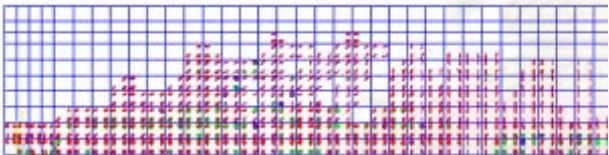
Load 80 kN



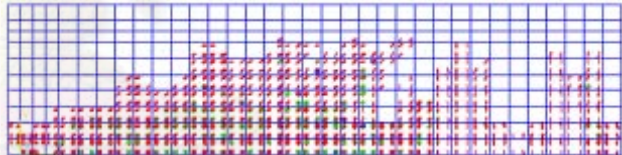
Load 80 kN



Load 100 kN



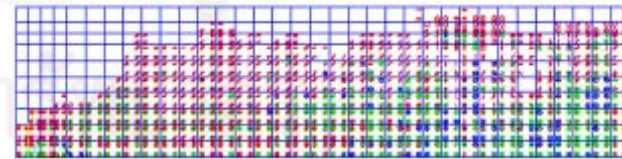
Load 100 kN



Load 120 kN



Load 120 kN

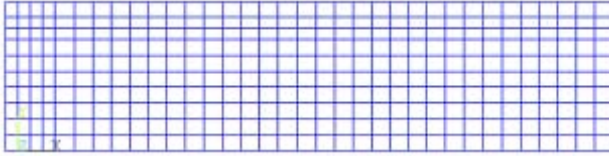


(a)

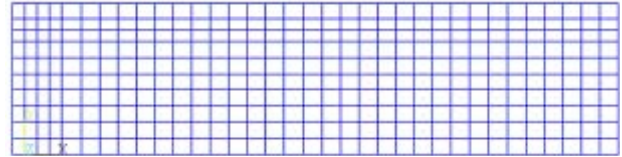
(b)

Figure 4.20 Variation of the crack patterns with load for C25-250:
 (a) FE analysis with perfect bond and (b) FE analysis with slip bond

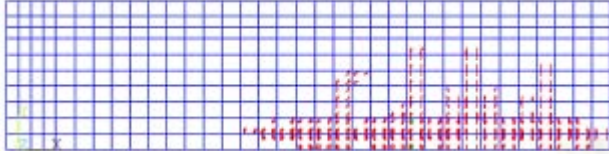
Load 20 kN



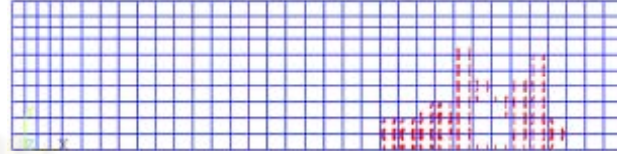
Load 20 kN



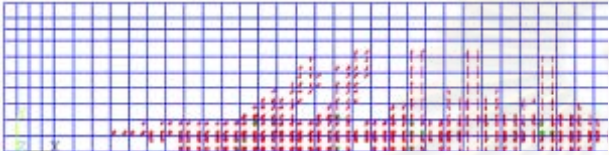
Load 40 kN



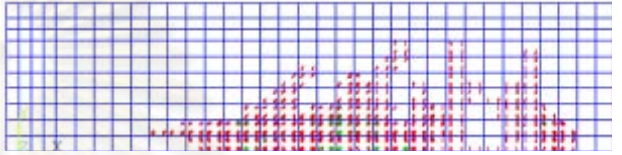
Load 40 kN



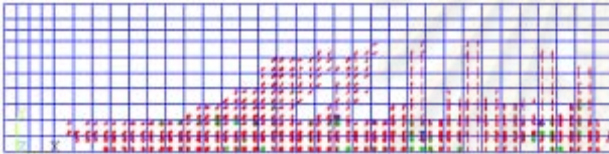
Load 60 kN



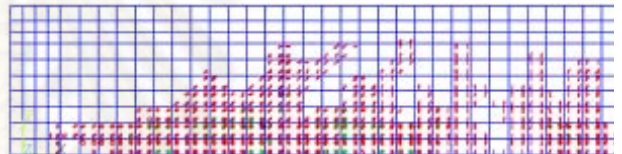
Load 60 kN



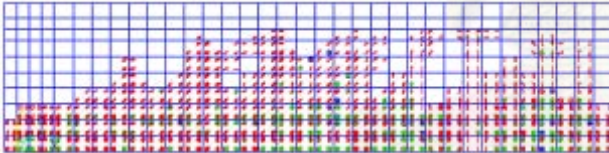
Load 80 kN



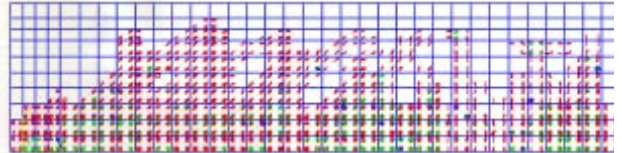
Load 80 kN



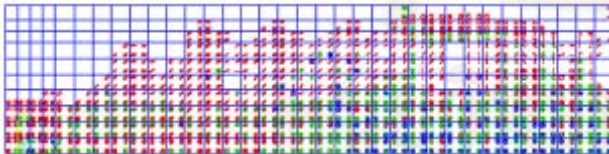
Load 100 kN



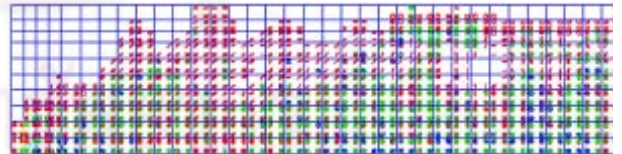
Load 100 kN



Load 120 kN



Load 120 kN

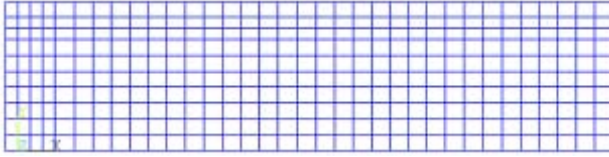


(a)

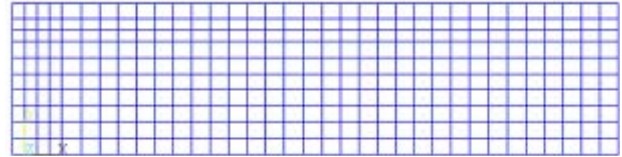
(b)

Figure 4.21 Variation of the crack patterns with load for C25-400:
 (a) FE analysis with perfect bond and (b) FE analysis with slip bond

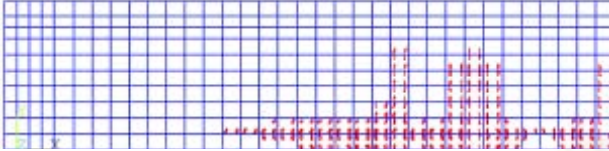
Load 20 kN



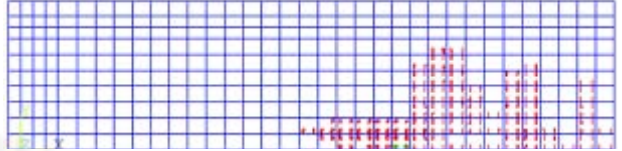
Load 20 kN



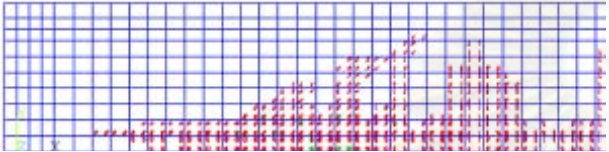
Load 40 kN



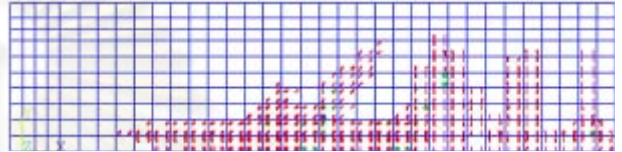
Load 40 kN



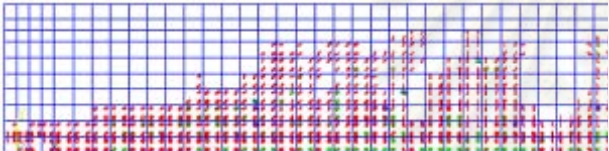
Load 60 kN



Load 60 kN



Load 80 kN



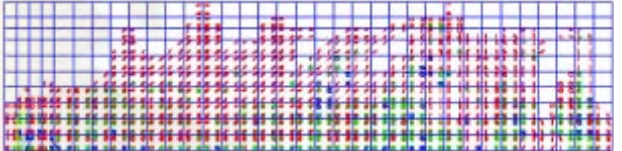
Load 80 kN



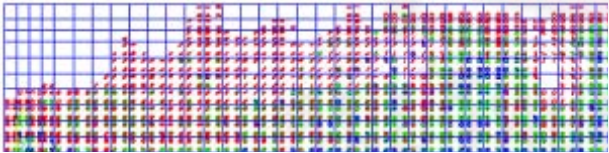
Load 100 kN



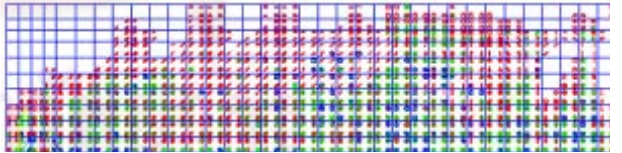
Load 100 kN



Load 110 kN



Load 110 kN

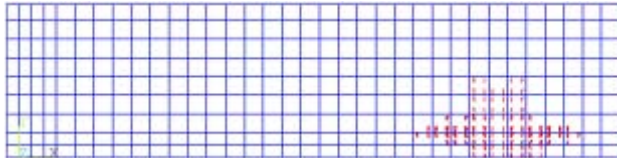


(a)

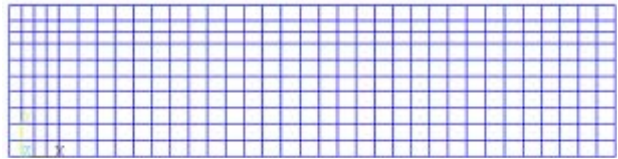
(b)

Figure 4.22 Variation of the crack patterns with load for C25-550:
 (a) FE analysis with perfect bond and (b) FE analysis with slip bond

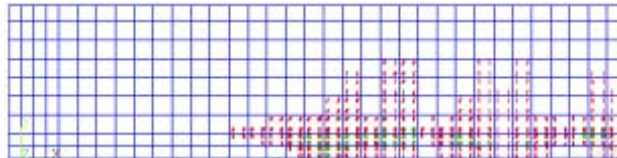
Load 20 kN



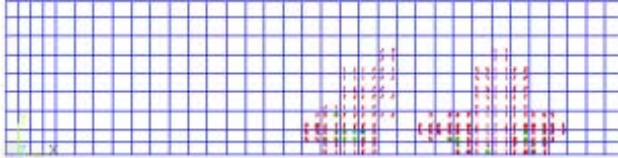
Load 20 kN



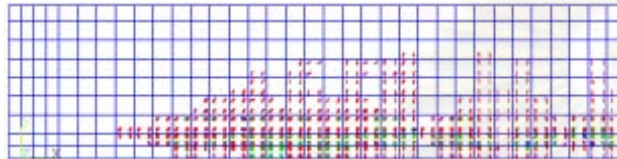
Load 40 kN



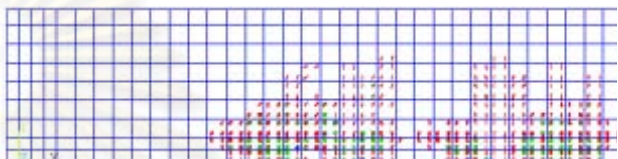
Load 40 kN



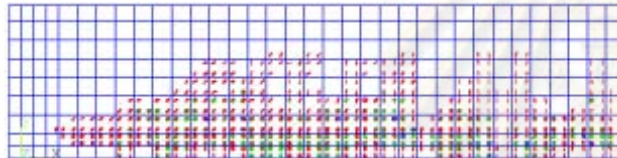
Load 60 kN



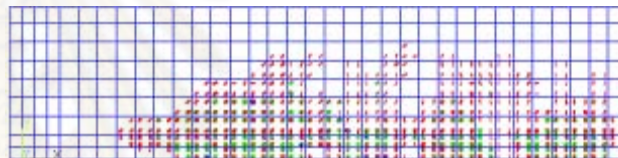
Load 60 kN



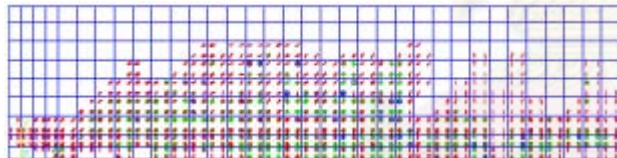
Load 80 kN



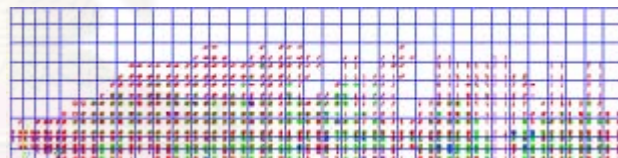
Load 80 kN



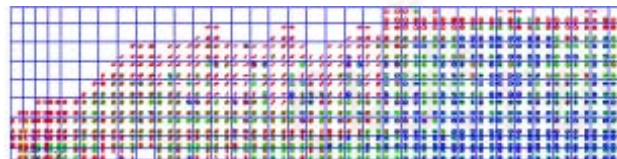
Load 100 kN



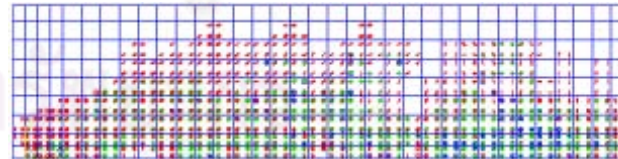
Load 100 kN



Load 120 kN



Load 120 kN

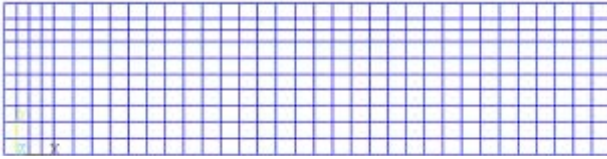


(a)

(b)

Figure 4.23 Variation of the crack patterns with load for C40-RT:
 (a) FE analysis with perfect bond and (b) FE analysis with slip bond

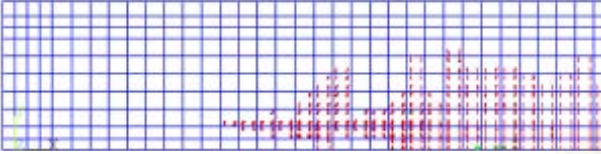
Load 20 kN



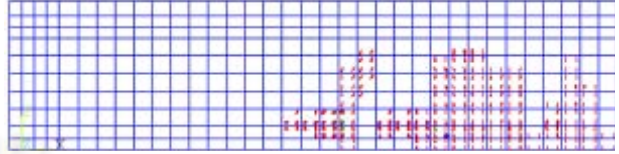
Load 20 kN



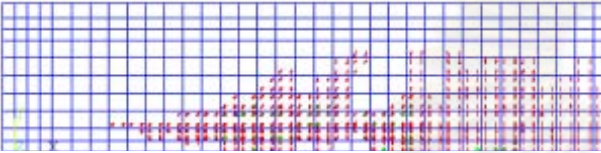
Load 40 kN



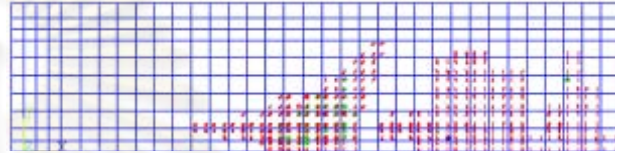
Load 40 kN



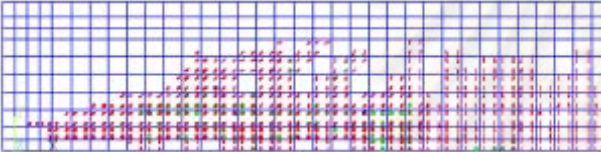
Load 60 kN



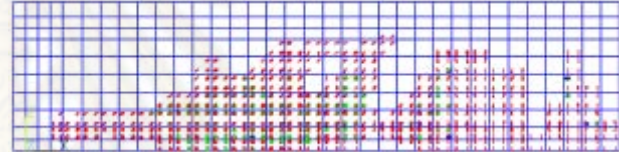
Load 60 kN



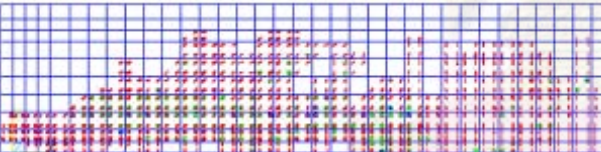
Load 80 kN



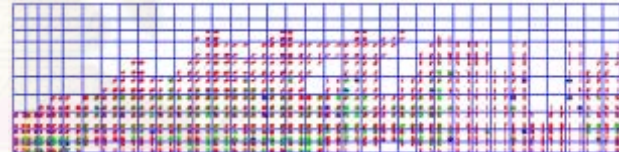
Load 80 kN



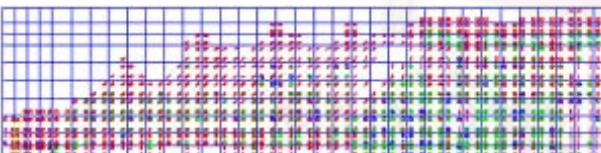
Load 100 kN



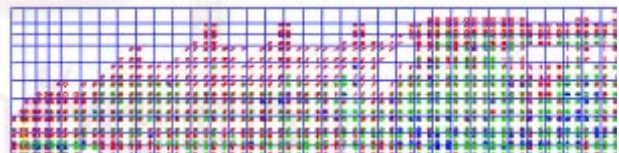
Load 100 kN



Load 112 kN



Load 112 kN

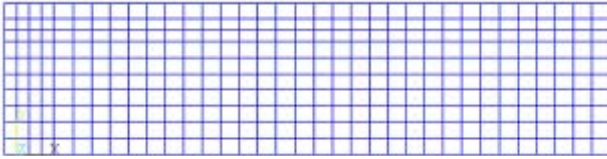


(a)

(b)

Figure 4.24 Variation of the crack patterns with load for C40-250:
 (a) FE analysis with perfect bond and (b) FE analysis with slip bond

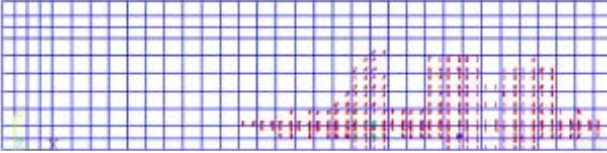
Load 20 kN



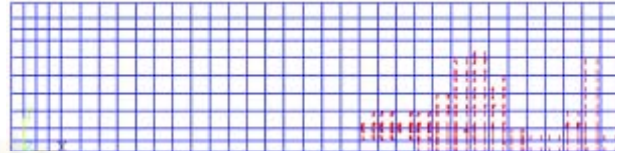
Load 20 kN



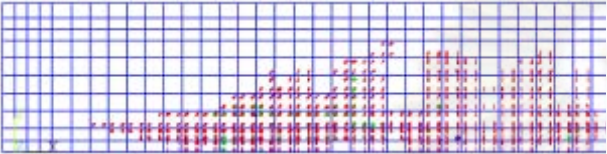
Load 40 kN



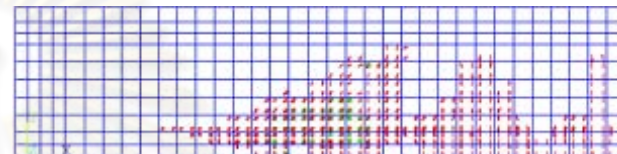
Load 40 kN



Load 60 kN



Load 60 kN



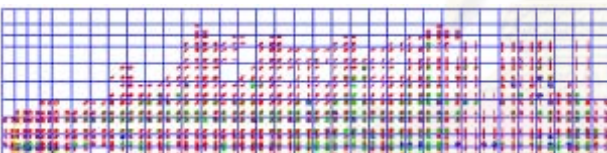
Load 80 kN



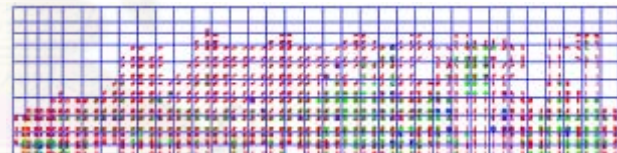
Load 80 kN



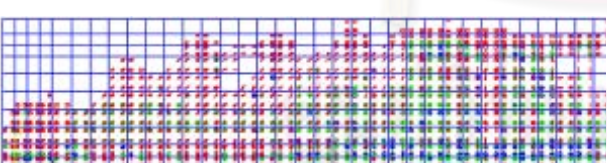
Load 100 kN



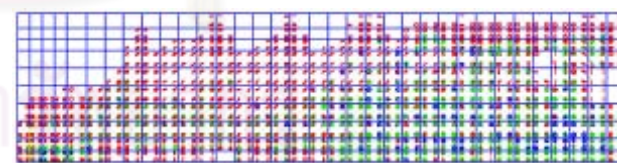
Load 100 kN



Load 112 kN



Load 112 kN



(a)

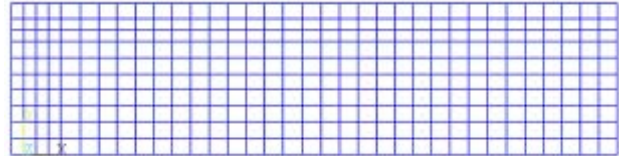
(b)

Figure 4.25 Variation of the crack patterns with load for C40-400:
 (a) FE analysis with perfect bond and (b) FE analysis with slip bond

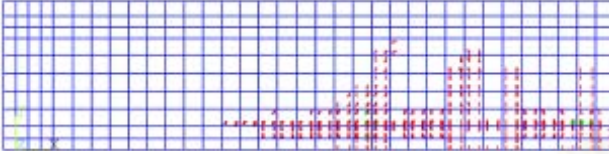
Load 20 kN



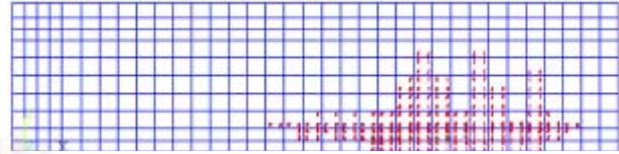
Load 20 kN



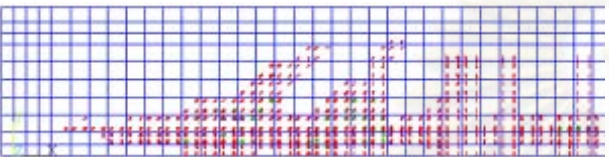
Load 40 kN



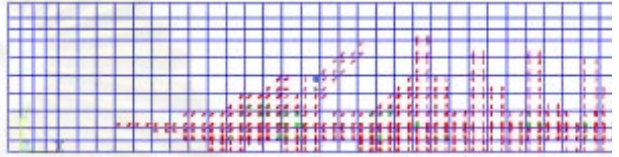
Load 40 kN



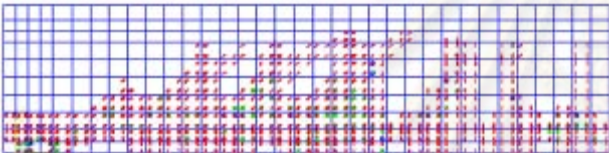
Load 60 kN



Load 60 kN



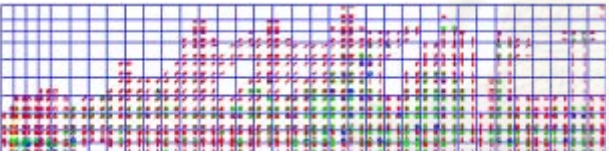
Load 80 kN



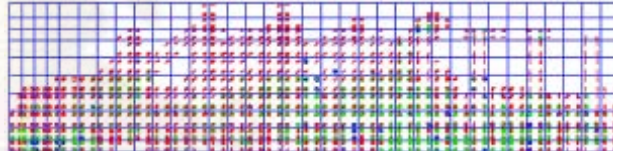
Load 80 kN



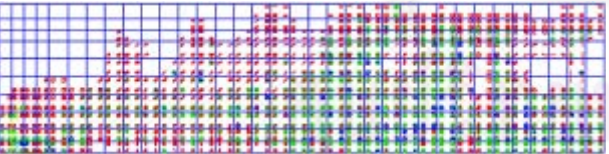
Load 100 kN



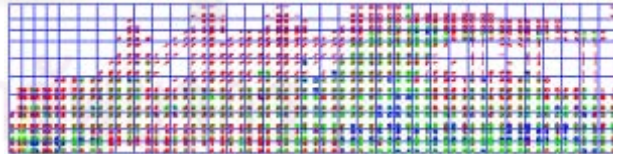
Load 100 kN



Load 110 kN



Load 110 kN



(a)

(b)

Figure 4.26 Variation of the crack patterns with load for C40-550:
 (a) FE analysis with perfect bond and (b) FE analysis with slip bond

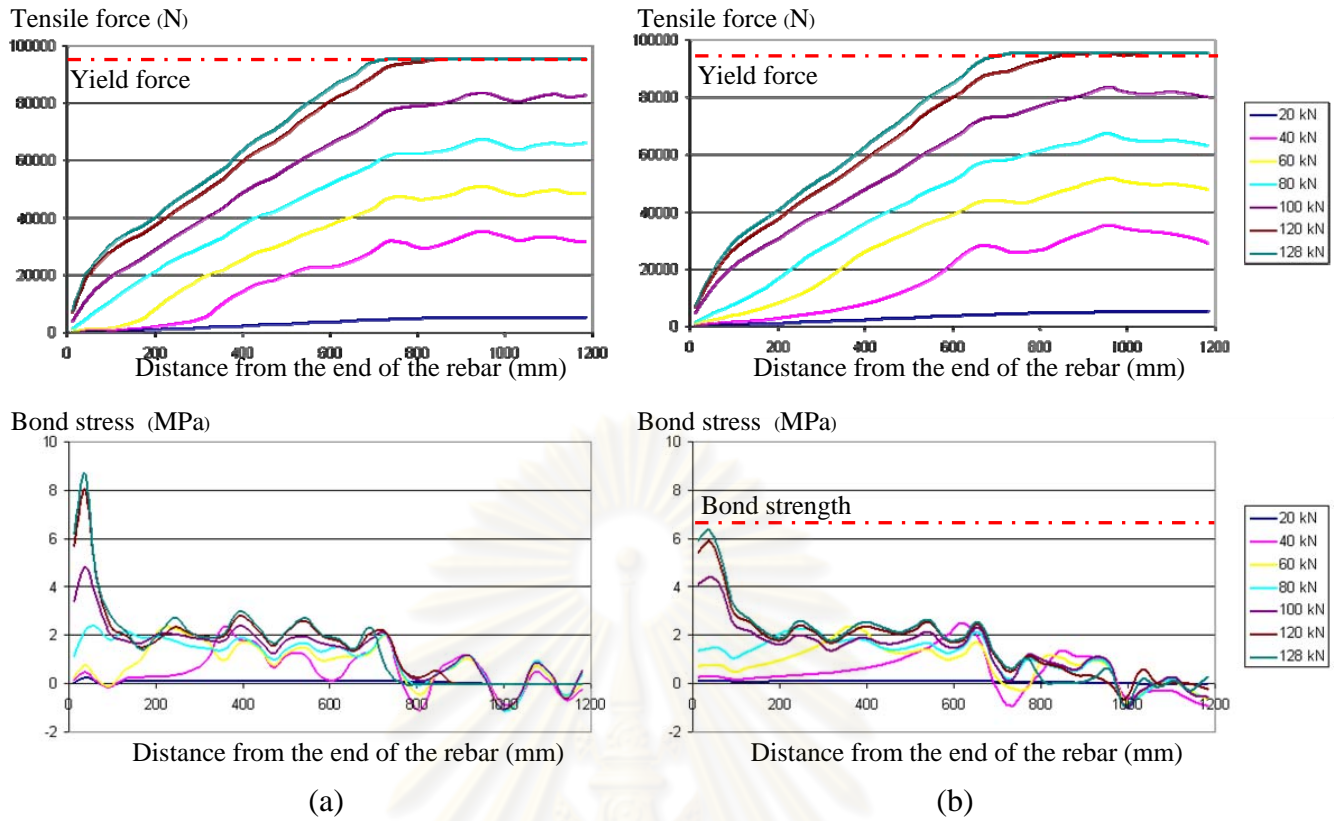


Figure 4.27 Variation of the tensile force and the bond stress distribution along the rebar with load for C25-RT: (a) FE model with perfect bond and (b) FE model with slip bond

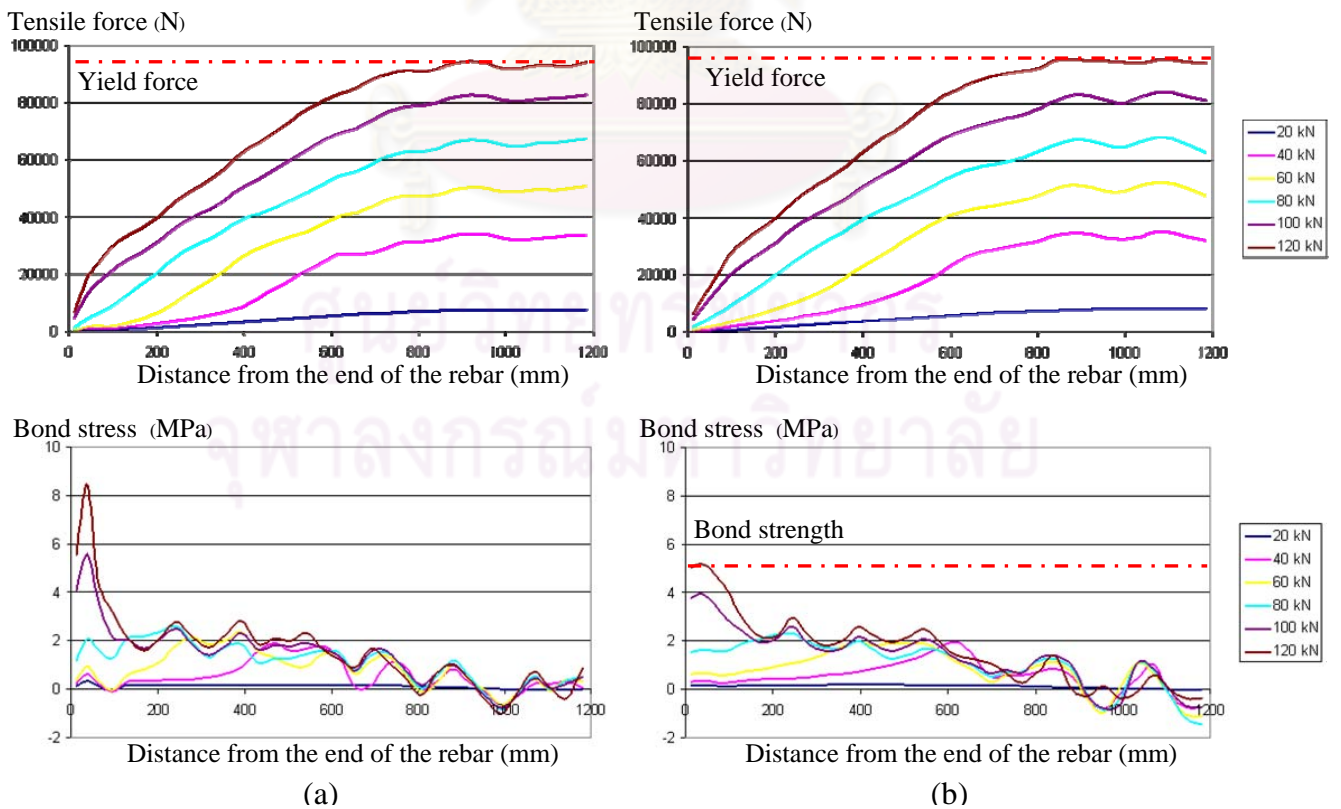


Figure 4.28 Variation of the tensile force and the bond stress distribution along the rebar with load for C25-250: (a) FE model with perfect bond and (b) FE model with slip bond

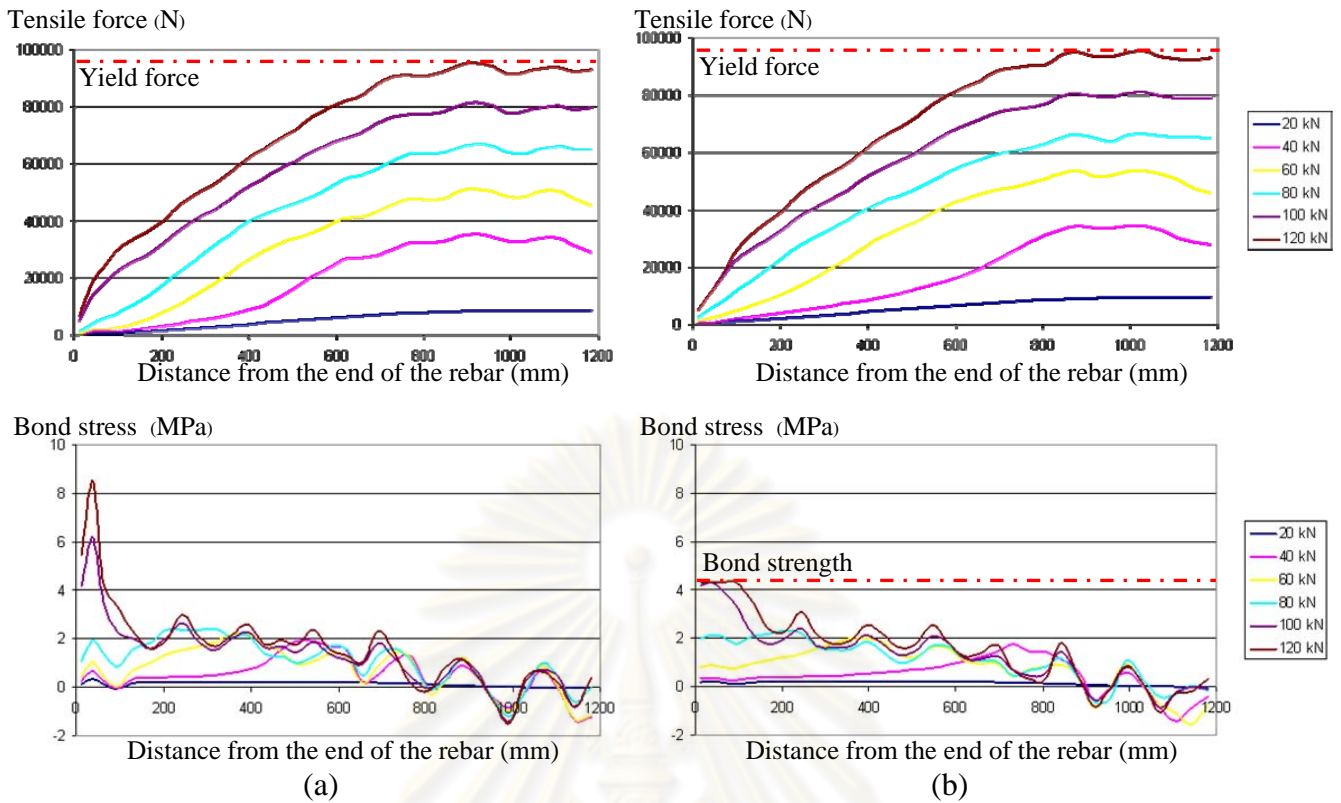


Figure 4.29 Variation of the tensile force and the bond stress distribution along the rebar with load for C25-400: (a) FE model with perfect bond and (b) FE model with slip bond

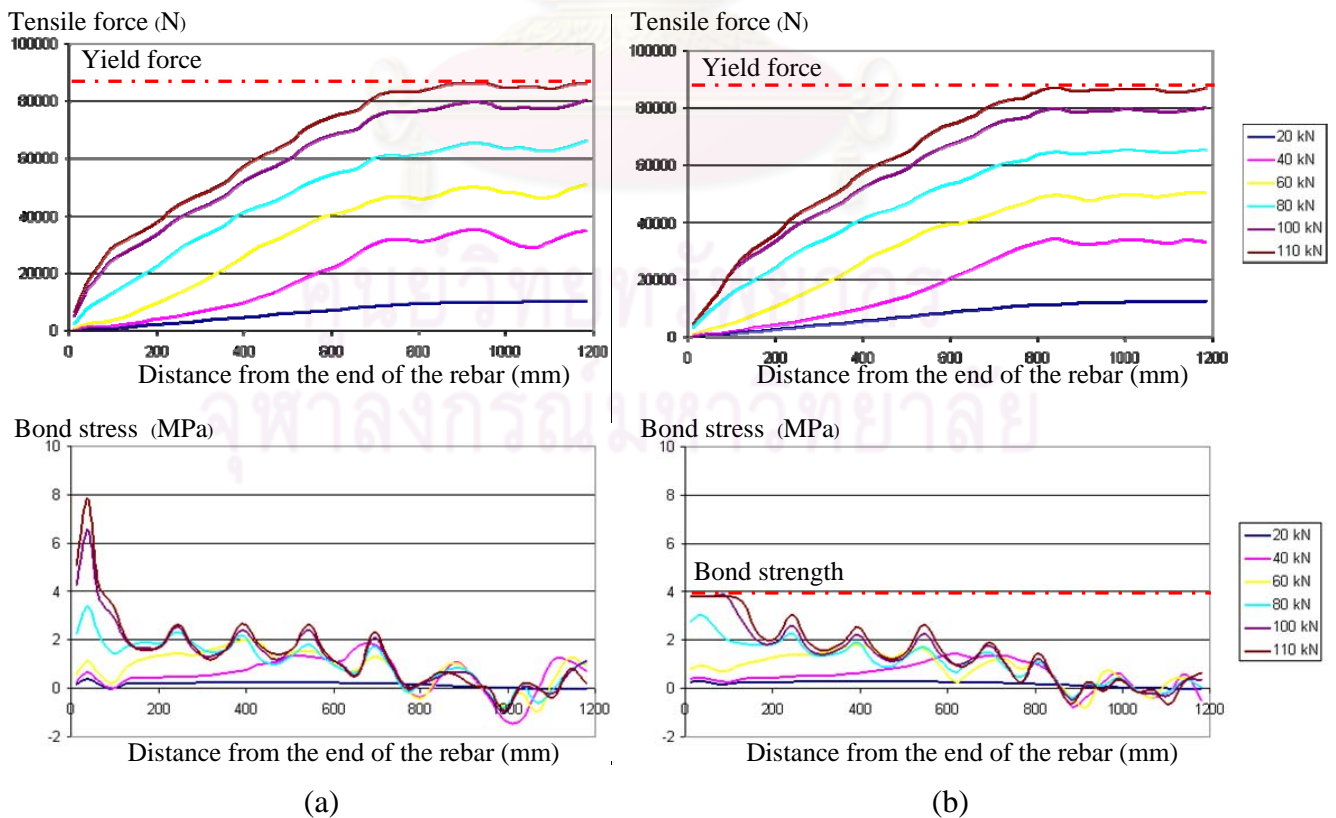


Figure 4.30 Variation of the tensile force and the bond stress distribution along the rebar with load for C25-550: (a) FE model with perfect bond and (b) FE model with slip bond

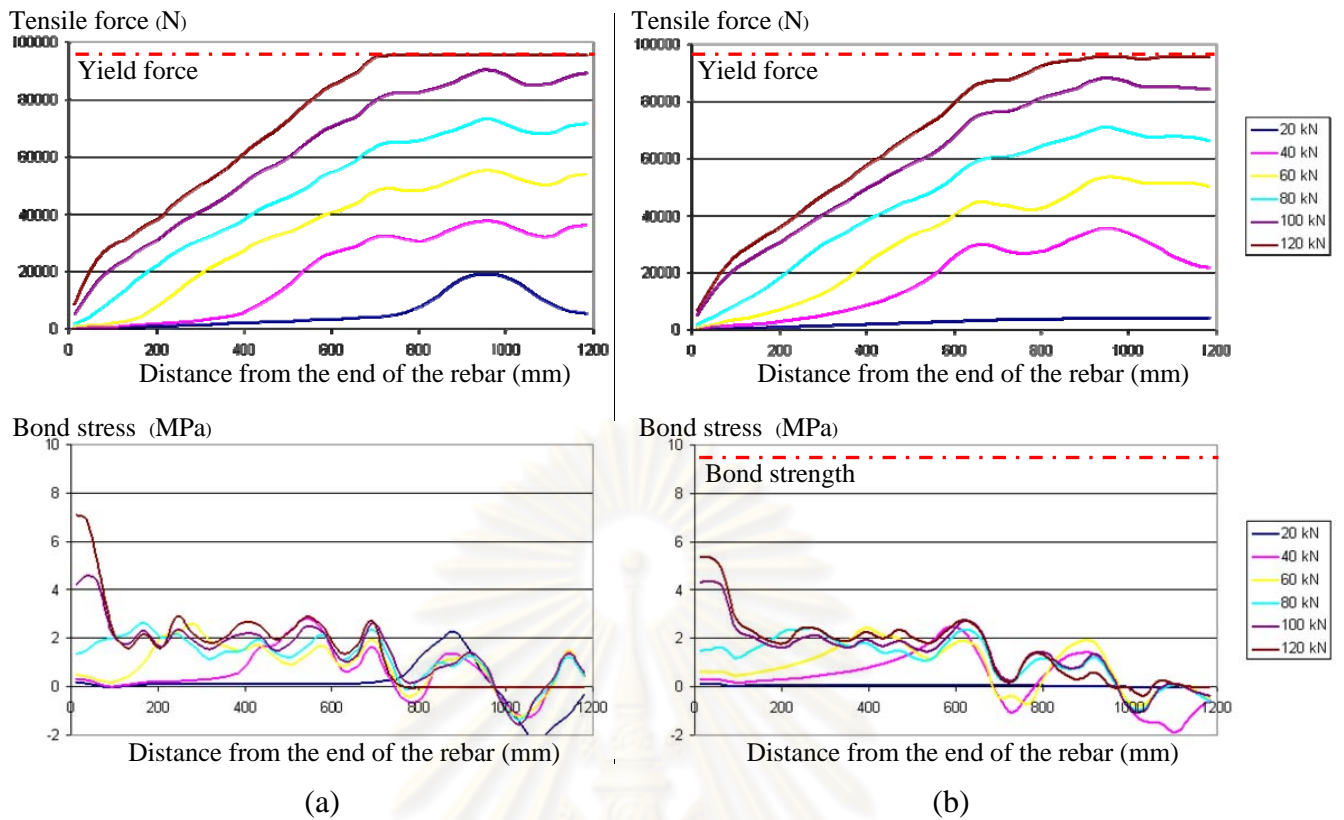


Figure 4.31 Variation of the tensile force and the bond stress distribution along the rebar with load for C40-RT: (a) FE model with perfect bond and (b) FE model with slip bond

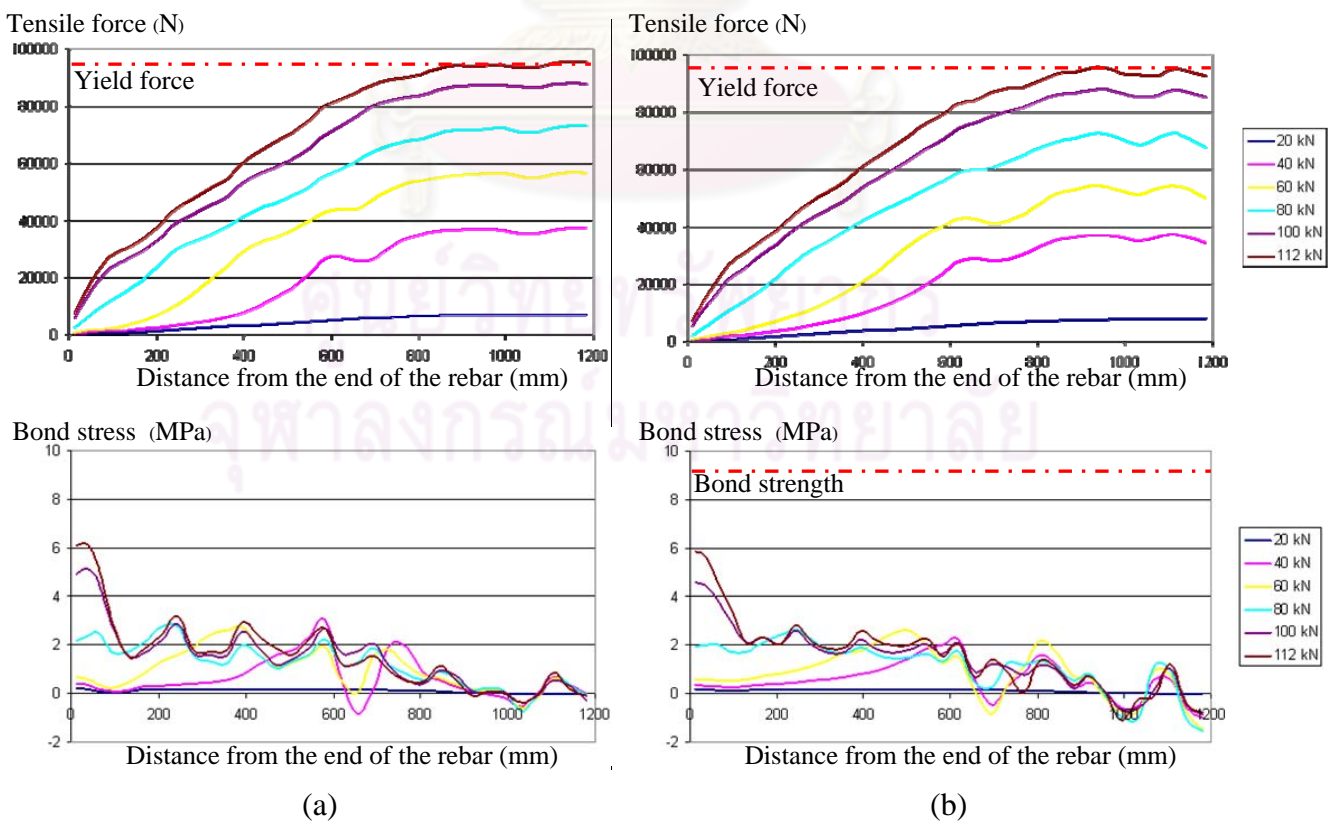


Figure 4.32 Variation of the tensile force and the bond stress distribution along the rebar with load for C40-250: (a) FE model with perfect bond and (b) FE model with slip bond

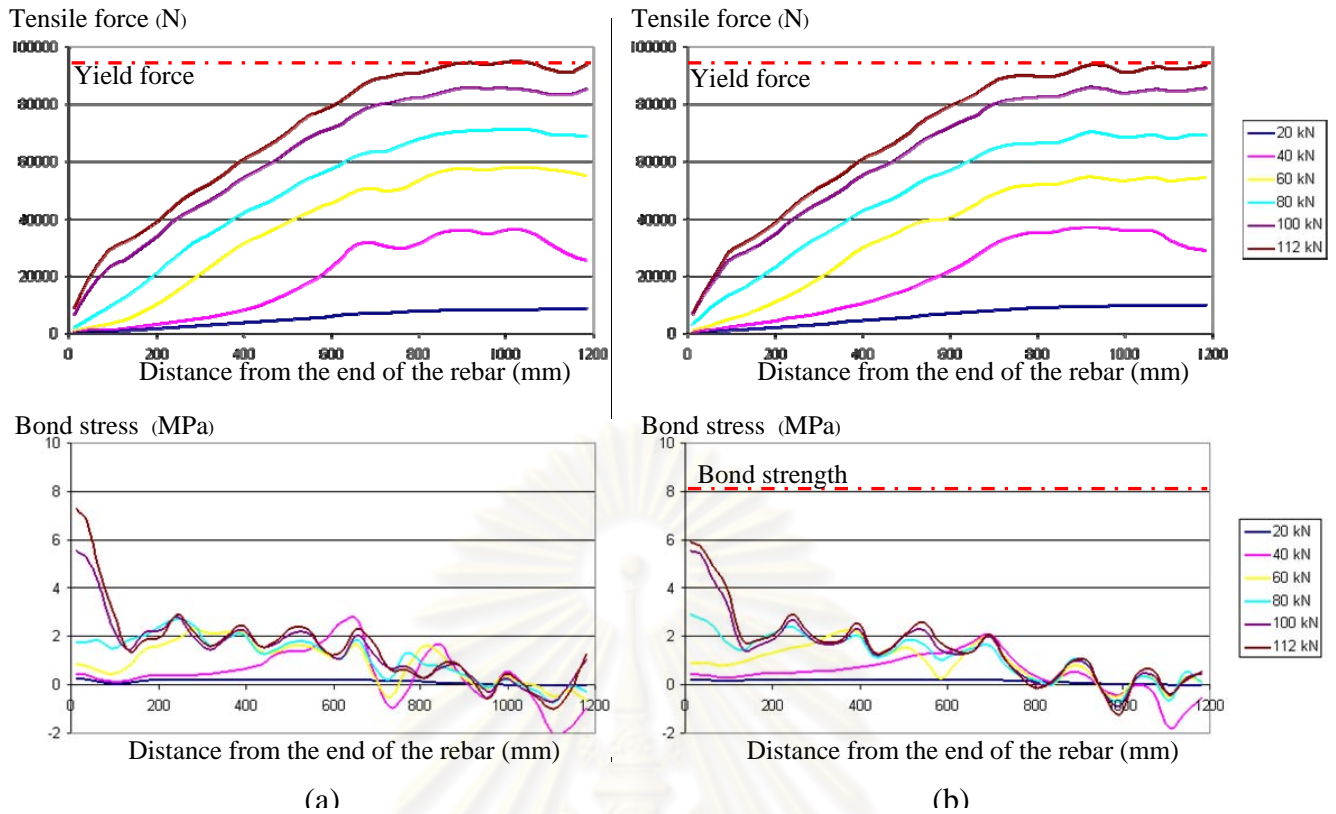


Figure 4.33 Variation of the tensile force and the bond stress distribution along the rebar with load for C40-400: (a) FE model with perfect bond and (b) FE model with slip bond

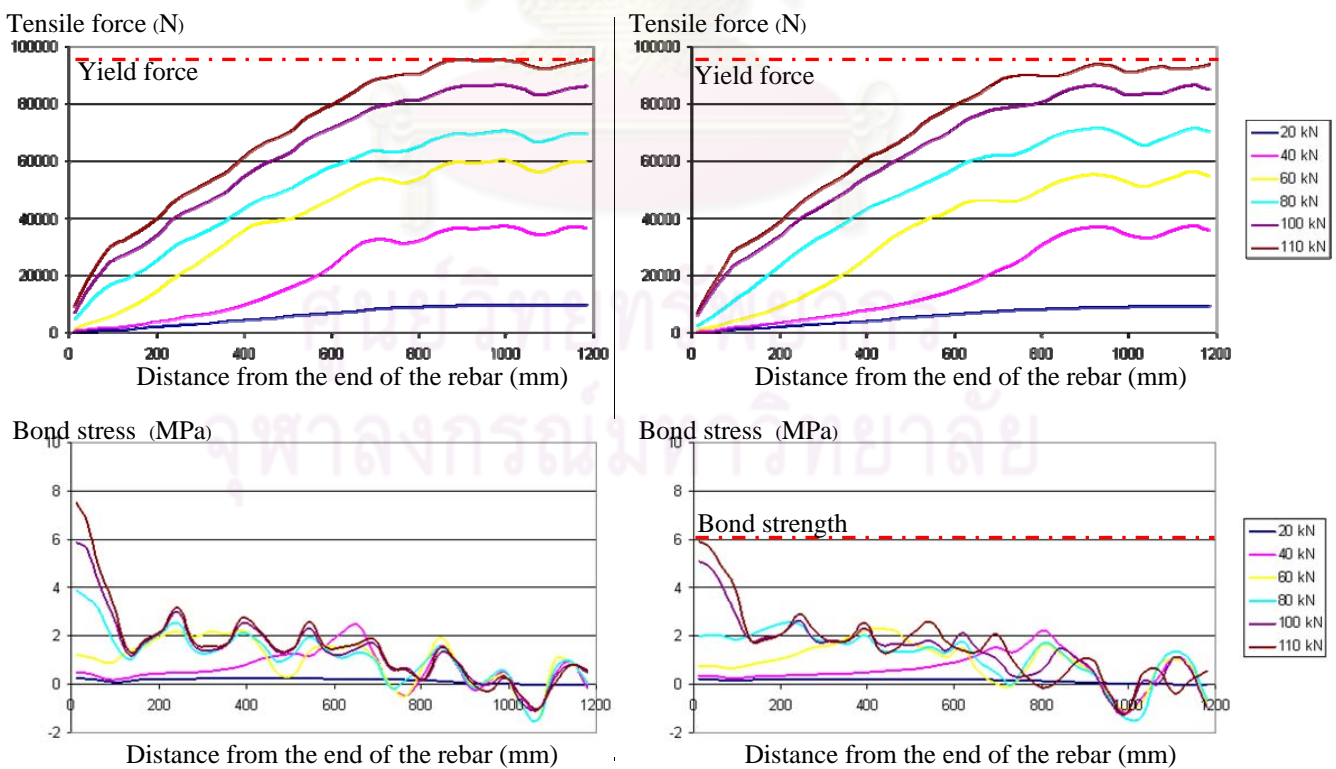


Figure 4.34 Variation of the tensile force and the bond stress distribution along the rebar with load for C40-550: (a) FE model with perfect bond and (b) FE model with slip bond

CHAPTER V

CONCLUSIONS

A mechanical bond model capable of characterizing the bonding behavior of reinforced concrete structures at elevated temperatures is proposed in the current study. The proposed model is developed based on the smear crack theory and the thick-wall cylinder theory by considering the concrete cover in its partially cracked elastic stage. The relationship between the splitting resistance and the inner crack radius of the concrete cover at the elevated temperature is established by taking into account the variation of the material properties with temperature and the differential thermal expansion of the steel rebar and the concrete cover. The computation procedure involves strain compatibility and pressure equilibrium at the rebar-concrete interface in order to estimate the thermal radial pressure and the corresponding crack radius. Furthermore, to investigate the bonding mechanism for the reinforced concrete elements at elevated temperatures, the effects of the pull-out force and the thermal load are simultaneously considered. The thermal crack is found to degrade the pressure resistance of the concrete cover to the pull-out force as the residual uncracked concrete cover is reduced. The proposed model is verified by using previous experimental results on the splitting bond strength of reinforced concrete elements at normal temperature as well as the critical temperature increment, the inner crack radius and the bond strength of reinforced concrete elements at elevated temperatures.

The mechanical bond-slip relationship is also examined by comparing the normalized bond stress-inner crack radius relationship obtained from the proposed model with the normalized bond-slip relationship of the previous experiments in which a linear relationship between the slip and the inner crack radius is found. The influence of the bond-slip relationship on the behavior of reinforced concrete structures is investigated through a series of load-bearing tests of reinforced concrete beams with 25-mm and 40-mm concrete covers at elevated temperatures. The types of

failure observed for the beam specimens are flexural failure, shear failure and shear failure with tensile splitting cracks. The tensile splitting cracks of the specimens with 25-mm concrete cover are viewed to be due to insufficient concrete cover and contribute to the structural failure.

The load-deflection relationships and the crack patterns of the tested beams are compared with the finite-element modeling results based on two types of bonding: perfect bonding and slip bonding (the proposed model). The comparisons reveal that the FE models with perfect bond and slip bond provide similar results in terms of the load-deflection curve, the crack pattern and the tensile force distribution along the rebars. For the bond stress distribution, the FE models with slip bond are capable of predicting the tensile splitting cracks in the beam specimens whereas the FE models with perfect bond tend to overestimate the bond stresses.

The current study has confirmed that the tensile splitting cracks can contribute to the failure of reinforced concrete structures at elevated temperatures. To prevent this type of failure, the structures must be designed with sufficient concrete cover. The model proposed in the current study is capable of predicting the bonding degradation and the tensile splitting cracks as well as their influences upon the behavior of reinforced concrete beams at elevated temperatures. The model can thus be adopted to determine the minimum concrete cover in the structural design for fire safety.

The model proposed in the current study is limited only for the splitting failure of the concrete structures reinforced with deformed steel bars without taking into account the effect of the transverse steel reinforcement (i.e., stirrups), which may enhance the bond strength of the reinforced concrete elements. Moreover, the current study adopts the mechanical properties of steel and concrete at elevated temperatures from the Eurocodes whereas the actual properties of the materials can vary in a wide range which could possibly affect the efficacy of the proposed model.

The tensile splitting cracks that have been found to contribute to the failure of reinforced concrete structures at elevated temperatures in the current study are based on a series of load-bearing tests of simply supported reinforced concrete beams at the elevated temperatures of up to 550°C. A more comprehensive test program should further be conducted to investigate the influences of the relevant parameters on the bond strength and the bond-slip relationship of reinforced concrete elements at elevated temperatures.



ศูนย์วิทยทรัพยากร
จุฬาลงกรณ์มหาวิทยาลัย

REFERENCES

- Abbasi, A. and Hogg, P.J. (2006). Fire testing of concrete beams with fibre reinforced plastic rebar. Composites: Part A 37:1142–1150.
- ACI Committee 408. (2003). Bond and development of straight reinforcing bars in tension, ACI 408R-03, American Concrete Institute, Farmington Hills, Mich.
- Alsawat, J., and Saatcioglu, M. (1992). Reinforcement Anchorage Slip under Monotonic Loading. ASCE, Journal of Structural Engineering, 118(9):2421-2438.
- Al-Negheimish, A.I., and Al-Zaid, R.Z. (2004). Effect of manufacturing process and rusting on the bond behavior of deformed bars in concrete. Cement & Concrete Composites, 26: 735–742.
- Aiello, M. A. (1999). Concrete Cover Failure in FRP Reinforced Beams under Thermal Loads, Journal of Composites for Construction, 3(1), 46-52.
- Aiello, M. A., Focacci, F., and Nanni, A. (2001). Effects of thermal loads on concrete cover of fiber reinforced polymer reinforced elements: Theoretical and experimental analysis. ACI Materials Journal, 98,4: 332–339.
- Amatavirakul, T. (2008). Flexural behavior of reinforced concrete beam under corrosion using finite element method. M.S. Thesis, Kasetsart University.
- Arioz, O. (2007). Effects of elevated temperatures on properties of concrete. Fire Safety Journal, 42: 516–522.
- Bazant, P., and Chern, J.C. (1987). Stress-induced thermal and shrinkage strains in concrete. ASCE, Journal of Engineering Mechanics, 113(10):1493–511.
- Bazant, Z. P., and Oh, B. H. (1983). Crack-band theory for fracture of concrete. Materials and Structures, 16: 155–177.
- Bazant, Z.P., and Kaplan, M.F. (1996). Concrete at high temperature: material properties and mathematical models. England: Longman Group Limited.
- Bazant, Z.P. (2002). Concrete fracture models: testing and practice. Engineering Fracture Mechanics, 29(2):165–205.
- Bratina, S., Saje, M., and Planinc, I. (2007). The effects of different strain contributions on the response of RC beams in fire. Engineering Structures, 29:418–30.
- Buchanan, A.H. (1999). Structural Design for Fire Safety. New Zealand: University of Canterbury.

- Cairns, J., and Jones, K. (1996). An evaluation of the bond-splitting action of ribbed-bars, ACI Materials Journal, 93,1: 10– 19.
- Capua, DD., and Mari, AR. (2007) Non-linear analysis of reinforced concrete cross-sections exposed to fire. Fire Safety Journal, 42:139–49.
- CEB-90 (1991). Final draft CEB-FIP model code 1990. Bulletin information 203, Committee Euro-International du Beton.
- Chang, Y.F., Chen, Y.H., Sheu, M.S., and Yao, G.C. (2006). Residual stress–strain relationship for concrete after exposure to high temperatures. Cement and Concrete Research, 36: 1999–2005.
- Chiang, CH., and Tsai, CL. (2003). Time–temperature analysis of bond strength of a rebar after fire exposure. Cement and Concrete Research, 33:1651-1654.
- Den Uijl, JA., and Bigaj, AJ. (1996). A bond model for ribbed bars based on concrete confinement. HERON, 41(3): 206-226.
- Diederichs, U., and Schneider, U. (1981). Bond strength at high temperatures. Magazine Concrete Research, 33(115):75 –84.
- Dotreppe, JC., and Franssen, JM. (1985). The use of numerical models for the fire analysis of reinforced concrete and composite structures. Engineering analysis, vol. 2. CML Publications, 2: 67-74.
- EC2. (2004). Eurocode 2: design of concrete structures—part 1–1: general rules and rules for building. London (UK): British Standards Institution. BS EN 1992-1-1.
- EC2. (2004). Eurocode 2: design of concrete structures—part 1.2: general rules- structural fire design. London (UK): British Standards Institution. BS EN 1992-1-2.
- EC3. (2005). Eurocode 3: design of steel structures—part 1–1: general rules and rules for buildings. London (UK): British Standards Institution. BS EN 1993-1-1.
- EC3. (2005). Eurocode 3: design of steel structures—part 1–2: general rules- structural fire design. London (UK): British Standards Institution. BS EN 1993-1-2.
- El-Hawary, M.M., and Hamoush, S.A. (1996). Bond Shear Modulus of Reinforced Concrete at High Temperatures. Engineering Fracture Mechanics, 55,6: 991-999.
- Eligeliausen, R., Popov, E., and Bertero, V. (1983). Local Bond Stress-Slip Relationship of Deformed Bars under Generalized Excitations. Report No.UCBEERC-83/23. Earthquake Engineering Center, University of California, Berkeley.
- Ellingwood, B., and Lin, TD. (1991) Flexure and shear behaviour of concrete beams during fires. ASCE, Journal of Structural Engineering, 117(2):440–58.

- Gambarova, P.G., and Rosati, G.P. (1997). Bond and splitting in bar pull-out: behavioural laws and concrete cover role. Magazine Concrete Research, 49 (179): 99–110.
- Goto, Y. (1971). Cracks formed in concrete around tension bars. ACI Journal, Proceedings, 68(4). April
- Guinea, G.V., Planas, J., and Elices, M. (1994). A general bilinear fit for the softening curve of concrete. Materials and Structures, 27(2):99–105.
- Haddad, R.H., and Shannis, L. (2004). Post-fire behavior of bond between high strength pozzolanic concrete and reinforcing steel. Construction and Building Materials, 18: 425–435.
- Haddad, R.H., Al-Saleh, R.J., and Al-Akhras, N.M. (2008). Effect of elevated temperature on bond between steel reinforcement and fiber reinforced concrete. Fire Safety Journal, 43: 334–343.
- Harajli, M.H., Hout, M., and Jalkh, W. (1995). Local bond stress-slip relationship of reinforcing bars embedded in plain and fiber concrete. ACI Materials Journal, 92(4): 343 - 354.
- Hertz, K.D. (1982). The anchorage capacity of reinforcing bars at normal and high temperatures. Magazine Concrete Research, 35(121):213 –20.
- Hertz, K.D. (2005). Concrete strength for fire safety design. Magazine Concrete Research, 57(8): 445–53.
- Huang, Z., and Platten, A. (1997). Non-linear finite element analysis of planar reinforced concrete members subjected to fire. ACI Structural Journal, 94(3):272–82.
- Huang, Z., Burgess I.W., and Plank R.J. (2009) Three-dimensional analysis of reinforced concrete beam-column structures in fire. Journal of Structural Engineering, 1201-1212
- Ibrahim, M. A., and Mahmood, S. M. (2009). Finite element modeling of reinforced concrete beams strengthened with FRP laminates. European Journal of Scientific Research, 30(4): 526-541.
- Khoury, G.A. (1992). Compressive strength of concrete at high temperatures: A reassessment. Magazine Concrete Research, 44 (161): 291–309.
- Kodur, V.K.R., and McGrath, R. (2003). Fire endurance of high strength concrete columns. Fire Technology, 89: 73–87.

- Kodur, V.K.R., and Dwaikat, M. (2008). A numerical model for predicting the fire resistance of reinforced concrete beams. Cement & Concrete Composites, 30: 431-443.
- Lee, HS., Takafumi, N., and Fuminori, T. (2002). Evaluation of the bond properties between concrete and reinforcement as a function of the degree of reinforcement corrosion. Cement and Concrete Research, 32: 1313–1318.
- Lettow, S. (2004). The Simulation of bond between concrete and reinforcement in nonlinear three-dimensional finite element analysis. IWB, University of Stuttgart, Stuttgart, Germany.
- Lie T.T., and Irwin R.J. (1993). Method to calculate the fire resistance of reinforced concrete columns with rectangular cross section. ACI Structural Journal, 90(1):52–60.
- Lin, T.D., Gustaferoo, A.H., and Abrams, M.S. (1981). Fire endurance of continuous reinforced concrete beams. PCA R&D Bulletin, RD072.01B.
- Masmoudi, R., Zaidi, A., and Ge´rard, P. (2005). Transverse thermal expansion of FRP bars embedded in Concrete. Journal of Composites for Construction, 9(5), 377-387.
- Mitchell, D. et.al., (1992). State-of-the-Art Report on Bond Under Cyclic Loads. Reported by ACI Committee 408, ACI 408.2R-92: 1-31.
- Morely, P., and Royles, R. (1983). Response of the bond in reinforcing concrete to high temperatures. Magazine Concrete Research, 35 (123): 67–74.
- Nielsen, C.V., and Bicanic, N. (2002). Radial fictitious cracking of thick-walled cylinder due to bar pull-out. Magazine Concrete Research, 54,3: 215– 221.
- Pantazopoulou, S.J., and Papoulia, K.D. (2001). Modeling cover-cracking due to reinforcement corrosion in RC structures. Journal of Mechanical Engineering, 127 (4): 342–351.
- Petersson, PE. (1981). Crack growth and development of fracture zone in plain concrete and similar materials. Report No. TVBM-1006, Division of building materials, Lund Institute of Technology, Lund, Sweden.
- Piloto, P.A.G. Ramos Gavilán, A.B., and Mesquita, L.M.R. (2006). Advanced Numerical method for estimate fire resistance of partially encased beams. International Congress in Fire Safety in Tall Buildings. Santander
- Pochanart S., and Harmon T. (1989) Bond-Slip Model for Generalized Excitations Including Fatigue. ACI Materials Journal, 86(5): 465-474

- Poon, C.S., Azhar S., Anson M., and Wong Y.L.. (2001). Strength and durability recovery of fire-damaged concrete after post-fire-curing. Cement and Concrete Research, 31: 1307–1318.
- Reichel, V. (1978). How fire affects steel-to-concrete bond? Building Research and Practice, 6(3):176 -87.
- Roelfstra, P.E., and Wittmann, F.H. (1986). Numerical method to link strain softening with failure of concrete. Fracture Toughness and Fracture Energy of Concrete. Ed. Wittmann, F.H. Elsevier, 163-175.
- Rohugo, K., Iwasa, M., Suzuki, K., and Koyanagi, W. (1989) Testing methods to determine tensile strain-softening curve and fracture energy of concrete. Ed. Mihashi, H., Takahashi, H., Wittmann, FH., Balkema, : 153-63
- Royles, R., and Morley, P. (1983). Response of the bond in reinforced concrete to high temperatures. Magazine Concrete Research, 35(123):67 –74.
- Saroushian, P., and Choi, K-B. (1989). Local Bond of Deformed Bars with Different Diameters in Confined Concrete. ACI Structural Journal, 86,2: 217-22.
- Sarshar, R., and Khoury, G.A. (1993). Material and environmental factors influencing the compressive strength of unsealed cement paste and concrete at high temperatures. Magazine Concrete Research, 45 (162): 51–61.
- Sebastjan Bratina, Bojan C., Miran Saje, and Igor Planinc. (2005). Numerical modelling of behaviour of reinforced concrete columns in fire and comparison with Eurocode 2. International Journal of Solids and Structures, 42: 5715–5733.
- Skorobogatov, SM., and Edwards, AD. (1979) The influence of the geometry of deformed steel bars on their bond strength in concrete. Proceedings - Institution of Civil Engineers, 67 (Pt. 2).
- Taerwe, L., et al. (2008). Fib Bulletin 46: Fire Design of Concrete Structures - Structural Behaviour and Assessment, State-of the art Report. International Federation for Structural Concrete (fib TG 4.3.2), Lausanne.
- Takahiro, S, Toshiyuki, K., Keisuke, Y., and Hiroshi, F. (1999). Bond Splitting Behavior of Continuous Fiber Reinforced Concrete Members. ACI SP-188: 1131-1144.
- Tepfers, R. (1979). Cracking of concrete cover along anchored deformed reinforcing bars. Magazine Concrete Research, 31(106): 3-12.
- Tepfers, R. (1982). Lapped Tensile Reinforcement Splices. ASCE, Journal of Structural Division, 108, ST1: 283-301.

- Terro, MJ. (1998). Numerical modeling of the behavior of concrete structures in fire. ACI Structural Journal, 95(2):183–93.
- Timoshenko, S. P., and Goodier, J. N. (1970). Theory of Elasticity, 3rd ed. (International Student Edition). Tokyo : McGraw-Hill Kogakusha Ltd., Japan.
- Valcuende, M., and Parra, C. (2009). Bond behaviour of reinforcement in self-compacting concretes. Construction and Building Materials, 23: 162-170.
- Walraven J.C., Han N., and Stroband J. (1993). Experimenteel onderzoek aan beton met hoge sterkte. run-Commissie Rapport 93-7 Part II (in Dutch), 38-75.
- Wang, X., and Liu X. (2003). A strain-softening model for steel–concrete bond. Cement and Concrete Research, 33:1669–1673.
- Wittmann, FH., Rokugo, K., Bruhwiler, E., Mihashi, H., and Simopnin, P. (1988). Fracture energy and strain softening of concrete as determined by compact tension specimens. Materials and Structures, 21(1):21–32.
- Wong Y.L., Fu Y.F., Poon C.S., and Tang C.A. (2006). Spalling of concrete cover of fiber-reinforced polymer reinforced concrete under thermal loads. Materials and Structures, 39:991-999
- Xiao, J., and Konig, G. (2004). Study on concrete at high temperature in China—an overview. Fire Safety Journal, 39: 89–103.
- Xiao, J., and Falkner H. (2007). Bond behaviour between recycled aggregate concrete and steel rebars. Construction and Building Materials, 21: 395-401.
- Xie, GM., and Qian, ZZ. (1998). Research on bond and tension behaviour of concrete after high temperature. Journal of Zhejiang University, 32(5):597–602.
- Yasojima, A., and Kanakubo, T. (2005). Bond splitting Strength of RC Members Based on Local Bond Stress and Slip Behavior. 11th International Conference on Fracture, 4486.
- Youssef, M.A., and Moftah, M. (2007). General stress–strain relationship for concrete at elevated temperatures. Engineering Structures, 29: 2618–2634.
- Zaidi, A., and Masmoudi, R. (2008). Thermal effect on fiber reinforced polymer reinforced concrete slabs. Canadian Journal of Civil Engineering, 35, 312–320.
- Zha, X.X. (2003) Three-dimensional non-linear analysis of reinforced concrete members in fire. Building and Environment, 38: 297 – 307
- Zhang, B., and Bicanic, N. (2002). Residual fracture toughness of normal- and high-strength gravel concrete after heating to 600°C. ACI Materials Journal, 99 (3): 217-226.

- Zhou, S., Rizos, D.C., and Petrou, M.F. (2004). Effects of superstructure flexibility on strength of reinforced concrete bridge decks. Computers and Structures, 82: 13–23
- Zhou, XG., and Wu, JL. (1995). Tests and analysis on bond performance between bars and concrete after high temperature. Chinese Industrial Construction, 25(5):37–40.



ศูนย์วิทยทรัพยากร
จุฬาลงกรณ์มหาวิทยาลัย



APPENDIX

ศูนย์วิทยทรัพยากร
จุฬาลงกรณ์มหาวิทยาลัย

FE Mesh Refinement for Structural and Thermal Analyses

To determine the appropriate FE mesh to be used for structural analysis, we examine a series of FE models with different meshing schemes; M1, M2, M3, M4 and M5, for the beam specimens in C25 and C40 series as illustrated in Figure A-1. The load-deflection curves obtained from the FE analysis of the beam models are plotted in Figure A-2. It can be seen from the illustration that the accuracy of the load-deflection relationships obtained from the beam models in case M4 for both C25 and C40 series are acceptable compared to case M5.

The capability of the FE models in case M4 (a) and case M4 (b) for thermal analysis have also been verified by examining the temperature distribution within the cross section of the beam models. Because the locations of the points where temperatures were measured within the beam specimens do not match with the nodal points of the beam models in case M4, we have to indirectly compare the temperature distribution obtained from the FE models in case M4 with the models having a more refined meshing scheme comprising 5-mm elements, of which the temperature-time curves agree well with the experimental results as can be seen in Figures A-3 and A-4. The vertical and the horizontal lines across the beam models (A-A and B-B) as illustrated in Figure A-5 have been specified to examine the difference between the temperature distribution obtained from the FE model in case M4 and that with 5-mm elements. Figure A-6 compares the temperature distribution obtained from the FE model in case M4 and the FE model with 5-mm elements for C25-550 and C40-550. It is seen from the figure that the FE model in case M4 is able to provide reasonably accurate results.

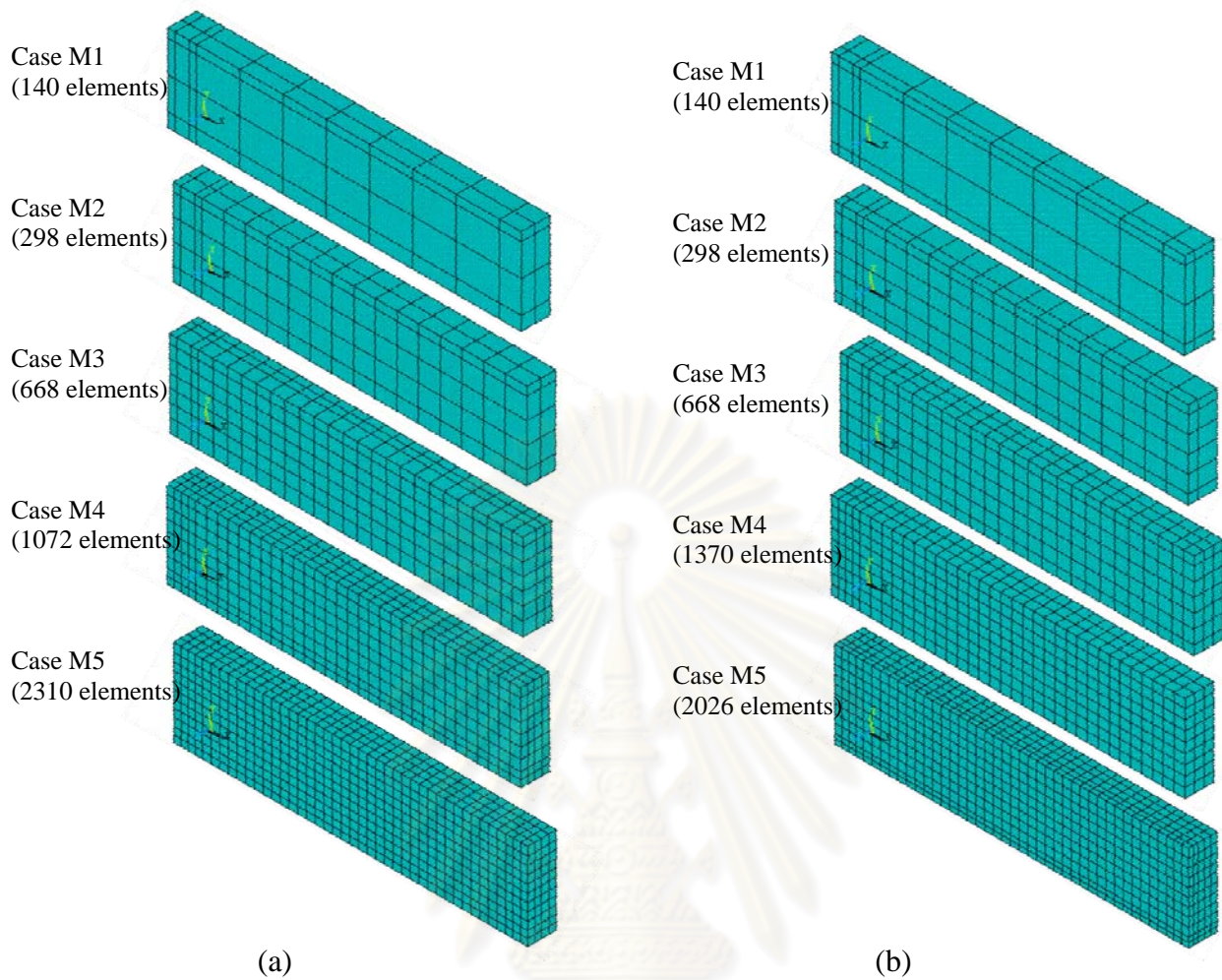


Figure A-1 FE models with different meshing schemes: (a) C25 series and (b) C40 series

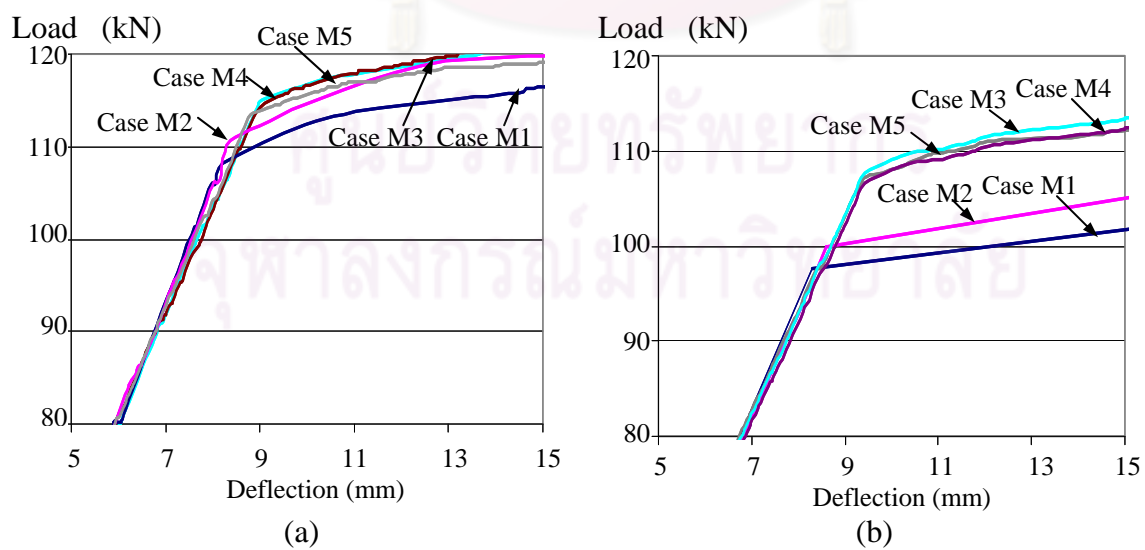


Figure A-2 Load-deflection relationships obtained from the FE models with different meshing schemes: (a) C25 series and (b) C40 series

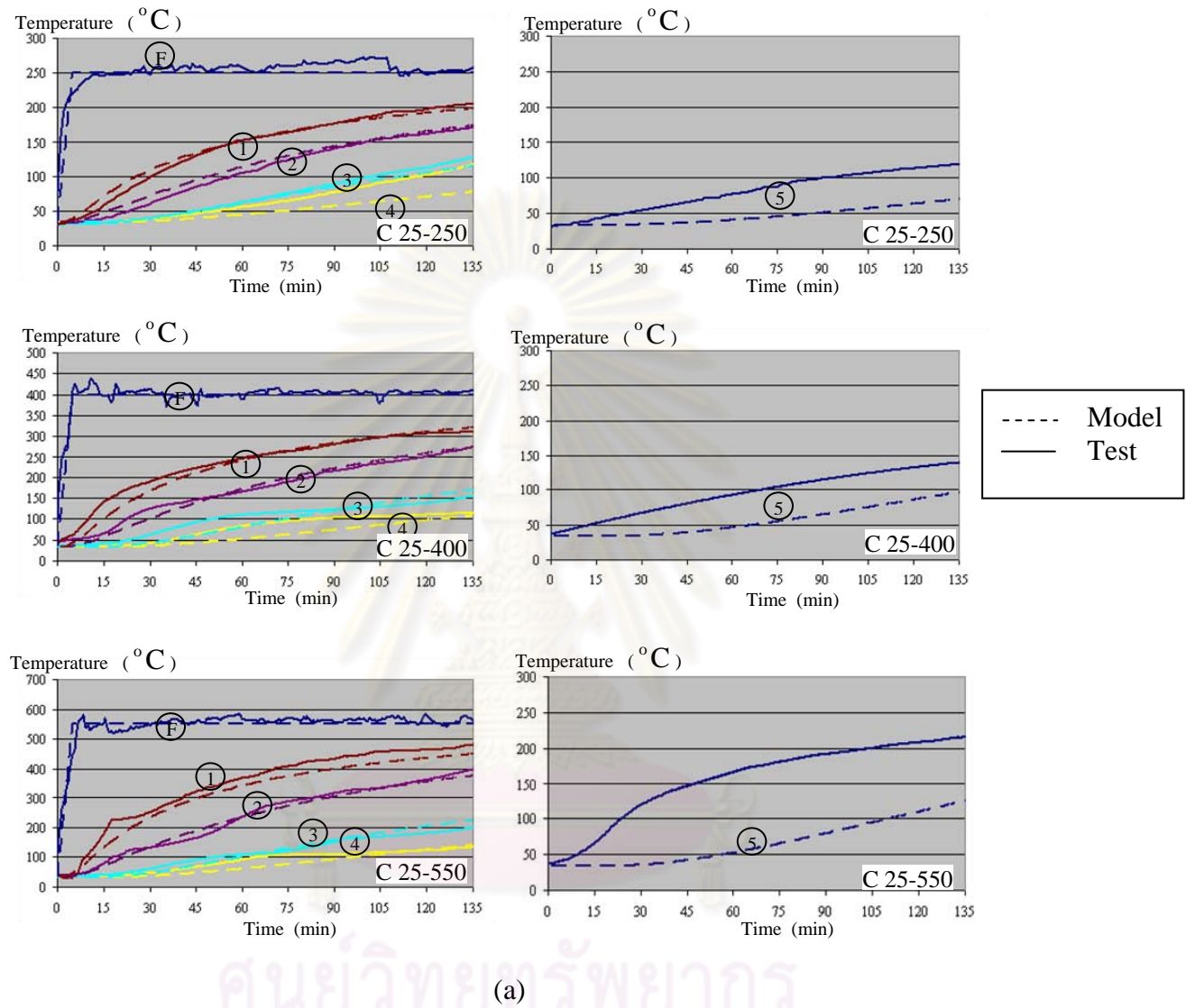


Figure A-3 Comparison of the temperature-time curves obtained from the experiment and the FE model with 5-mm elements for C25 specimens

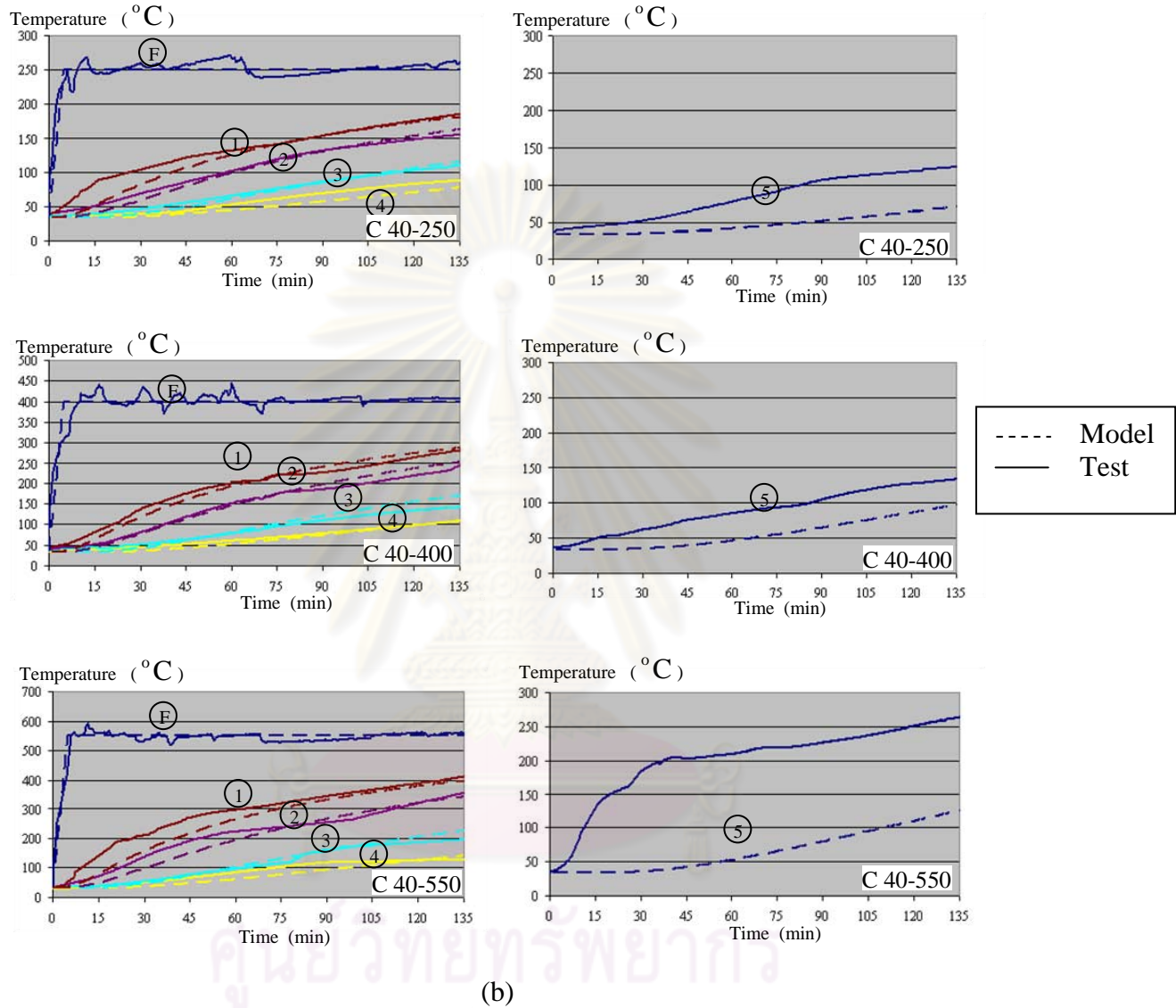


Figure A-4 Comparison of the temperature-time curves obtained from the experiment and the FE model with 5-mm elements for C40 specimens

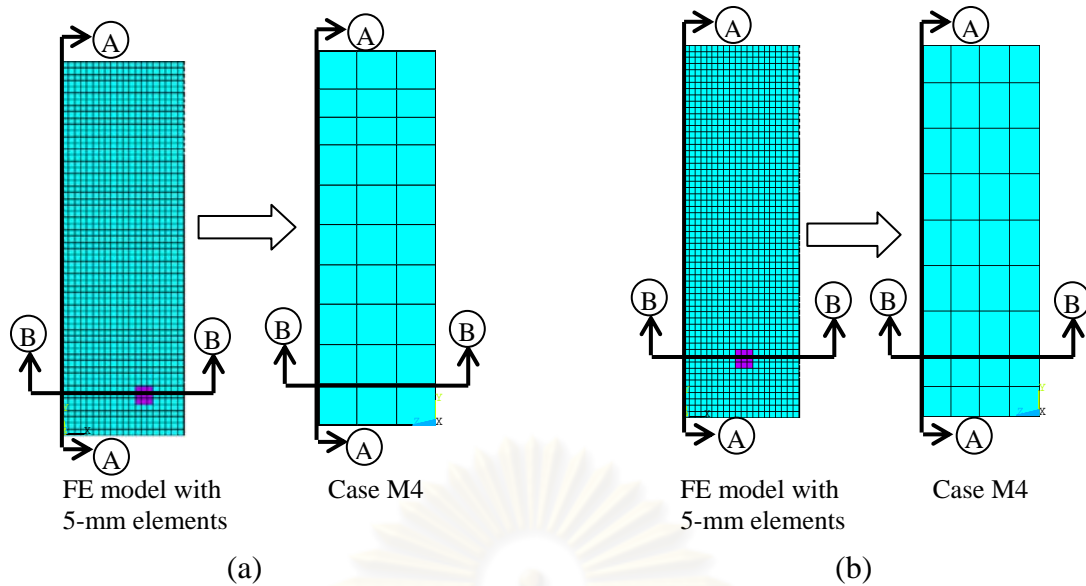


Figure A-5 Lines A-A and B-B for the comparison of temperature distribution: (a) C25 series and (b) C40 series

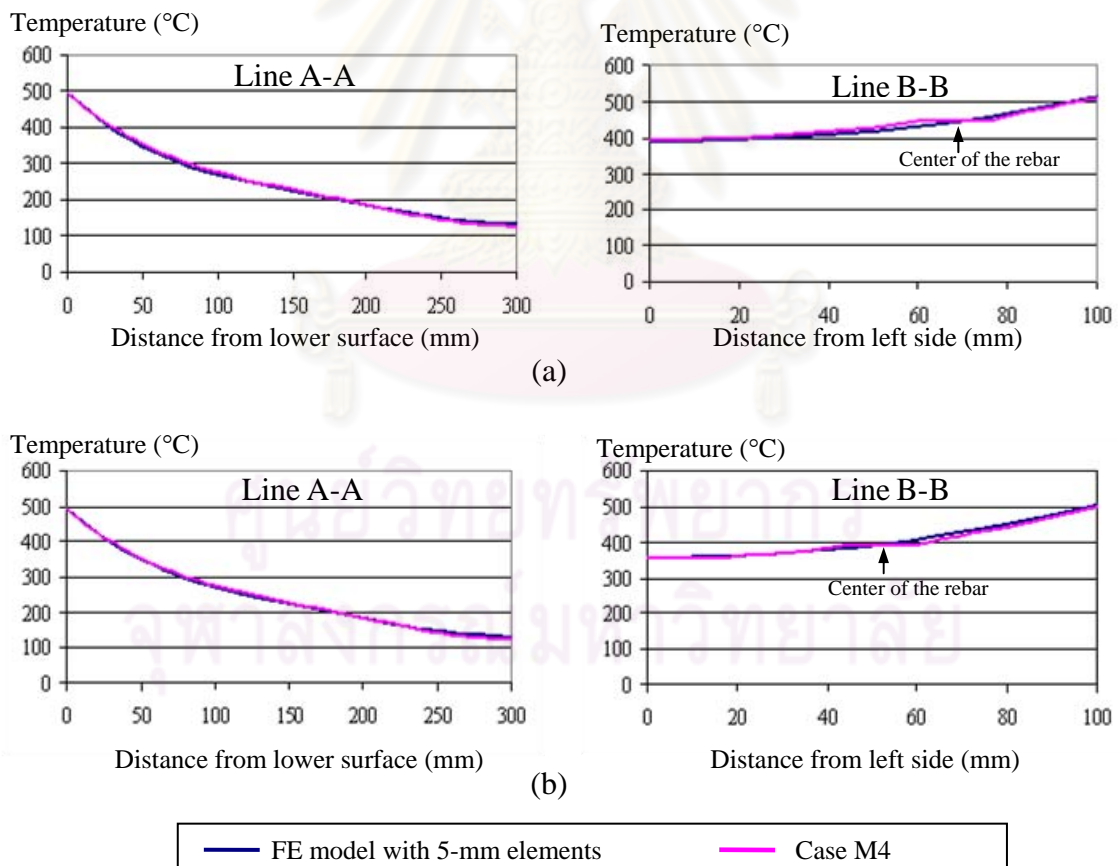


Figure A-6 Comparison of the temperature distribution obtained from the FE model in case M4 and the FE model with 5-mm elements: (a) C25-550 and (b) C40-550

VITA

Mr. Pattamad Panedpojaman was born in Songkhla, Thailand in 1980. He graduated Bachelor's degree in Civil Engineering at King Mongkut's Institute of Technology Ladkrabang in 2002 and Master's degree in Civil Engineering at Chulalongkorn University in 2005. He has been granted the scholarship by AUN/SEED-Net to study PhD degree in the field of Structural Engineering, Department of Civil Engineering, Chulalongkorn University, Thailand since 2008.



ศูนย์วิทยทรัพยากร
จุฬาลงกรณ์มหาวิทยาลัย